

MECHANICS AND DYNAMICS OF BALLEN MILLING

By

Peter Pak Wing Lee

B. A. Sc. (Mechanical Engineering)

University of British Columbia, 1993

**A THESIS SUBMITTED IN PARTIAL FULFILLMENT OF
THE REQUIREMENTS FOR THE DEGREE OF
MASTER OF APPLIED SCIENCE**

in

**THE FACULTY OF GRADUATE STUDIES
MECHANICAL ENGINEERING**

We accept this thesis as conforming
to the required standard

THE UNIVERSITY OF BRITISH COLUMBIA

August 1995

© Peter Pak Wing Lee, 1995

In presenting this thesis in partial fulfilment of the requirements for an advanced degree at the University of British Columbia, I agree that the Library shall make it freely available for reference and study. I further agree that permission for extensive copying of this thesis for scholarly purposes may be granted by the head of my department or by his or her representatives. It is understood that copying or publication of this thesis for financial gain shall not be allowed without my written permission.

Department of MECHANICAL ENGINEERING

The University of British Columbia
Vancouver, Canada

Date OCTOBER 16, 1995

Abstract

Ball end milling has been used extensively in current manufacturing industry in producing parts with sculptured surfaces. Due to its complex cutter geometry, ball end milling mechanics and dynamics have not been studied until recently. In this research, the mechanics and dynamics of cutting with a special helical ball end cutter are modeled. A unified mathematical model, which considers the true rigid body kinematics of milling, static deformations and forced and self excited vibrations, is presented. The ball end mill attached to the spindle is modeled by two orthogonal structural modes in the feed and normal directions at the tool tip. For a given cutter geometry, the process dependent cutting coefficients are obtained by applying oblique tool geometry to the fundamental properties such as shear yield stress, shear angle and average friction angle measured from orthogonal cutting tests. The three dimensional surface finish generated by the helical flutes is digitized using the true kinematics of ball end milling process. The dynamically regenerated chip thickness, which consists of rigid body motion of the cutter and structural vibrations, is evaluated at discrete time intervals by comparing the present and previous tooth marks left on the finish surface. The process is simulated in time domain, by considering the instantaneous regenerative chip load, local cutting force coefficients, structural transfer functions and the geometry of ball end milling process. The proposed model predicts cutting forces, finished surface and chatter-free condition charts, and is verified experimentally under both static and dynamic cutting conditions. The model allows process planners to select cutting conditions to minimize dimensional surface errors, shank failure and chatter vibrations for end milling operations.

Table of Contents

Abstract	ii
Table of Contents	iii
List of Tables	vi
List of Figures	vii
Acknowledgement	xi
1 Introduction	1
2 Literature Review	4
2.1 Overview	4
2.2 Milling Force Models	7
2.2.1 Mechanistic Model	9
2.2.2 Mechanics of Milling Model	12
2.3 Dynamic Cutting	13
3 Geometric Modelling of Milling Cutters	17
3.1 Introduction	17
3.1.1 Modelling of Cylindrical End Mill	18
3.1.2 Modelling of Ballend/Bullnose Mill	20
3.1.3 Modelling of Tapered Ballend Mill	24
3.1.4 Cutting Geometry and Chip Thickness Calculation	25

3.2	Conclusions	28
4	Modelling of Milling Forces	30
4.1	Introduction	30
4.2	Milling Force Models	32
4.2.1	Mechanistic approach with Average Force Model	32
4.2.2	Mechanics of Milling Model	36
4.2.3	Prediction of Cutting Force Coefficients from an Oblique Cutting Model	42
4.2.4	Simulation and Experimental Verification	53
4.3	Conclusions	58
5	Dynamic Milling and Chatter Stability	63
5.1	Introduction	63
5.2	Modelling of Dynamic Milling	68
5.2.1	Dynamic Milling Implementation	69
5.2.2	Structural Dynamic Model	74
5.3	Chatter Stability	77
5.3.1	Prediction of Chatter Stability from Time Domain Simulation . .	80
5.4	Simulations and Experimental Verification	86
5.4.1	Verifications with Cylindrical End Mill	87
5.4.2	Verifications with Ballend Mill	101
5.4.3	Summary	138
5.5	Conclusions	138
	Conclusions	140
	Bibliography	143

Appendices	147
-------------------	------------

A Ballend Milling Force Coefficients	147
---	------------

List of Tables

4.1	Orthogonal cutting data	51
4.2	Cutting conditions for static ballend tests and simulations	55
5.1	Time Domain Simulation Conditions for Dynamic Ball End Milling Tests I	119
5.2	Cutting Conditions for Dynamic Ball End Milling Tests II	120
A.1	Edge Force Coefficients, Rake = 0 degree	148
A.2	Cutting Force Coefficients, Rake = 0 degree	148
A.3	Results from Orthogonal Cutting Experiments	149

List of Figures

2.1	Common milling geometries: a) Up milling, b) Down milling	5
2.2	a) Orthogonal cutting geometry, b) Oblique cutting geometry	8
2.3	Force diagram in chip formation	10
2.4	Dynamic Cutting and Wave Regeneration in Orthogonal Cutting	14
3.1	a) Cylindrical End Mill, b) Ballend Mill, c) Bullnose Mill, d) Tapered Ballend Mill	19
3.2	a-d Geometric model of Ballend cutter	22
3.3	Geometric parameters along ballend cutter	23
3.4	Common milling geometry and chip formation	27
3.5	Chip Thickness Profile at two cutter locations, solid line - approximation, dotted line - exact kinematics	29
4.1	Average Forces vs Feed rate for different axial depth of cuts in ballend milling	37
4.2	Average Edge Forces vs axial depth of cut in ballend milling	38
4.3	Ballend Milling Force coefficients estimated from Average Force Model: a) vs s_t , b) vs a	39
4.4	Oblique Cutting Geometry of a Ballend Mill	41
4.5	Experimental Setup - Orthogonal Turning test	45
4.6	Edge Force Extrapolation from Orthogonal Turning test	47
4.7	Cutting Ratio identified from Orthogonal Turning test	48
4.8	Shear Stress identified from Orthogonal Turning test	49

4.9	Friction angle identified from Orthogonal Turning test	50
4.10	Generalized Mechanics of Cutting Approach to Milling Force Prediction .	52
4.11	Experimental Setup for Milling Test	54
4.12	Statistical Evaluation of Model and Data	57
4.13	Measured and predicted cutting forces for slot cutting tests, ballend mill, spindle speed $269rev/min$, $R_0 = 9.525mm$, $i_0 = 30^\circ$, $s_t = 0.0508[mm/flute]$ (a)- $a = 1.27 [mm]$ (b)- $a = 6.35[mm]$, rake=0	59
4.14	Measured and predicted cutting forces for slot cutting tests, ballend mill, spindle speed $269rev/min$, $i_0 = 30^\circ$. (a) $a=3.81 [mm]$, $R_0=9.525 mm$, $s_t=0.1016[mm/flute]$, rake=5 (b) $a=3.048 [mm]$, $R_0=6.35 mm$, $s_t=0.0762$ [mm/flute], rake=10	60
4.15	Measured and predicted cutting forces for half radial immersion cutting tests, ballend mill, $\alpha_n = 0^\circ$, $a=6.35mm$, spindle speed $269rev/min$, $i_0 =$ 30° , (a) $s_t=0.0508 [mm/flute]$, (b)- $s_t=0.102 [mm/flute]$	61
4.16	Measured and predicted cutting forces for slot milling with a 3 fluted bal- lend mill, $a = 8.9mm$, $i_0 = 30^\circ$, (a) spindle speed $480rev/min$, $\alpha_n = 15^\circ$, $s_t=0.0889 [mm/flute]$, (b) spindle speed $615rev/min$, $\alpha_n = 0^\circ$, $s_t=0.127$ [mm/flute]	62
5.1	Schematic Representation of a SDOF System	65
5.2	Frequency Domain characteristic curve for a SDOF Dynamic System . .	67
5.3	Evaluation of chip thickness from the dynamically generated surfaces at present and previous tooth periods	70
5.4	Dynamic model and Chip thickness regeneration mechanism in milling .	73
5.5	Analytical and time domain stability limit predictions for a case analyzed by Smith and Thusty	78

5.6	Phase difference between the current and previous surfaces resulting from tool vibration	79
5.7	Time Domain Stability Limit Calculation Algorithm	82
5.8	Experimental and Simulated Cutting Forces, cylindrical end milling . . .	88
5.9	Stability Lobe Diagram for Cylindrical End milling. Weck's Experiments	89
5.10	Cutting Force Simulation I, cylindrical cutter, Weck's experiments	91
5.11	Vibrations Simulation I, cylindrical cutter, Weck's experiments	92
5.12	Peak To Peak Graphs from Time Domain Simulation I, cylindrical cutter. Weck's Experiments	94
5.13	Cutting Forces and Vibrations Simulation II, Weck's Experiments	95
5.14	Fourier Spectrums from Simulations II, Weck's Experiments	96
5.15	Simulated Surface under Chatter Condition, from Simulations II	97
5.16	Simulated Surface Mark at $z = 2.0mm$ under Chatter Condition, from Simulations II	98
5.17	Analytical and Time Domain Predicted Stability Lobes, cylindrical cutter	100
5.18	Model Verification I - Chip Thickness Profile	102
5.19	Model Verification II - Cutting Force Patterns	103
5.20	Model Verification III - Surface Feed Marks: a) $\Psi = 0^\circ$ (up milling side), b) $\Psi = 90^\circ$ (down milling side)	105
5.21	Experimental Setup - Dynamic Test	107
5.22	Measured Transfer Function at Tool Tip, Ballend Milling Test I	108
5.23	Static Stiffness Measurements, Ballend Milling Test I	109
5.24	Measured Workpiece Transfer Function, Ballend Milling Test I	110
5.25	Dynamic Ballend Milling Test I, Speed = 115-430 RPM	111
5.26	Dynamic Ballend Milling Test I, Speed = 730-1450 RPM	112
5.27	Fourier Spectrum of F_x from Ballend Milling Test I	113

5.28 Measured and Simulated Cutting Forces, N=115 RPM, Ballend Milling	
Test I	115
5.29 Fourier Spectrum from Ballend Milling Test I, N=115 RPM	116
5.30 Measured and Simulated Cutting Forces, N=1000 RPM, Ballend Milling	
Test I	117
5.31 Fourier Spectrum from Ballend Milling Test I, N=1100 RPM	118
5.32 Transfer Function Measured at tool tip. Ballend Test II	121
5.33 Ballend Milling Experiments II, $a = 2\text{mm}$	122
5.34 Ballend Milling Experiments II, $a = 3\text{mm}$	123
5.35 Experimental and Simulated PTP results. Ballend Milling Test II	126
5.36 Simulated Stability Lobe Diagram for Ballend milling Test II	127
5.37 Simulated Cutting Forces and Vibrations. Ballend Milling Test II	128
5.38 Simulated Cutting Forces and Vibrations. Ballend Milling Test II	129
5.39 Wave generation on different cutting geometries. Ballend Milling	130
5.40 Simulated Stability Lobe Diagram for Ballend milling III	131
5.41 Simulations showing the waviness on cut surface at different cutting speeds	132
5.42 Simulations of cutting forces at 2 different speeds, Ballend milling	134
5.43 Simulations of vibrations at 2 different speeds, Ballend milling	135
5.44 FFT of the simulated cutting forces at different speeds, Ballend milling	136
5.45 Simulations of finished surfaces at different speeds, Ballend milling	137

Acknowledgement

I would like to express my sincere gratitude to my research supervisor Dr. Yusuf Altıntaş, who provided me with valuable instructions and supports throughout the course of my graduate work. I would also like to extend special thanks to Dr. Erhan Budak, as well as to all my colleagues in the Manufacturing research group at UBC, for their patience, assistances and more importantly, their precious friendships.

I am thankful to my girl friend, Phoebe, and my brothers and sisters in Thy family, for their continuous supports and encouragements during the toughest time of my research.

My deepest gratitude is extended to my family, who are always behind me and have confident in me. I dedicate this work to them.

*"The fear of the LORD is the beginning of wisdom.
and knowledge of the Holy One is understanding."*

Proverbs 9:10

Nomenclature

a	axial depth of cut
a_{lim}	limiting axial depth of cut for chatter stability
a_{xx}, a_{yy}	directional dynamic milling coefficients
b	radial depth of cut
db	differential cutting edge length in the direction perpendicular to the cutting velocity
dz	differential height in axial direction
$dF_{tj}, dF_{rj}, dF_{aj}$	differential cutting forces in tangential, radial, and axial directions for tooth j
h	uncut chip thickness normal to cutting edge in milling
i_0	helix angle at ball shaped flute and shank meeting point
$i(\psi)$	local helix angle on the flute
r_t	cutting chip ratio in orthogonal cutting
s_t	feed per tooth
t, t_c	uncut and cut chip thickness in orthogonal cutting

$[A(t)]$	directional dynamic milling coefficient matrix
F_c, F_f	cutting and feed force in orthogonal cutting
F_{xj}, F_{yj}, F_{zj}	milling forces in Cartesian coordinates on flute j
G_x, G_y	Transfer functions in x and y directions, lumped at tip of cutter
K_{tc}, K_{rc}, K_{ac}	tangential, radial, and axial cutting force coefficients in milling
K_{te}, K_{re}, K_{ae}	tangential, radial, and axial edge force coefficients in milling
K_z	number of axial elements
N_f	number of flutes
N	spindle speed in revolution per minute
R_0	ball radius
$R(\psi)$	tool radius in x-y plane at a point defined by ψ

α_r, α_n	radial and normal rake angles
ϵ	phase between successive waves in chatter vibrations
γ	flank clearance angle
κ	angle in a vertical plane between a point on the flute and the z axis
ϕ, β	shear and average friction angles in orthogonal cutting
ϕ_n, β_n	normal shear and normal friction angles in oblique cutting
η_c	chip flow angle on the rake face
ω_c	chatter frequency
ψ	lag angle between the tip ($z=0$) and a point on the helical flute at height z
ψ_0	maximum lag angle between the tip($z=0$) and uppermost cutting point ($z=a$)
ϕ_p	pitch angle of the cutter ($= 2\pi/N_f$)
τ	shear stress at the shear plane
θ	tool rotation angle, measured from +ve y-axis cw
Ψ	local immersion angle in global coordinates, measured from +y axis (CW)
Ω	spindle speed in radian per second

Chapter 1

Introduction

Milling remains one of the most common machining operations in manufacturing industry mainly due to its flexibility in producing a wide range of shapes such as stamping dies and pockets found in die and mold industry, high performance parts encountered in aerospace components, and compressor impellers. Current manufacturing technologies have focused on increasing the productivity and the quality of the finished parts while maintaining a sufficient process stability and reliability. The most common methods involve selecting conservative cutting conditions, determining the appropriate machining conditions by the trial and error methods, or employing multiple finishing cuts to achieve better accuracy, which result in lower productivity and higher cost. Satisfactory production levels can be achieved if the process layout considers all aspects of the machining operations, such as the pre-specified surface tolerance, machine tool vibrations, and tool breakage. Furthermore, these issues are becoming more critical due to the recent advances in high speed milling technology employed in die and mold making industry. The development of reliable milling process methods is therefore important for increasing metal removal rates while maintaining the process stability and the required accuracy.

This study aims at analyzing the physics of a machining process, in particular, the mechanics and dynamics of milling with ball end mills used mainly in producing sculptured surfaces in die and mold and aerospace industry. Two key problems associated with this process, the cutting force prediction and chatter stability analysis in ball end

milling, are studied in the following chapters. A comprehensive and improved milling force model, based on the exact kinematics model presented by Montgomery [1], is applied to the ball end milling for the simulation of the process. The model predicts the milling forces, dimensional surface finish, and chatter-free machining conditions using shear stress, shear angle and friction coefficient of the cutting process, oblique tool geometry along the helical ball ended flutes and structural dynamic parameters of the machine tool system.

Henceforth, the thesis is organized as follows:

Chapter 2 provides necessary background and literature review on milling analysis. The fundamentals of metal cutting analysis, orthogonal and oblique cutting mechanics, geometry of milling, past models for the prediction of cutting forces, vibrations and machine tool chatter, are briefly reviewed.

Chapter 3 presents the geometric models of several common milling cutters. The geometric models of cylindrical, bull nose, ball end mills and taper ball end mills are developed.

The mechanics of milling, in particular, with ball end cutters, are investigated in Chapter 4. Two different milling force models, the mechanistic and the mechanics of milling models, are presented. The mechanistic model requires direct estimation of cutting constants from milling experiments. The mechanics of milling is based on the oblique cutting mechanics model, which requires the milling cutter geometry, the shear stress, shear angle and average friction coefficient for the prediction of cutting forces. The mathematical models have been experimentally verified along with their statistical evaluation.

In Chapter 5, the dynamics of the milling process is modeled. The general model considers structural vibrations, chip thickness regeneration, exact rigid body kinematics

of milling. The mechanics model presented in chapter 4 is integrated to the dynamic model. The combined model is able to predict cutting forces, surface finish and vibrations during ball end milling operations. The model predictions are compared with the experimental results.

The thesis is concluded with a short summary of the contributions and future research work.

Chapter 2

Literature Review

2.1 Overview

Milling is used extensively in the manufacturing industry where both precision and efficiency are critical. In this process the component shape, size and its surface finish is generated by systematically removing or 'cutting' the excess material from the original workpiece by a cutting tool. The milling cutter possesses a number of cutting edges. It is provided with a rotary motion and the work is gradually fed. Chips are removed by each cutting edge during revolution and a surface is produced. Milling is one of the most important manufacturing processes because it can produce a wide variety of component shapes and sizes with high dimensional accuracy and good surface finish, and it can be computer controlled and automated. In many of these operations the cutting force is an important parameter with respect to either the deflection (dimensional tolerance) and breakage of the cutter, or the stability of the process. Moreover, knowledge of the magnitude and variation of the cutting force with respect to the cutting conditions is essential for the process planning of milling operations.

Common milling geometries include conventional (up), climb (down), and slot milling. In the up milling process (figure 2.1 a), the chip thickness varies from zero to maximum. In down milling, the chip thickness starts from the maximum and decreases to zero at exit (figure 2.1 b). Down milling usually produces better surface finish since the shearing

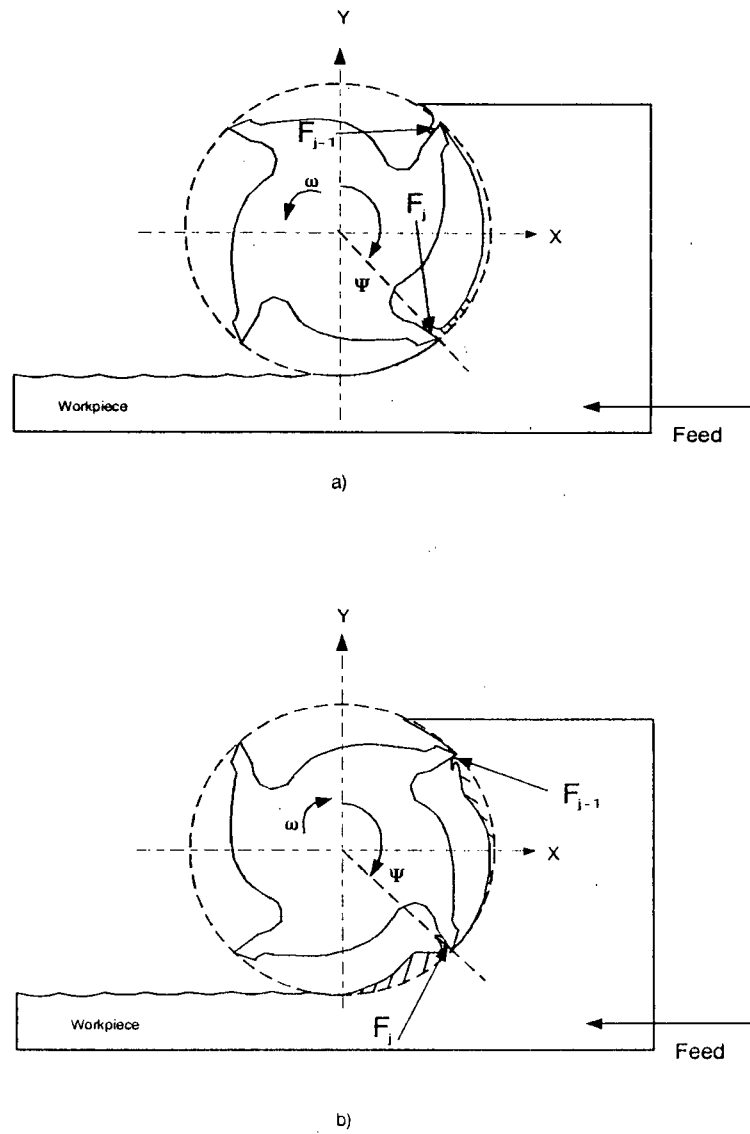


Figure 2.1: Common milling geometries: a) Up milling, b) Down milling

process ends at the finished surface. However, the directions of the resulting cutting forces are orientated in such a way that the cutter tends to be pushed away from the workpiece, leaving extra material on the surface, i.e. undercutting. Moreover, down milling produces higher shocks at the entry of the cut due to the abrupt change in chip thickness, thus requiring more gripping power from both the spindle and the clamps. In up milling, the shearing action begins at the finished surface, the cutter is always pushed in towards the workpiece, removing excess material from the desired surface dimensions. i.e. overcutting.

The mechanics of milling can be best understood by examining the chip formation during the process. An early detailed work by Martellotti [2] showed that, due to the combined rotational and linear feeding motions of the cutter towards the workpiece, the true path of a cutter tooth is an arc of a trochoid, rather than a circle, which complicates the mathematics in the analysis. However, Martellotti claimed that, in most practical cutting conditions where the cutter radius is much larger than the feed per tooth, the circular tooth path assumption is valid and the error introduced is insignificant. As the cutter rotates, the immersion angle (Ψ) varies, hence the chip load changes sinusoidally and given by Martellotti as:

$$t = s_t \sin(\Psi) \quad (2.1)$$

where t = instantaneous chip load

s_t = feed per tooth

Ψ = immersion angle of cutting point

2.2 Milling Force Models

The simplest form of machining operation is reviewed in this section. In the early 1940's Ernst and Merchant [3] presented a detailed analysis of a basic 2-D cutting process, often referred to as orthogonal cutting. Such an operation is realized when the cutting edge is straight and the relative velocity of the work and the tool is perpendicular to the cutting edge (figure 2.2 a). On the other hand, the term oblique cutting is used when the relative velocity of the work and the tool is not perpendicular to the cutting edge (figure 2.2 b).

The similarity between orthogonal and oblique cutting and their applications to milling will be detailed in the later sections. Some basic assumptions proposed by Merchant's model are:

1. A Type 2 (continuous) chip is formed.
2. The deformation is two dimensional without side spread of the chip.
3. Sharp cutting edge. (no edge force)
4. The thin shear zone is idealized by a 'shear plane'.
5. The shear stress τ in the 'shear plane' is uniform.

Merchant's analysis, whose diagrammatic representation is shown in figure 2.3, was based on the equilibrium of the chip under the action of friction forces at the rake face and shear forces in the 'shearing zone'. The tool face, with a rake angle α and clearance angle γ , penetrates into the work material at an uncut chip thickness t . The material shears along the shear plane and results in a cut chip with thickness t_c . The cutting ratio, r_c , is defined as:

$$r_c = t/t_c \quad (2.2)$$

The shear plane is inclined at an shear angle ϕ and is determined by the rake angle

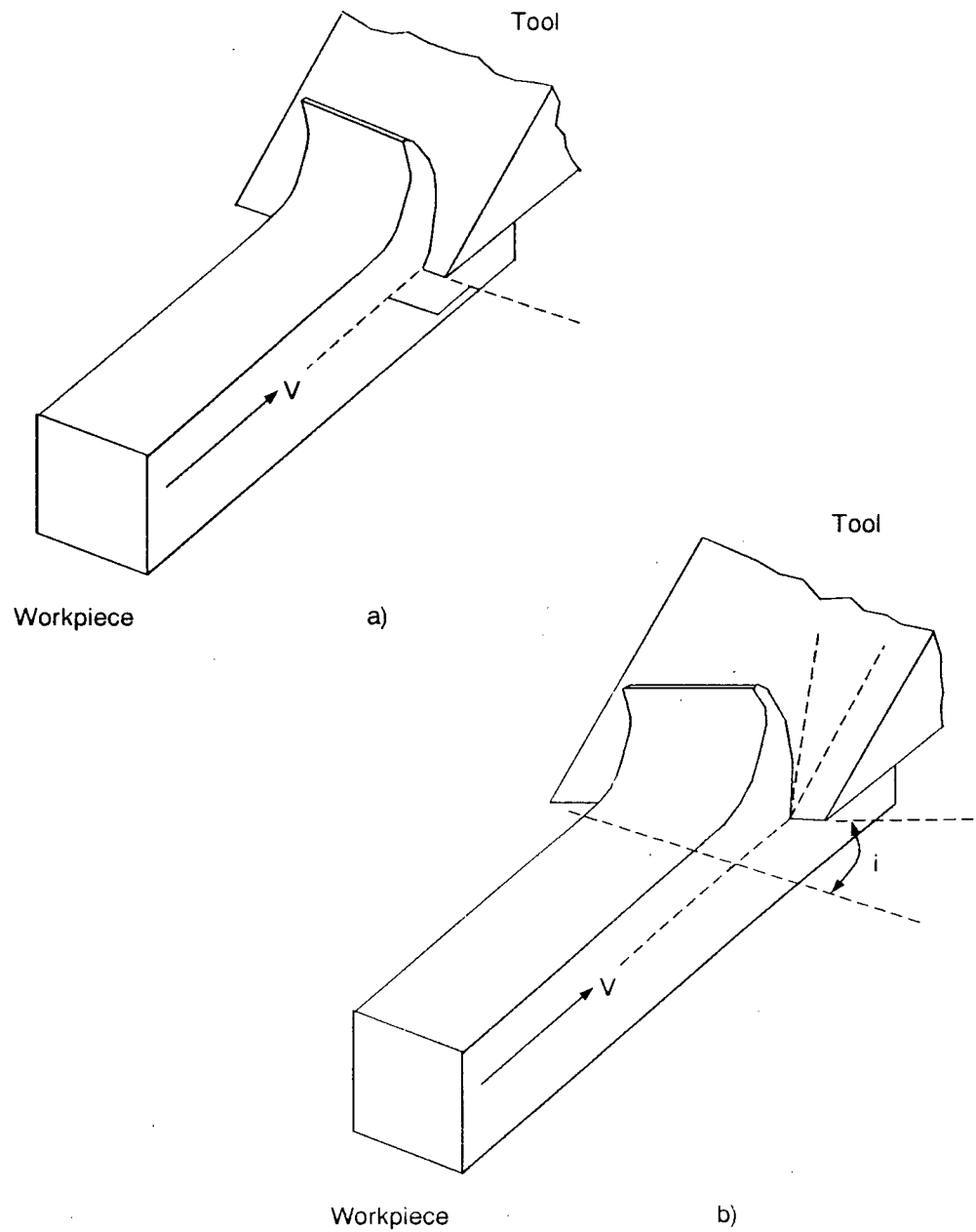


Figure 2.2: a) Orthogonal cutting geometry, b) Oblique cutting geometry

α_r of the tool and by the friction between the chip and the tool face.

$$\tan\phi = \frac{r_c \cos\alpha_r}{1 - r_c \sin\alpha_r} \quad (2.3)$$

The components of force found in the tool/chip interaction plane are the shear force F_s and the normal force F_n . In practice, these forces are resolved into directions parallel (F_c) and perpendicular (F_f) to the work velocity,

$$\begin{aligned} F_c &= F_s \cos\phi + F_n \sin\phi \\ F_f &= -F_s \sin\phi + F_n \cos\phi \\ F &= -F_c \sin\alpha_r - F_f \cos\alpha_r \\ N &= -F_c \cos\alpha_r + F_f \sin\alpha_r \end{aligned} \quad (2.4)$$

where the shearing force is assumed to be proportional to the chip area:

$$F = Ktb \quad (2.5)$$

where K and b are specific cutting pressure and width of chip respectively.

The above general relationship between the cutting force and the chip area was further explored and applied by many researchers in milling analysis. Their analyses attempted to relate the forces and power in milling to the practical variables such as the tool geometry and cut geometry as well as work material and deformation properties. Two commonly used milling force models are explained in the following:

2.2.1 Mechanistic Model

An early analysis of milling forces produced by a helical flute was presented by Koenigsberger et al. [4, 5, 6]. They related the elemental chip loading to rigid cutting forces (in

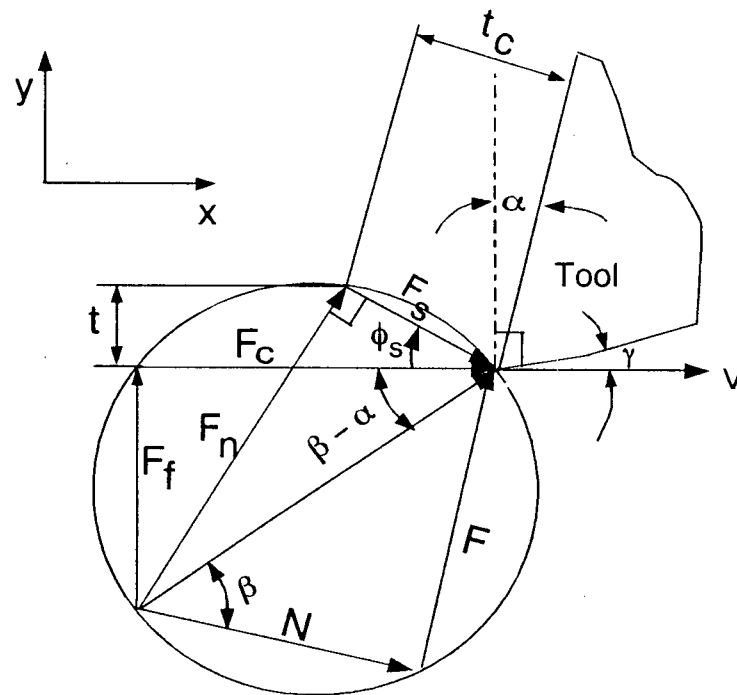


Figure 2.3: Force diagram in chip formation

tangential and radial directions) through experimentally calibrated milling force coefficients K_T and K_R . In general, these coefficients are identified through empirical curve fitting technique and provide little physical insight in terms of the nature of the process. The cutting forces were expressed as a function of cutting pressure exerted on the instantaneous uncut chip area:

$$\begin{aligned} F_t &= K_T * a * s_t \sin(\Psi) \\ F_r &= K_R * F_t \end{aligned} \quad (2.6)$$

Later, other researchers employed the same model with improvements such as including the effect of run out and tool deflections [7, 8, 9, 10, 11]. Tlustý and MacNeil [12], Yellowley [13], Armarego and Budak et al. [14] further improved the accuracy in predicting the milling force coefficients for cylindrical helical end mills by introducing an edge force component to their linear model.

The limitations of the mechanistic approach became apparent in recent research on milling with complex cutters such as ballend mills which have variable geometry in the axial direction. As a result, Lim and Feng [15] approximated the cutting force coefficients with a third degree polynomial which depends on the axial depth of cut. They then estimated the coefficients by iteratively curve fitting using average run-out values on the cutters. Similarly, Yucesan and Altintas [16] presented a semi-mechanistic model which predicts the shear and friction load distribution on the rake and flank faces of the helical ball end mill flutes. They used a complex mathematical model and identified the milling force coefficients through an empirical curve fit to measure average milling forces. The result is a set of cutter geometry and cutting condition dependent milling force coefficients, which limits the mechanistic model's applicability.

With the mechanistic model, prior evaluation of the milling force coefficients is necessary for any analysis and prediction. Moreover, a large amount of milling tests is required

to be run at different feed rates, cutting speeds, and constant cutting geometry, and the results are applicable to a particular workpiece material-cutter pair only. Although the model allows quick calibration of existing cutters, it is not practical and useful in the case of complex cutter such as ball end mill due to its variable geometry such as helix and rake angles.

2.2.2 Mechanics of Milling Model

Armarego [14, 17, 18] was among a few researchers to apply the orthogonal cutting theory on milling force predictions. The basic idea is to represent the milling geometry by segments of oblique cutting processes. Based on Merchant's thin shear zone theory, Armarego determined the milling force coefficients for cylindrical helical end mills without calibration tests. From Merchant's theory,

$$F_s = \tau b \frac{t}{\sin \phi} \quad (2.7)$$

By measuring the forces in turning, Budak, Altintas and Armarego [19] identified the traditional material properties such as shear strength and friction from a set of standard orthogonal turning test. They showed an accurate method of transformation between the orthogonal cutting parameters (i.e. shear stress, shear and friction angles) and local milling force coefficients, taking into consideration the cutter geometry such as helix angle and rake angle. Yang and Park [20] took a similar approach and applied the orthogonal theory on ballend mills. They obtained the fundamental cutting parameters from orthogonal turning tests and simplified the analysis by approximating the oblique cutting on each ballend flute by infinitesimal orthogonal processes. Later they considered the variation in the chip loads due to static tool deflections. Tai and Fuh [21] used a similar cutting model but they represented the cutting edge geometry as intersections

between skew planes and spherical ball end mill surface. Ramarji [22] applied a similar theory on taper shaped cutter by obtaining the shear stress from the stress-strain curve.

The mechanics of milling approach is more versatile to apply on cutters with complex geometries such as ballend and tapered ballend mills. Moreover, it eliminates the need for new calibration tests required for each new cutter geometry. It also gives more physical insight to the real process.

2.3 Dynamic Cutting

The milling models considered above deal with steady-state, static cutting, which is an ideal machining situation - where the structural vibrations during cutting are ignored. A cutting system is often subjected to some type of external dynamic forces. This forcing function can be time-dependent, harmonic, periodic, or random in nature. In dynamic milling, under some conditions, force induced vibrations may be inherent into the process, at the tooth passing frequency. For other conditions the vibration may cause the cutting process to vary so that it supplies a positive input of energy to maintain the vibration, which is known as self-induced or self-excited vibration in machining. Chatter is a self-excited type of vibration which occurs in metal cutting due to the lack of stiffness in the process, or can be best explained by a phenomenon called "regeneration of waviness". "Regeneration of waviness" is a mechanism by which the input force is modulated by system dynamics so as to produce force variations and vibration." [23]. Figure 2.4 shows an orthogonal cutting process where the relative vibration between the tool and the workpiece produces a "wavy" machining surface therefore influences the uncut chip thickness variation at the chatter frequency. This undulation affects the cutting forces which in turn excite the structure to produce vibrations and modulating the chip thickness more. Chatter vibrations occur around the natural frequency of the

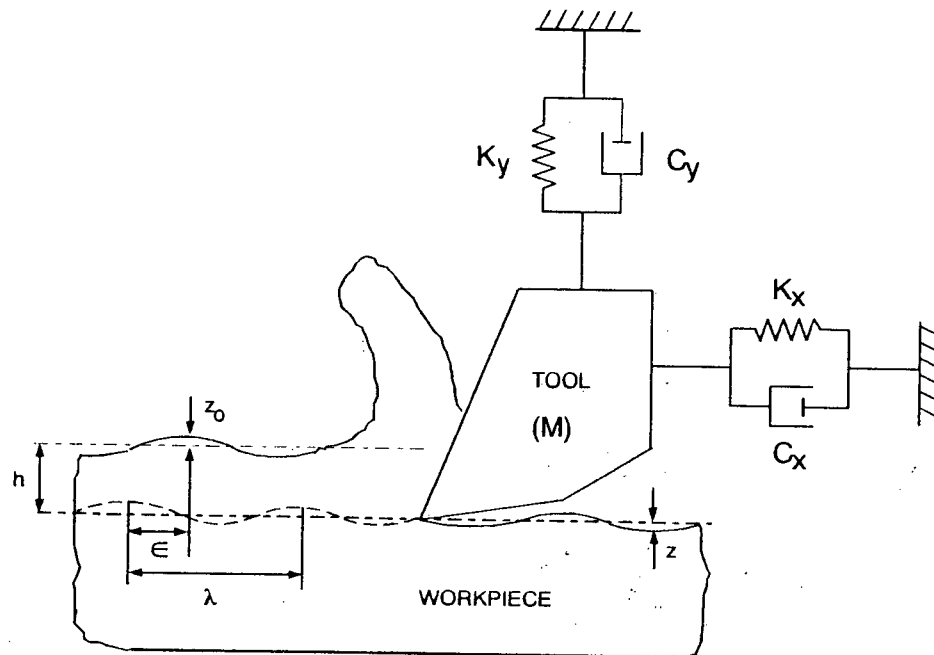


Figure 2.4: Dynamic Cutting and Wave Regeneration in Orthogonal Cutting

most flexible part of the machine tool-workpiece structure which is closest to the cutting point.

Chatter in machining requires in-depth analysis as the machine tool, the workpiece structure and the cutting process form a complex system. Severe vibrations in milling can lead to imperfections on the work surface as the tool impacts on the work and produces heavy marks or rough gouges. Chatter may also increase the rate of wear of the tool, the likelihood of machine-tool break down, and it may cause a high frequency sound which is unpleasant and can be physically harmful to nearby personnel.

Some of the main factors affecting the occurrence of chatter include: the structure of the machine tool and workpiece, the overall system stiffness, damping, material hardness, tool geometry, and orientation of tool vibration modes, and cutting conditions such as speed, depth and width of cut. In general, chatter can be prevented by stiffening the relative compliance between the tool/workpiece, or by selecting conservative cutting width and depth of cuts, but at the expense of productivity. The use of non-uniform pitch cutters in chatter suppression was also subjected to many investigations [24, 25]. The main idea is to disturb the normal wave regeneration mechanism which leads to self-excitation chatter.

Tobias [26, 27], and Tlustý [28] were among the few early researchers to study dynamic cutting. They explained the fundamental mechanism of chatter during turning and derived the stability theory which analytically predicts chatter free cutting conditions. Their stability theory was based on the orthogonal cutting model where the directions of cutting forces and the structural dynamics of the tool workpiece system were assumed constant. It was later adopted by many investigators and resulted in more understanding in chatter prediction and avoidance.

Chatter in milling, however, is different from turning in which the cutter rotates with

respect to the structure/workpiece system. The directions of the cutting force components and chip thickness are no longer constant but changed with respect to the cutter's coordinate, hindering the direct application of the time invariant chatter stability theory developed in turning. Sridhar [29] presented a milling stability model which requires numerical solution of the milling equation. Later Minis [30] proposed an improved method of solving the stability equation analytically by iteration. Recently, Budak et al. [31] have solved the chatter stability in milling for helical end mills. They represented the time varying milling force coefficients in Fourier series and were able to solve the stability equation analytically and more efficiently, taking into account the change in the milling force directions. However, the applicability of their theory has yet to be justified with other complex cutters such as ballend mills.

All of the above analytical models target towards a "chatter stability chart" which allows chatter-free cutting speed, axial and radial depth of cuts to be selected accordingly. Thusty et al. [32, 33] also took a different approach in understanding the dynamics and the stability of the process by introducing the time domain simulations of chatter vibrations in milling. They simulated the real machining process numerically by considering the speed dependent process damping, structural dynamics, and the nonlinearities signified by the tool jumping in and out of the workpiece due to excessive vibrations which cannot be modelled in the analytical stability theory. Altintas and Montgomery [1] presented an improved simulation model, including the true kinematics of the tool and workpiece motions and the tool interference with the workpiece. In general, the time domain chatter simulation provides a useful and reliable tool in predicting chatter free cutting conditions. Chatter vibrations in ball end milling, however, have not received a similar attention due to its complex geometry and dynamic chip load generation mechanism.

Chapter 3

Geometric Modelling of Milling Cutters

3.1 Introduction

A large variety of milling tools are available and used in die and mold manufacturing. Each cutting edge on the tool is carefully designed to ensure maximum cutting performance while minimizing the resulting cutting forces. A detailed analysis of the cutting edge geometry is also necessary for the development of the force model. The important characteristics of milling tools are the macro geometry (cylindrical, ball-end, bull-nose, tapered ball-end mills. etc.), the micro geometry (helix angle, rake angle, relief angle, ball radius. etc.), the cutting material (carbide, HSS and PCBN), and coating material (e.g. TiN, TiAlN).

In general, several aspects are considered concerning the cutting edge geometry:

- A positive rake angle improves the shearing and cutting actions and decreases the forces, but weakens the wedges and more susceptible to wear and breakage.
- High helix angle "smoothens" and reduces the impact force during entry cutting.
- Presence of clearance angle reduces the rubbing on the machine surface thus improves the surface finish, but at the expense of weakening the wedge and more importantly, reduces process damping and increases the likelihood to chatter vibrations. A second clearance angle may be provided to reduce the amount of grinding during sharpening.

One common approach in modelling complex milling cutters is by numerical method.

The tool and its cutting edge geometry are discretized and recorded by a coordinate measuring device, and the data is used to construct the curve through fitting. This method requires extensive computational time and vast amount of data to be stored. Moreover, the same data cannot be applied to any other design or in the case of regrinding of the cutting edge shape. Therefore, simple mathematical models are desirable which would increase the accuracy of the mechanistic model. Such models would also eliminate the need for extensive testing to determine the functional relationship of model parameters. The following section will begin by examining the geometric modelling of four practically used milling cutters, as shown in Figure 3.1.

3.1.1 Modelling of Cylindrical End Mill

Figure 3.1.a shows the common nomenclature for a helical end mill with N_f teeth. Each flute is inclined at a constant helix angle i_0 and the immersion angle for flute j changes along the axial direction. For cylindrical cutters which have a constant radius and helix angle, the immersion angle varies linearly with the height. At a height of z , the angular position Ψ of a cutting point on flute j can be described as:

$$\Psi_j(z) = \theta + (j - 1)\phi_p - \frac{z}{R_0} \tan i_0 \quad (3.1)$$

where R_0 is the cutter radius, $\phi_p = 2\pi/N_f$ is the cutter pitch angle. θ is the base angle of the reference flute in global coordinate system.

It should be noticed that, the cutting action on a milling cutter with straight edges is equivalent to orthogonal cutting with a tool having the same rake angle. Similarly, a helical cutting edge on the cutter is equivalent to an oblique tool with an inclination angle i_0 . The application of the geometric similarity between the two processes will become apparent in the derivation of the milling force coefficients in chapter 4.

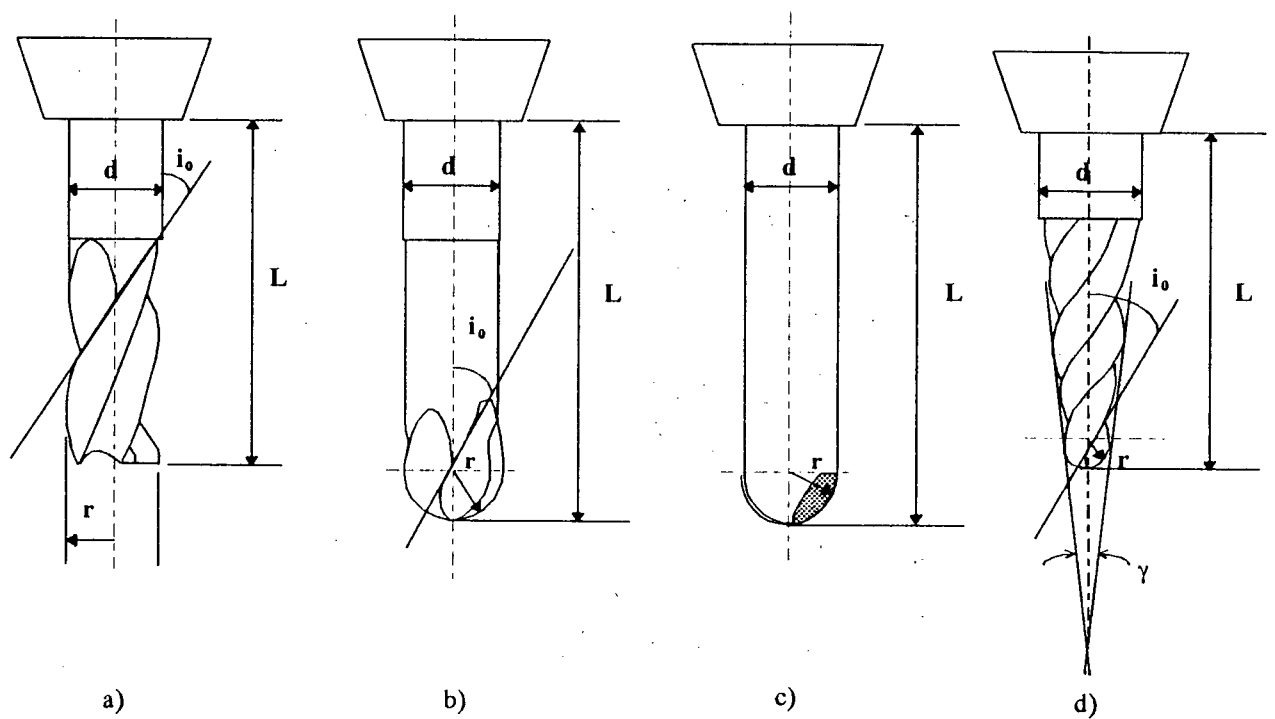


Figure 3.1: a) Cylindrical End Mill, b) Ballend Mill, c) Bullnose Mill, d) Tapered Ballend Mill

3.1.2 Modelling of Ballend/Bullnose Mill

With ballend and bullnose end mills, the exact description of the cut geometry is complicated because the points along the cutting edge generate trochoid curves. Thus, there are complex relationships between the machining parameters (feed per tooth, depth and width of cut) and technological parameters (chip thickness and cutting cross section). In most cases, those relationships can only be found using numerical methods.

Another important difference between using ballend mills and end mills in machining is the speed of material removal or the cutting speed. A ball end mill cuts at a portion of the sphere near the axis of rotation and thus has various cutting speeds. With end-mills, however, the material is always cutting at the periphery of the cutter at a constant cutting speed.

A bullnose milling cutter (shown in Figure 3.1.c) has vertical cutting edges and each flute lies on the envelope of the hemisphere. Due to its zero helix angle, any cutting point on the same flute j has a constant angular position ψ ,

$$\Psi_j = \theta + (j - 1)\phi_p \quad (3.2)$$

and the height z can be expressed in terms of the angle κ between the cutting point and the z -axis in the vertical plane as,

$$z = R_0(1 - \cos\kappa) \quad (3.3)$$

The parametric equation of cutting edges with non-zero helix angle is more complicated (figure 3.1.b). The detailed geometry of a helical ball end milling cutter is shown in Figure 3.2 a-d. Each flute lies on the surface of the hemisphere, and is ground with a constant helix lead. The flutes have a helix angle of i_0 at the ball-shank meeting boundary (figure 3.2.a). Due to the reduction of radius at $(x - y)$ planes towards the ball tip

in axial (z) direction, the local helix angle $i(\psi)$ along the cutting flute varies for constant helix-lead cutters. The expression for the envelope of the ball part is given by,

$$x^2 + y^2 + (R_0 - z)^2 = R_0^2 \quad (3.4)$$

where R_0 is the ball radius of the cutter measured from the center of the sphere (C). The cutter radius in $x - y$ plane at axial location z is,

$$R^2(z) = x^2 + y^2 \quad (3.5)$$

and it is zero at the ball tip. The z coordinate of a point located on the cutting edge is,

$$z = \frac{R_0 \psi}{\tan i_0} \quad (3.6)$$

where ψ is the lag angle between the tip of the flute at $z=0$ and at axial location z , and it is due to the helix angle. ψ is measured clockwise from $+y$ axis, see Figure 3.2.b. The center of the local coordinate system coincides with the global coordinate system X-Y-Z on the dynamometer shown by ball tip point 0 in the figure.

For cutters which have constant lead length, the local helix angle is scaled by a radius factor and can be expressed as,

$$\tan i(\psi) = \frac{R(\psi)}{R_0} \tan i_0 \quad (3.7)$$

From the equations given above, the cutter radius in $x - y$ plane, which touches a point on the helical and spherical flute located at angle ψ , can be expressed as,

$$R(\psi) = R_0 \sqrt{1 - (\psi \cot^2 i_0 - 1)^2} \quad (3.8)$$

A vector \vec{r} is drawn from the cylindrical coordinate center (C) to a point on the cutting edge and defined by,

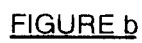
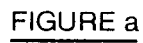


Figure 3.2: a-d Geometric model of Ballend cutter

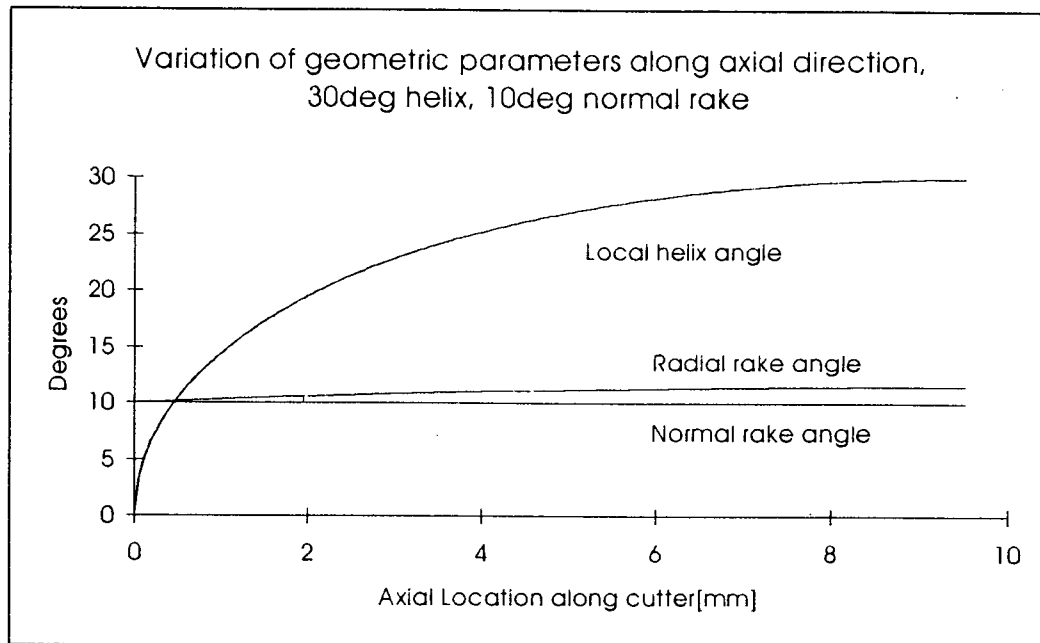


Figure 3.3: Geometric parameters along ballend cutter

$$\vec{r}(\psi) = R(\psi)(\cos \psi \vec{i} + \sin \psi \vec{j}) + R_0 \psi \cot i_0 \vec{k} \quad (3.9)$$

The length of an infinitesimal curved cutting edge segment, dS along the ball part is computed from,

$$dS = \| d\vec{r} \| = \sqrt{(R'(\psi))^2 + R^2(\psi) + R_0^2 \cot^2 i_0} d\psi \quad (3.10)$$

where $R'(\psi)$ is the derivative of $R(\psi)$

$$R'(\psi) = \frac{-R_0(\psi \cot i_0 - 1) \cot i_0}{\sqrt{1 - (\psi \cot i_0 - 1)^2}} \quad (3.11)$$

From Figure 3.2.c, the radial rake α_r and relief angle α_f are both defined in x-y plane and the normal rake angle α_n is measured on a plane passing through the cutting point and center of the ball, see Figure 3.2.a.

Figure 3.3 shows the variation of helix angle, normal and radial rake angle in the axial direction along a flute. As formulated, the local helix angle i approaches the nominal helix angle i_0 at the ball-shank meeting point, i.e. $z = R_0$. A point on the flute j at height z is referenced by its angular position Ψ in global coordinate system,

$$\Psi_j(z) = \theta + (j - 1)\phi_p - \frac{z}{R_0} \tan i_0 \quad (3.12)$$

where R_0 is the ball radius, $\phi_p = 2\pi/N_f$ is the pitch angle of the cutter, and θ is the rotation angle of reference flute $j = 1$. θ is measured clockwise from y -axis, and from the center point O.

3.1.3 Modelling of Tapered Ballend Mill

Tapered ballend mills (Figure 3.1.d) are widely used in manufacturing components with low curvature surfaces such as those encountered with turbine and compressor blades.

There are two commonly used tapered end mill, each possesses slightly different cutting edge geometry. A constant lead tapered mill has constant pitch but variable helix angle along the cutting edge due to the change in radius, while a constant helix tapered mill has a smaller pitch at the tip but larger pitch closer to the shank.

The parametric equation describing the cutting edge on a constant lead tapered mill is given by,

$$R(\psi) = R_0(1 + \psi \cot i_0 \tan \gamma) \quad (3.13)$$

Similar to the equations developed for ball end mills, the position angle ψ defines the position of any point on a cutting edge. R_0 is the radius of the cutter at the tip, i_0 is the helix angle at the tip and γ is the half-apex tapered angle. These cutters are usually combined with ball shaped flutes and referred to as tapered ballend mill. The equation of the cutting edge on the taper part which starts at ψ_{a0} is,

$$R(\psi) = R_0[1 + (\psi - \psi_{a0}) \cot i_0 \tan \gamma] \quad (3.14)$$

where ψ_{a0} , representing the ball/taper intersection point, is obtained by substituting ($z = R_0$) into Eq. (3.6), resulting in

$$\psi_{a0} = \tan i_0 \quad (3.15)$$

3.1.4 Cutting Geometry and Chip Thickness Calculation

During cutting, the tool edge penetrates into the workpiece material and removes a chip section which runs along the rake face. The chip thickness prediction is a key to milling analysis as the instantaneous cutting forces are proportional to the cross-sectional chip thickness at each tooth edge and its maximum value is always a good indication of the process load. Unlike in turning where the chip thickness is always constant and can be

set directly, the chip thickness varies in milling and, in general, depends on the workpiece geometry, the tool location and geometry, and the cutting parameters such as the axial depth of cut and the feed direction simultaneously. The following section summarizes the solutions to the chip thickness prediction of simple milling operations. Later in chapter 5, a more accurate numerical model which incorporates the exact kinematics of the process will be compared against the closed form solutions.

For example, Figure 3.4 shows a typical milling operation where the cutter periphery is in full contact with the workpiece, and the workpiece is fed perpendicularly towards a rotating cutter in the feed (x) direction, the actual shape of an undeformed chip is rather complex as the cutting edge traverses a trochoidal path proven by Martellotti [2].

$$t_n = \frac{R_0 s_t \left\{ \frac{R_0 + \frac{2}{3} \left[\frac{v}{2\pi N} \cos^{-1} \left(\frac{R_0 - d}{R_0} \right) - s_t \right]}{\frac{v}{2\pi N} + R_0 - \frac{2}{3} s_t} \right\} \sin \left[\frac{R_0 + \frac{v}{2\pi N} \cos^{-1} \left(\frac{R_0 - d}{R_0} \right) - s_t}{\frac{v}{2\pi N} + R_0 - \frac{2}{3} s_t} \right]}{\sqrt{\left(\frac{v}{2\pi N} \right)^2 + R_0^2 + \frac{v}{\pi N} R_0 \cos \left[\frac{(\frac{v}{2\pi N} + R_0) \cos^{-1} \left(\frac{R_0 - d}{R_0} \right) - s_t}{\frac{v}{2\pi N} + R_0 - \frac{2}{3} s_t} \right]}} \quad (3.16)$$

The above expression, although it accounts for the continuous motions of both the cutter and the workpiece, is too complex to be applied in practice. Various approximations, such as assuming a circular tooth path, or neglecting the effect of the table feeding term $(v/2\pi N)^2$ in the expression, have been made to give the most commonly used chip thickness expression in milling analyses, i.e.

$$t(\psi, \theta) = s_t \sin(\Psi) \quad (3.17)$$

In practice, the cutting speed is much greater than the table feeding speed and the above equation gives good prediction of the chip thickness in the x - y plane, normal to the cutting edge in the case of cylindrical cutters. In ballend/bullnose milling, the chip thickness normal to the cutting edge on the spherical surface, denoted by t_n , is a function of both the radial position angle θ and the axial angle κ as shown in Figure 3.2 d,

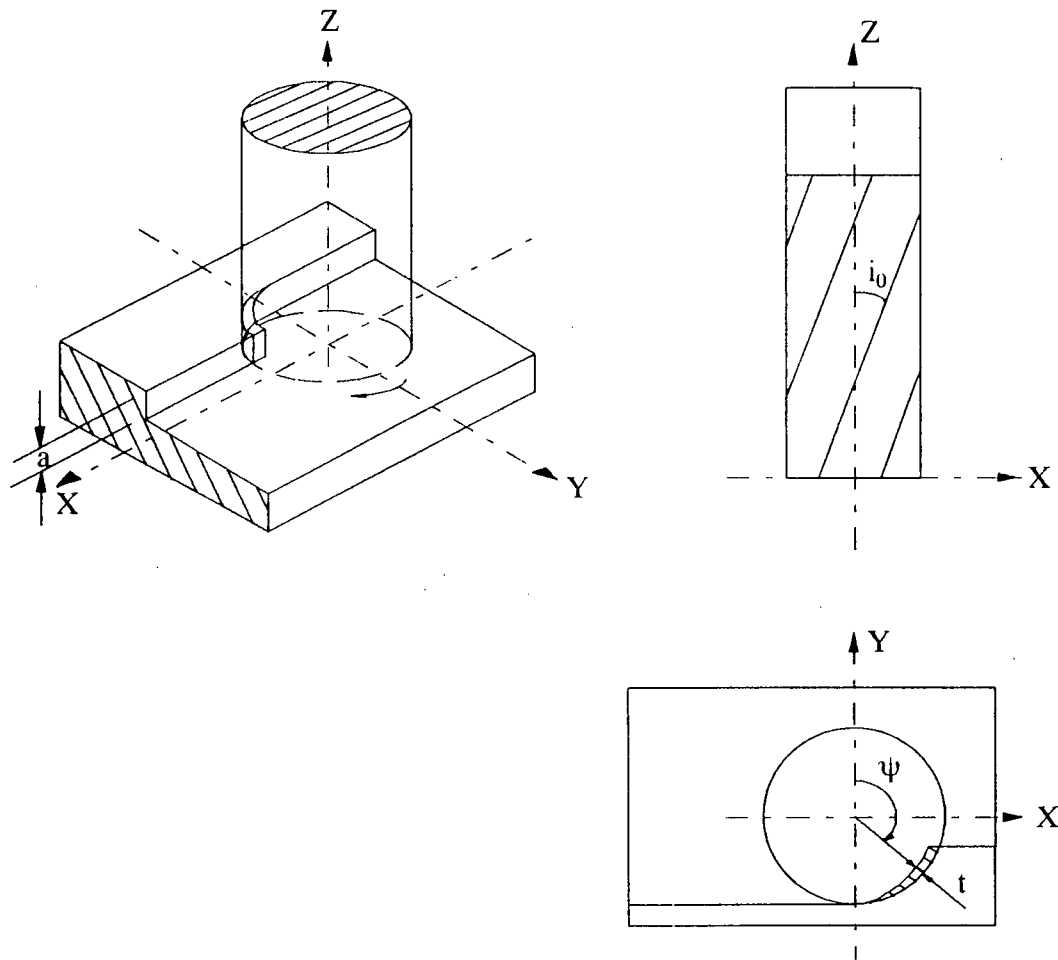


Figure 3.4: Common milling geometry and chip formation

$$t_n(\psi, \theta, \kappa) = s_t \sin(\Psi) \sin(\kappa) \quad (3.18)$$

where

$$\kappa = \sin^{-1} \frac{R(\psi)}{R_0} \quad (3.19)$$

The two chip thickness formulations (Eq. 3.16 and Eq. 3.17) are plotted in Figure 3.5 at two cutter locations ($z = 0.1R_0$ and $z = 0.25R_0$). The radius of the cutter is 10mm and the feed rate is 0.127mm/tooth . From the figure, it can be seen that, the error introduced by the above analytical chip thickness expression is significant only in areas around the ball tip. Hence, the use of exact kinematic model of chip thickness formulated by Martelotti will not significantly improve the results when the axial depth of cut is not too small.

The chip thickness in other unconventional milling operations, for instance, when the workpiece geometry and the cutter orientation vary, requires a much involved analyses. Analytical solution is usually not possible as the tool/part engagement limit can become irregular and has to be identified with the available solid modelling system [34].

3.2 Conclusions

In this chapter several common milling cutter geometries, in particular, ballend mills, were thoroughly investigated. An analytical model of the spiral edge on the ballend was developed. It considers the chip thinning effect, variable helix angle and changing cutting speeds which are unique in ballend milling. The use of simplified chip thickness formulation was justified and the error was found to be insignificant except at very low axial depth of cut. The derived cutter geometries and the helical cutting edge orientation will be used to formulate the cutting forces during the dynamic milling process in the following chapter.

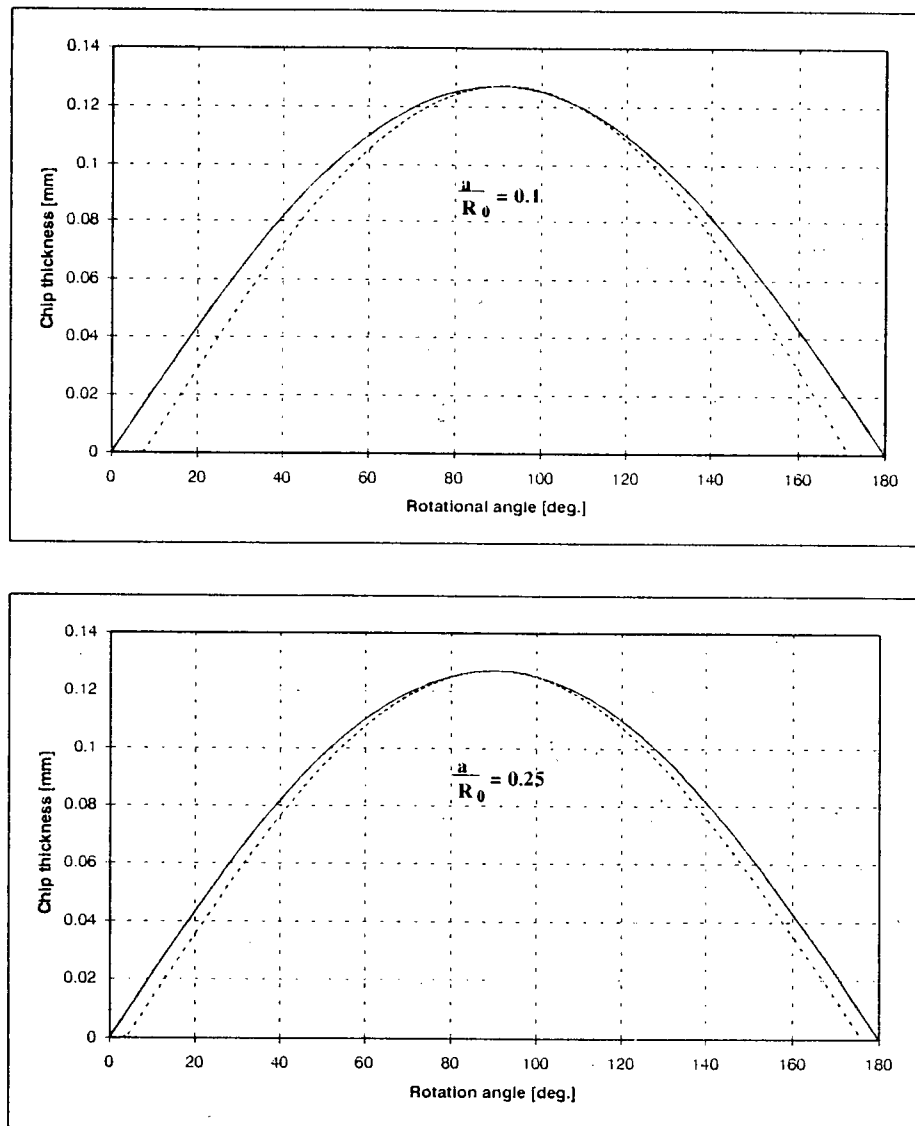


Figure 3.5: Chip Thickness Profile at two cutter locations, solid line - approximation, dotted line - exact kinematics

Chapter 4

Modelling of Milling Forces

4.1 Introduction

In the machining of complex and costly parts such as those involved in aircraft or die and mold industries, prior knowledge of the milling forces, surface form errors and chatter vibrations is essential to assist engineers in designing machine tools, jigs and fixtures. It can also help them in selecting economic cutting conditions to reduce tool deflection and chatter vibrations which affect the surface quality of the finished parts. For instance, if the chip load is selected to be too large, the forces cause chipping of the cutting edge or even tool breakage, while a small chip load will increase the percentage of deformation and friction action in the process which leads to higher temperatures, abrasive wear, and poor surface quality. The basic difference between predicting cutting forces from empirical testing and metal cutting theory is that in the former, tests are required for the specific cutting operations and the approach usually considers the influence of practical rather than fundamental variables. Therefore, it may be difficult to apply data from one process to another. The second approach, which involves a more detailed analysis and testing procedure, aims at determining the fundamental machining parameters which may be useful in solving various cutting processes.

Many investigations have been made into the nature of the cutting forces during milling [4, 12, 35, 34]. Cutting forces are evaluated in the following way, a complete representation of the chip load on the end mill at any instant is obtained by integrating

the chip area on the cutter by considering thin disc-like sections along the axis of the cutter. The location of each section is first determined and for each flute engaged in the cut, the chip thickness times the chip width yields the chip load. As the angular position of the cutter changes, the chip load is recomputed. Traditionally, cutting force coefficients are calibrated experimentally for a particular tool/workpiece set through empirical curve fitting techniques in which polynomial regression models are developed to relate the average chip load to measured average forces. The milling force coefficients are then applied in an analytical model which predicts the cutting forces produced by the same cutter in other machining conditions. The mechanistic approach described above usually results in simple formulation and accurate predictions in the cases with cutters of simple geometry such as cylindrical end mills or face mills. However, it suffers a few shortcomings. For cutters with complex geometry, such as ballend mills where the cutting edge geometry changes in the axial direction, the applicability and flexibility of the mechanistic approach will be greatly reduced. More calibration tests are required since the milling force coefficients become functions of multiple geometry factors.

A second approach deals with the unified mechanics of cutting was first presented by Armarego [14, 17, 18]. Each cutter tooth is partitioned into a series of axial elemental oblique tools. Then the cutting geometry of each in-cut tooth element is identified and thin shear zone mechanics of cutting analyses are applied to obtain the resultant force. This mechanics of milling approach, which results in the estimation of the milling force coefficients from orthogonal machining data, will be studied, and applied in this chapter, to milling force prediction with ballend cutters.

4.2 Milling Force Models

Two milling force models will be presented here. The average force model, which involves calibration of each milling cutter prior to the predictions, and the mechanics of milling approach, which is more suitable to apply on cutters with complex geometries.

4.2.1 Mechanistic approach with Average Force Model

It has been shown by Sabberwal [4, 35] that force predictions may be made by considering the tangential cutting force to be proportional to the chip load and the radial force proportional to the tangential force,

$$dF_t = K_T t_c da_z \quad (4.1)$$

$$dF_r = K_R dF_t \quad (4.2)$$

where dF_t is the tangential force on a disc element,

dF_r is the radial force on a disc element,

da_z is the thickness of the axial discs,

t_c is the chip thickness from Eq. (3.17), and

K_T, K_R are milling force coefficients.

One common method used in estimating the milling force coefficients is to assume average values at all the cutting points. This allows the above integrations to be evaluated analytically. Average force expressions are obtained and the values for K_T and K_R may then be solved by relating the expressions to the measured average forces. The milling force coefficients, in general, vary with the machining conditions. For cutters with simple

geometry such as cylindrical end mills, it has been shown that, they are strong functions of the average chip thickness [36]. Therefore, empirical models are developed to predict them as functions of the average chip thickness. The above model is modified and adapted to ballend milling in the following section.

The geometry of a cutting edge on the ballend cutter was shown in Figure 3.2 c. A set of curvilinear coordinate system normal to the ball envelope is used to specify the resultant cutting forces acting on the flute. The elemental tangential, radial, and axial cutting forces dF_t, dF_r, dF_a acting on the cutter are given by

$$\begin{aligned} dF_t(\theta, z) &= K_{te}dS + K_{tc}t_n(\theta, \psi, \kappa)db \\ dF_r(\theta, z) &= K_{re}dS + K_{rc}t_n(\theta, \psi, \kappa)db \\ dF_a(\theta, z) &= K_{ae}dS + K_{ac}t_n(\theta, \psi, \kappa)db \end{aligned} \quad (4.3)$$

where $t_n(\theta, \psi, \kappa)$ is the uncut chip thickness normal to the cutting edge, and varies with the position of the cutting point. The cutting forces are separated as edge (e) and shear cutting (c) components. The edge force coefficients (K_{te}, K_{re}, K_{ae}) are in [N/mm], constant and lumped at the edge of the flutes. dS is the differential length of the curved cutting edge segment given by Eq. (3.10). In the mechanistic approach, the shearing coefficients K_{tc}, K_{rc}, K_{ac} are identified from a set of standard milling tests with the same cutter and workpiece.

The resultant forces in Cartesian coordinates are obtained by introducing the transformation matrix T

$$\{\mathbf{dF}_{xyz}\} = [T]\{\mathbf{dF}_{rta}\} \quad (4.4)$$

$$\begin{bmatrix} dF_x \\ dF_y \\ dF_z \end{bmatrix} = \begin{bmatrix} -\sin(\kappa)\sin(\Psi) & -\cos(\Psi) & -\cos(\kappa)\sin(\Psi) \\ -\sin(\kappa)\cos(\Psi) & \sin(\Psi) & -\cos(\kappa)\cos(\Psi) \\ \cos(\kappa) & 0 & -\sin(\kappa) \end{bmatrix} \begin{bmatrix} dF_r \\ dF_t \\ dF_a \end{bmatrix}$$

The total cutting forces acting on one flute with an axial depth of cut z :

$$\{\mathbf{F}\} = \int^z d\mathbf{F} \quad (4.5)$$

where the differential force components are dependent on the engaged flute segment length dS , instantaneous chip load $t_n(\psi, z, \kappa)$, the local rotation (θ) and lag angle (ψ).

$$\left. \begin{aligned} F_{xj}[\theta(z)] &= \int_{z_1}^{z_2} (-dF_{rj} \sin(\kappa_j) \sin(\Psi_j) - dF_{tj} \cos(\Psi_j) - dF_{aj} \cos(\kappa_j) \sin(\Psi_j)) dz \\ F_{yj}[\theta(z)] &= \int_{z_1}^{z_2} (-dF_{rj} \sin(\kappa_j) \cos(\Psi_j) + dF_{tj} \sin(\Psi_j) - dF_{aj} \cos(\kappa_j) \cos(\Psi_j)) dz \\ F_{zj}[\theta(z)] &= \int_{z_1}^{z_2} (dF_{rj} \cos(\kappa_j) - dF_{aj} \sin(\kappa_j)) dz \end{aligned} \right\} \quad (4.6)$$

When the helix angle is zero, i.e. straight cutting edges as in bullnose cutters, the lag angle (ψ) is constant for each flute and it is possible to integrate the above expressions analytically to obtain a close form solution for the cutting forces. However, in that case, constant milling coefficients are assumed.

The integrations given above are calculated numerically by evaluating the contribution of each discrete cutting edge element at dz intervals. However, geometric considerations must be taken when the edge segment is outside the immersion zone. i.e. If the edge is not in contact with the workpiece, the contribution to the cutting forces is zero.

Assuming *average* milling force coefficients $\overline{K_{te}}, \overline{K_{ac}}, \overline{K_{rc}}$ along the cutter axis, the above integral can be evaluated and averaged over one revolution of the cutter.

$$\left. \begin{aligned} \overline{F_x} &= \overline{K_{re}} I_{rex} + \overline{K_{rc}} I_{rcx} + \overline{K_{te}} I_{tex} + \overline{K_{tc}} I_{tcx} + \overline{K_{ae}} I_{aex} + \overline{K_{ac}} I_{acx} \\ \overline{F_y} &= \overline{K_{re}} I_{rey} + \overline{K_{rc}} I_{rcy} + \overline{K_{te}} I_{tey} + \overline{K_{tc}} I_{tcy} + \overline{K_{ae}} I_{aey} + \overline{K_{ac}} I_{acy} \\ \overline{F_z} &= \overline{K_{re}} I_{rez} + \overline{K_{rc}} I_{rcz} + \overline{K_{te}} I_{tez} + \overline{K_{tc}} I_{tcz} + \overline{K_{ae}} I_{aez} + \overline{K_{ac}} I_{acz} \end{aligned} \right\} \quad (4.7)$$

where I_{rei} and I_{rci} ($i = x, y, z$) are functions of geometric variables such as local radius and immersion angle. They have to be evaluated numerically. The above expressions for the average forces are assumed to be constant over a complete revolution of the cutter. As proved by Whitfield [37], the helix angle does not have any effect on the average forces since the total amount of chip load remains constant in every revolution. Thus the milling force coefficients can be estimated, by applying least squares minimization technique, for each axial depth of cut, and as functions of average chip load and cutting speed.

Determination of Edge Force Coefficients: The average forces are obtained from experiment and plotted against the chip thickness and axial depth of cut as shown in Figure 4.1. Then the edge forces are obtained by extrapolating the measured average forces to zero chip thickness (Figure 4.2). A finite average force value at zero chip thickness reflects the existence of a secondary ‘rubbing’ process. The average edge force coefficients K_{te}, K_{re}, K_{ae} represent the rubbing forces per unit width, normalized with respect to the flute length¹. Past research show that the edge forces do not depend heavily on feed rate [16].

¹The in-cut flute length is obtained by integrating dS in Eq. (3.10) numerically

The effect of cutting speed has on the edge force coefficients is investigated by conducting tests at similar cutting conditions but with different spindle speeds. Although the cutting speed varies in each test due to varying cutter radius, results show that [31], the edge forces do not vary significantly with cutting speeds for the particular workpiece material (*Ti6Al4V*) used here.

The cutting components of the average forces are used in the evaluation of the cutting force coefficients. Results are plotted and shown in Figure 4.3. It can be seen that, due to variable cutting geometry along the axis of the cutter, the cutting force coefficients are strong functions of both the chip load and the axial immersion of the cutter. As a result, high order polynomial curve fitting technique is required to calibrate the coefficients for different axial depths. Due to the limited use of the mechanistic approach, the identification procedure will be kept outside the scope of this work. Similar works can be found in references [15, 16].

It can be seen that, the mechanistic approach requires vast amount of cutting data for each new cutter geometry and more importantly, the data cannot be generalized to be applied on other cutters as there is no explicit relationship between the tool geometry, cutting conditions, and the cutting force coefficients. Moreover, the empirical polynomial fitting does not give physical insight, for instance, the shearing resistance and the friction, in the process.

4.2.2 Mechanics of Milling Model

The mechanistic approach used in the previous section involves empirical curve fitting and assumes constant and average values which may not be suitable to be applied on cutters with complex geometry as the cutting force coefficients (K_{tc} , K_{ac} , K_{rc}) may be dependent on the local cutter geometry and cutting geometry (i.e. local chip thickness). In this section a mechanics of cutting analysis for the milling operation with complex

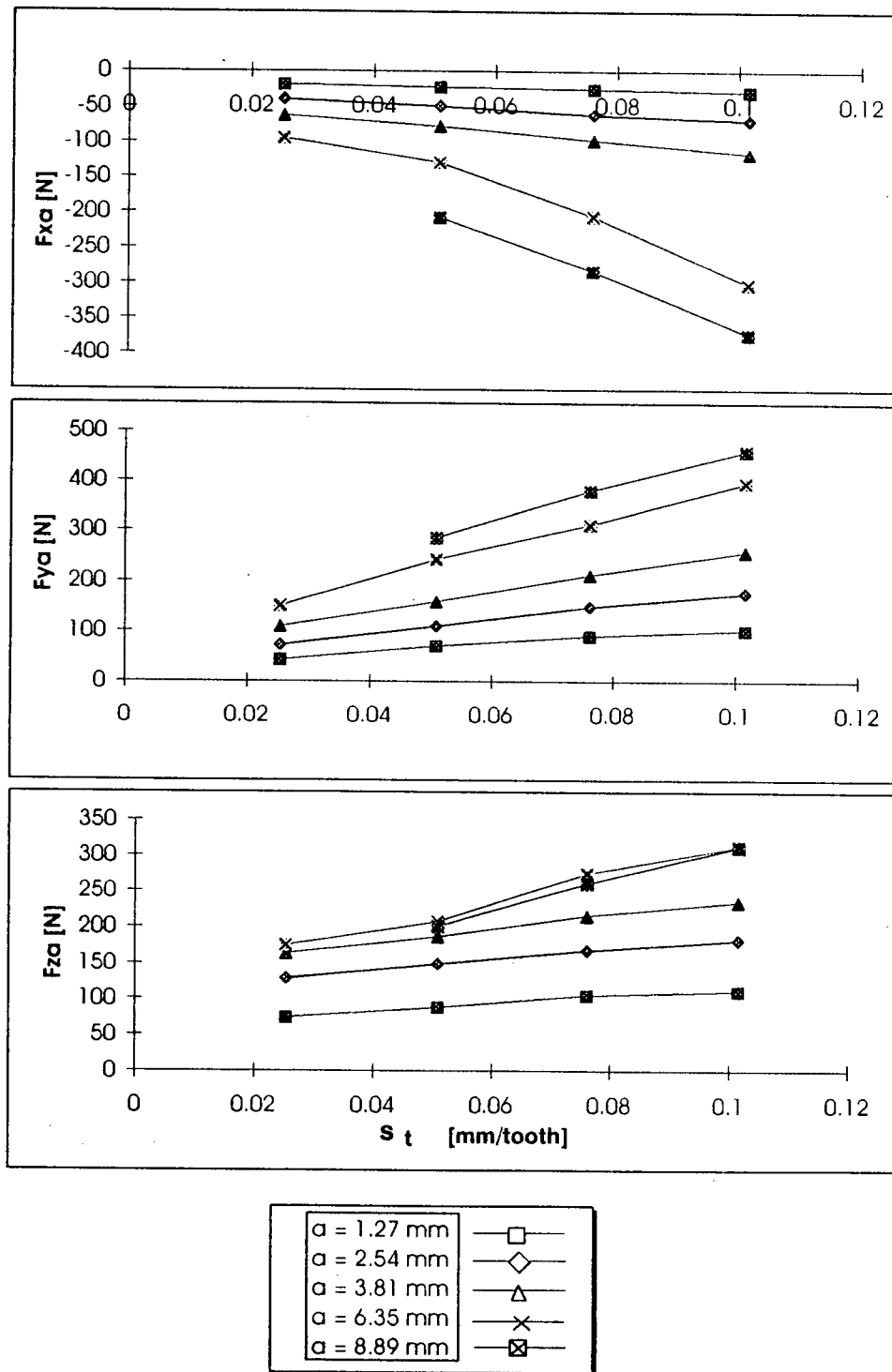


Figure 4.1: Average Forces vs Feed rate for different axial depth of cuts in ballend milling

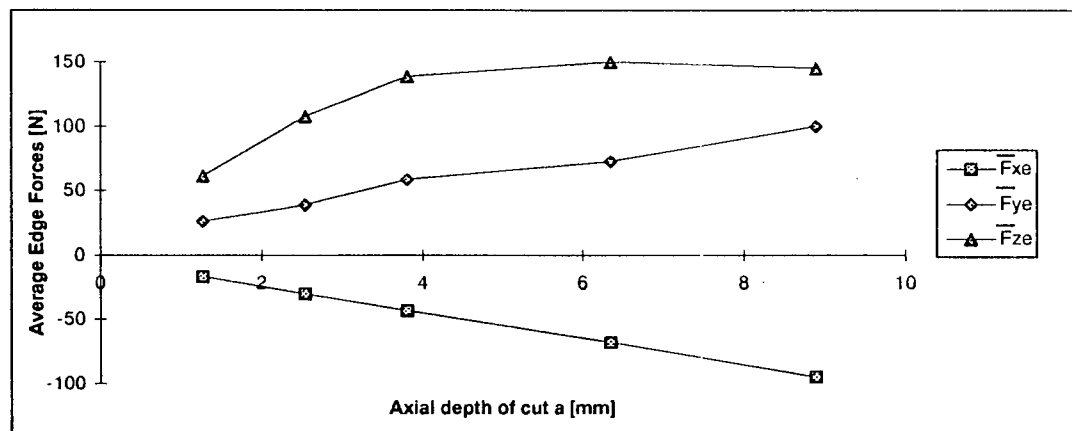


Figure 4.2: Average Edge Forces vs axial depth of cut in ballend milling

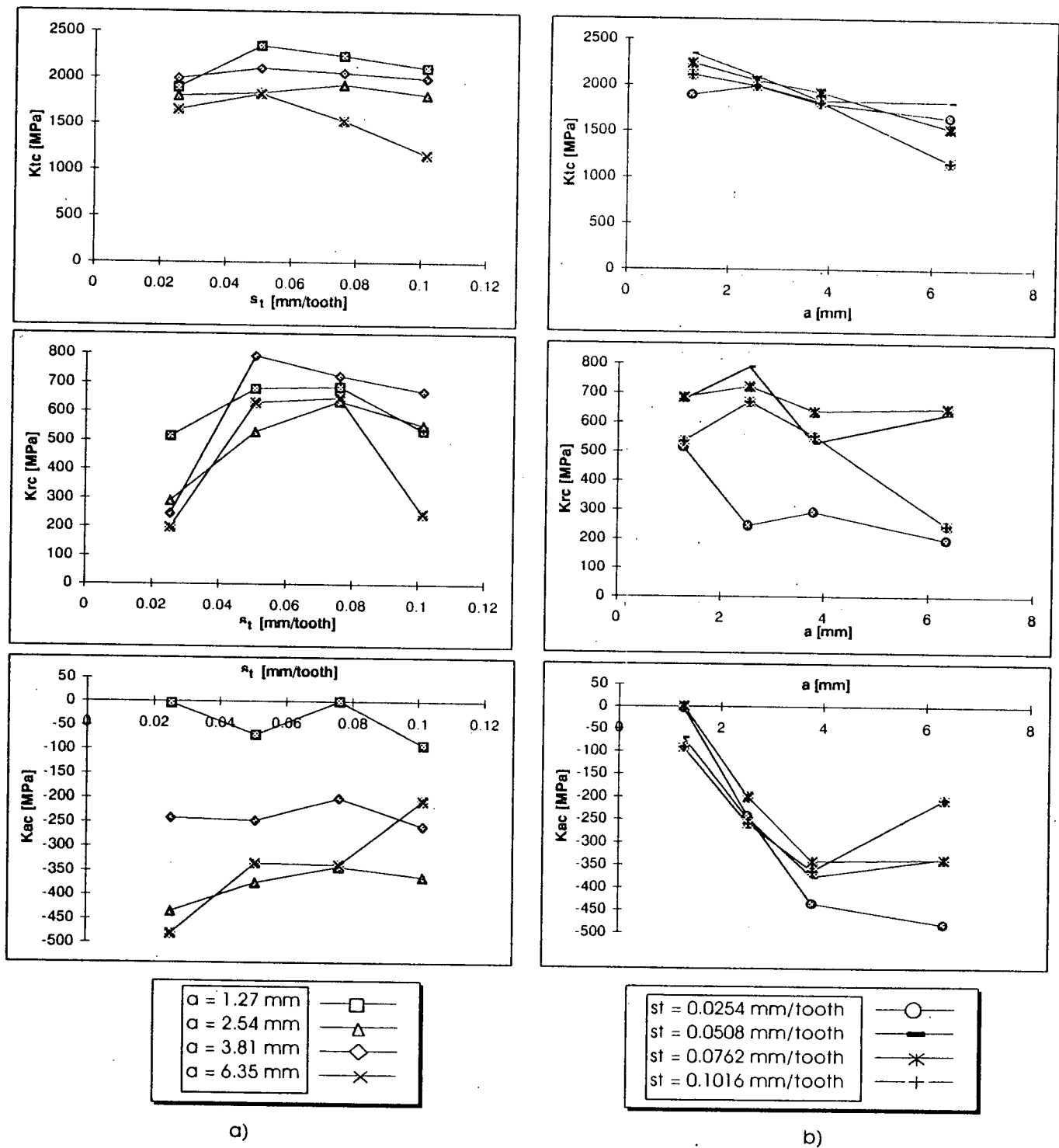


Figure 4.3: Ballend Milling Force coefficients estimated from Average Force Model: a) vs s_t , b) vs a

ballend cutters is developed and experimentally tested. The section will begin by examining some milling variables such as tooth helix angle, normal rake angle, and local chip thickness and their importances to the milling force analysis. The milling process is then examined theoretically, drawing emphasis particularly on its relationship with the fundamental theories of orthogonal and oblique cutting. It will be shown how the fundamental two dimensional orthogonal cutting model can be applied on the milling analysis and more importantly, how the required milling force coefficients can be estimated from the orthogonal machining data through oblique transformation.

Figure 4.4 shows the instantaneous geometry of a helical cutter during a milling operation with one tooth engaged in cutting at a given cutter orientation θ . The material approaches the flute at a speed approximately equal to the tangential cutting speed so that the cutting edge is inclined to the resultant cutting speed by the helix angle. Thus the cutting action may be considered equivalent to an oblique cutting process with a variable cut thickness and constant width of cut equal to a . Unlike orthogonal cutting which has a two dimensional cutting geometry, oblique cutting is a more general case of the cutting operation and is the appropriate model to represent milling with helical tool.

As in orthogonal cutting, the analysis is aimed at developing equations relating the three force components F_P, F_Q, F_R to the cutting chip geometries, b and t , the tool geometry α_n, i , the deformation geometry ϕ_n, η_c , the workmaterial property τ , and friction characteristic β at the tool/chip interface. For oblique cutting, the primary shear and friction forces lie on an orientated plane affected by the local helix angle and rake angle. Therefore, a geometric transformation has to be performed to obtain the resultant forces normal and parallel to the cutting edge.

Other important parameters required in the elemental oblique force prediction model are the inclination angle and the normal rake angle, or the velocity rake angle. As mentioned above, the inclination angle is the local helix angle on the cutter and the

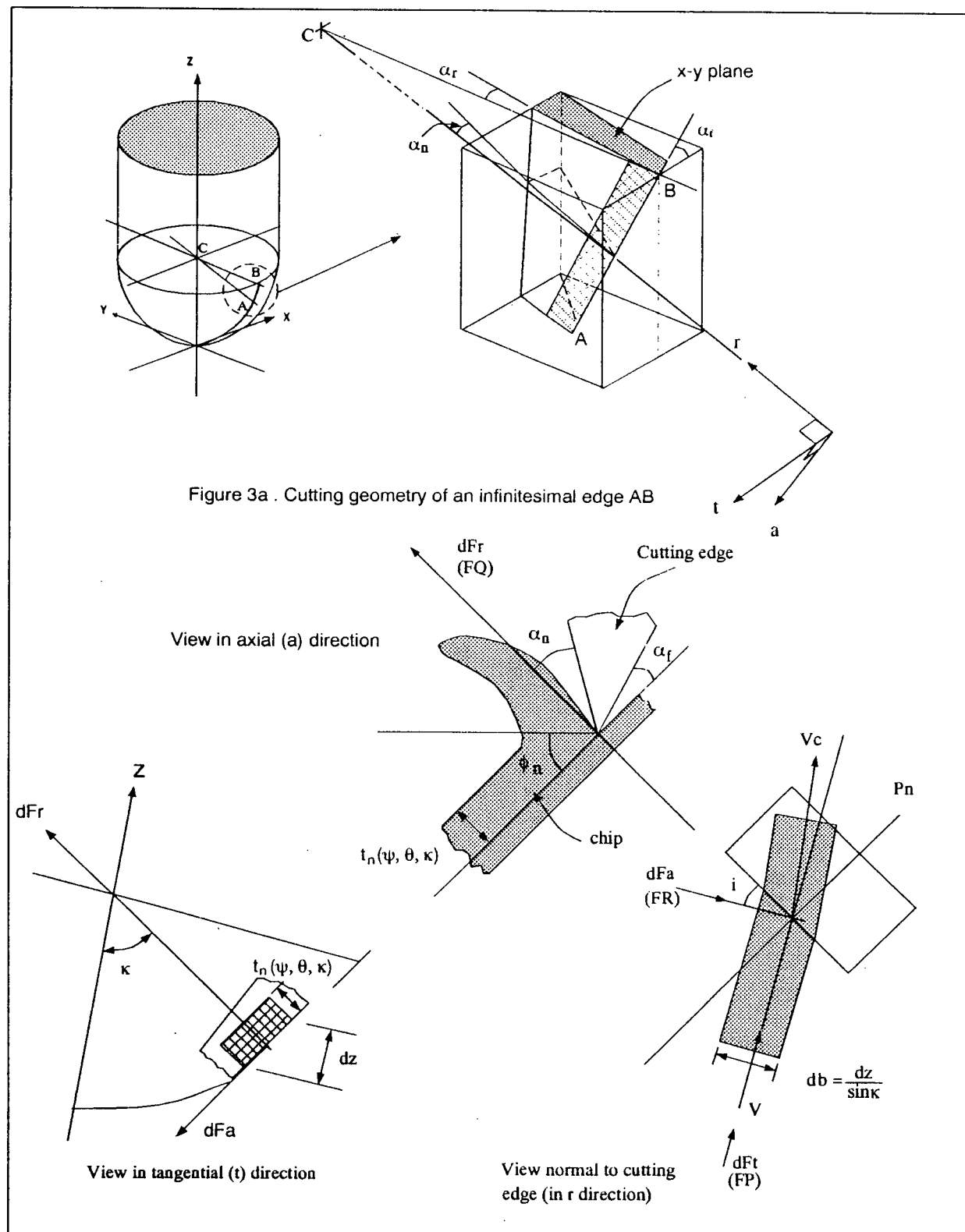


Figure 4.4: Oblique Cutting Geometry of a Ballend Mill

normal rake angle is defined in the plane perpendicular to the cutting velocity. Thus the working angles for the elemental oblique cuts can all be related to the local tool angles given in the cutter geometrical specifications.

4.2.3 Prediction of Cutting Force Coefficients from an Oblique Cutting Model

In this section, the mechanics of milling approach will be applied on ballend mills. The pressure applied on the cutter due to ploughing and cutting is related to the total forces with edge force coefficients K_{te} , K_{re} , K_{ae} , and cutting force coefficients K_{tc} , K_{rc} , K_{ac} and they will be estimated from basic machining parameters.

Ball end mill flutes are treated as combination of series of oblique cutting edge segments. An oblique cutting geometry based on the thin shear zone model is shown in Figure 4.4. The chip velocity V_c is inclined at an acute angle i to the plane P_n normal to the cutting edge. All the following equations will be written on this plane P_n which also has its orientation changes along the cutting flute due to the change in radius of the cutter.

The elemental width db of the active cutting edges on all teeth in the axial direction depends on the axial depth of cut a and the number of elements selected. Due to helix, the uncut chip thickness seen by each tooth element is different and can be approximated by Eq. (3.17).

From Figure 4.4, db is the projected length of an infinitesimal cutting flute in the direction along the cutting velocity. It should be noted that db is consistent with the chip width defined in the classical oblique cutting theory. The relationship between db and dz is given by:

$$db = \frac{dz}{\sin \kappa} \quad (4.8)$$

Applying Merchant's theory, resolving the resultant forces due to 'cutting' on the shear plane into three mutually perpendicular components yields ([19], [38]),

$$\left. \begin{aligned} F_p &= \frac{\tau b t}{\sin \phi_n} \frac{\cos(\beta_n - \alpha_n) + \tan \eta_c \sin \beta_n \tan i}{c} \\ F_q &= \frac{\tau b t}{\sin \phi_n \cos i} \frac{\sin(\beta_n - \alpha_n)}{c} \\ F_r &= \frac{\tau b t}{\sin \phi_n} \frac{\cos(\beta_n - \alpha_n) \tan i - \tan \eta_c \sin \beta_n}{c} \end{aligned} \right\} \quad (4.9)$$

where

$$c = \sqrt{\cos^2(\phi_n + \beta_n - \alpha_n) + \tan^2 \eta_c \sin^2 \beta_n}$$

F_p, F_q, F_r are the power, thrust and radial forces acting on the oblique cutting edge segment, respectively. The normal friction angle, β_n , is defined as,

$$\tan \beta_n = \tan \beta \cos \eta_c \quad (4.10)$$

where β is the average friction angle at the rake face of an orthogonal cut, and η_c is the chip flow angle (angle between a perpendicular to cutting edge and the direction of chip flow over rake face, as measured in the plane of tool face). The normal rake angle is constant, and set during cutter grinding. The normal shear angle, ϕ_n , is obtained from the cutting ratio

$$\tan \phi_n = \frac{r_t \cos \alpha_n}{1 - r_t \sin \alpha_n} \quad (4.11)$$

r_t is the chip thickness ratio in oblique cutting and is related to orthogonal parameter r by $r_t = r \frac{\cos \eta_c}{\cos i}$. This relation is obtained from the mass continuity equation of the chip before and after the cut. To further simplify the model, Stabler rule [39] is applied

in which the chip flow angle η_c is approximated by the local inclination angle i . From Figure 4.4 in which a small segment on the ball end cutter is shown, the tangential, radial and axial force components dF_t, dF_r, dF_a are compatible with the power, thrust, and radial force components F_p, F_q, F_r in oblique cutting when the elemental cut thickness t and width of cut b are given by the instantaneous chip thickness $t_{nj}(\psi, \theta, \kappa)$ and length $dz/\sin(\kappa)$ [17]. Thus the milling force component coefficients due to 'cutting', i.e. K_{tc}, K_{rc} and K_{ac} , can be expressed in terms of the transformed cutting coefficients.

$$\begin{aligned}
 K_{tc} &= \frac{\tau}{\sin \phi_n} \frac{\cos(\beta_n - \alpha_n) + \tan \eta_c \sin \beta_n \tan i}{c} \\
 K_{rc} &= \frac{\tau}{\sin \phi_n \cos i} \frac{\sin(\beta_n - \alpha_n)}{c} \\
 K_{ac} &= \frac{\tau}{\sin \phi_n} \frac{\cos(\beta_n - \alpha_n) \tan i - \tan \eta_c \sin \beta_n}{c}
 \end{aligned} \tag{4.12}$$

The edge force coefficients, which represent the rubbing force on a unit length basis, will be identified from orthogonal cutting experiments and can be directly used on the cutter edge, taking into consideration the orientation factors. Cutting pressures in tangential, radial and axial directions are calculated locally along each cutting flute segment, and elemental forces are summed along each cutting edge to evaluate the total cutting forces.

Orthogonal Cutting Parameters: A set of turning experiments resembling orthogonal cutting was conducted on Titanium tubes (*Ti6Al4V*) with tools of different rake angles over different feeds and cutting speeds (See Figure 4.5). The diameter of the tube was 100 mm (O.D.) and the thickness was $t = 3.81\text{mm}$. The cutting speed range was from 2.6 to 47 m/min. Resultant forces in the power (F_c) and thrust (F_f) directions were measured with force dynamometer. Small steps in cutting conditions were used to

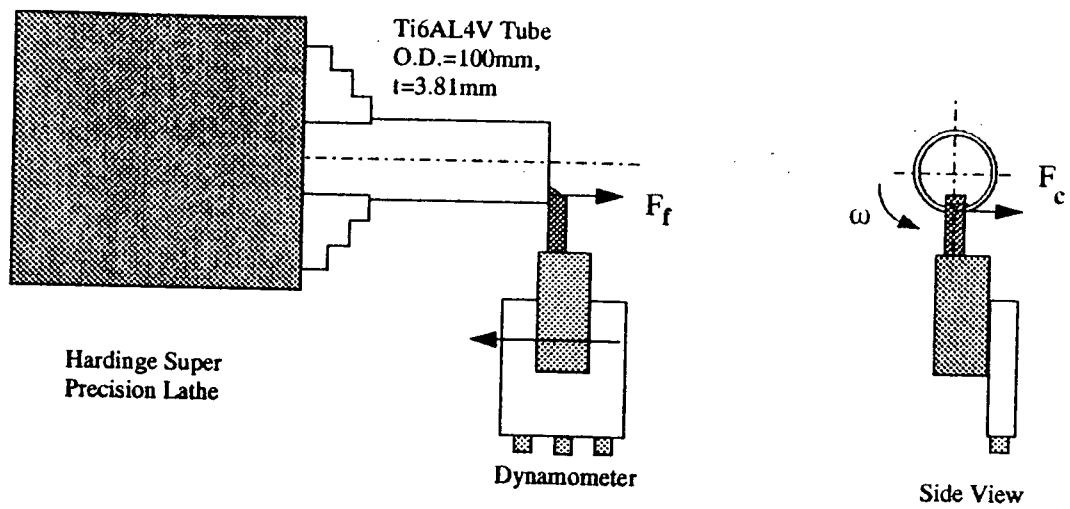


Figure 4.5: Experimental Setup - Orthogonal Turning test

increase the reliability of the measured forces. Since the measured forces may include both the forces due to shearing and a secondary process “ploughing” or “rubbing” at the cutting edge, the edge force model given in section 3.2 is applied, and the measured force components are expressed as:

$$\begin{aligned} F_{Pt} &= F_{Pe} + F_{Pc} \\ F_{Qt} &= F_{Qe} + F_{Qc} \end{aligned} \quad (4.13)$$

The edge forces are obtained by extrapolating the measured forces to zero chip thickness. From Figure 4.6, it can be seen that the edge forces do not vary significantly with cutting speeds and rake angles for the particular workpiece material (Ti6Al4V) used here. The average edge force coefficients K_{te} , K_{re} , K_{ae} represent the rubbing forces per unit chip width. The K_{ae} value is usually small and taken as zero [17].

The chip compression ratio (r), shear stress τ , shear angle ϕ , and friction angle β are calculated from the measured ‘cutting’ component of the forces and the cutting ratio by applying the orthogonal cutting theory presented by Merchant [3].

$$\left. \begin{aligned} \tau &= \frac{(F_{Pc} \cos \phi - F_{Qc} \sin \phi) \sin \phi}{bt} \\ \tan \phi &= \frac{r \cos \alpha}{1 - r \sin \alpha} \\ \tan \beta &= \frac{F_{Qc} + F_{Pc} \tan \alpha}{F_{Pc} - F_{Qc} \tan \alpha} \end{aligned} \right\} \quad (4.14)$$

The fundamental machining parameters, the shear stress (τ), average friction angle β , chip compression ratio r , are estimated by employing least square curve fitting technique to the measured orthogonal test results. Results are shown in figures 4.7, 4.8, 4.9.

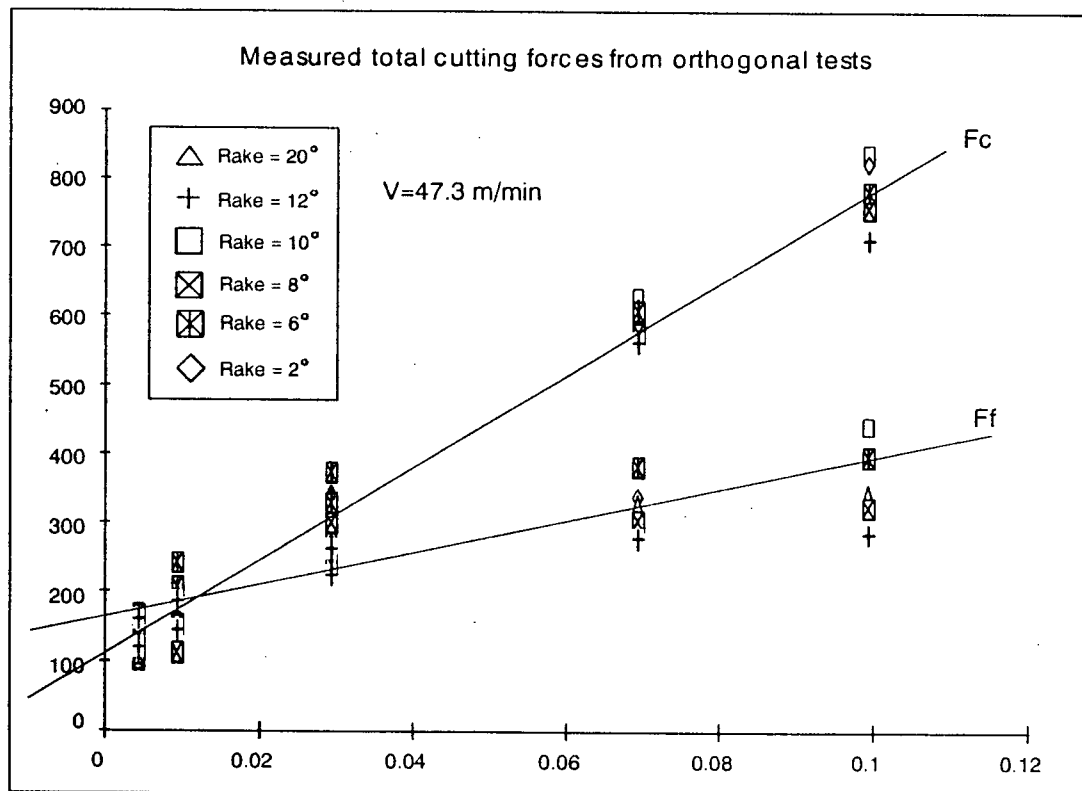
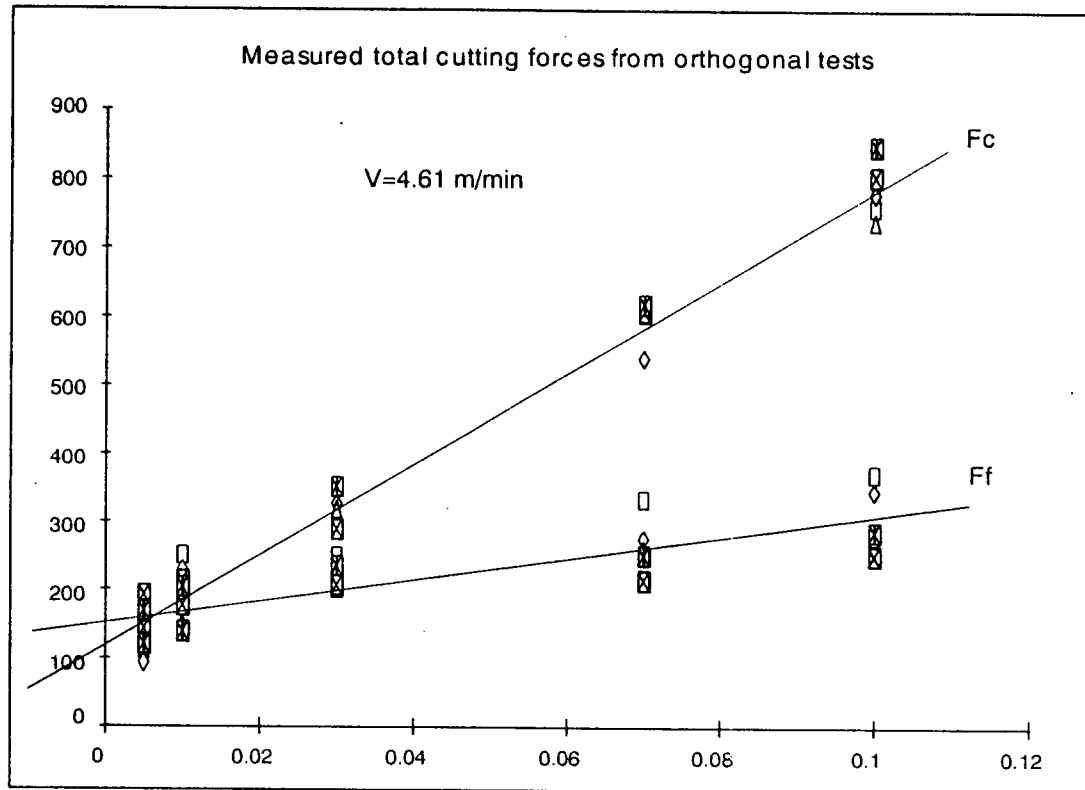


Figure 4.6: Edge Force Extrapolation from Orthogonal Turning test

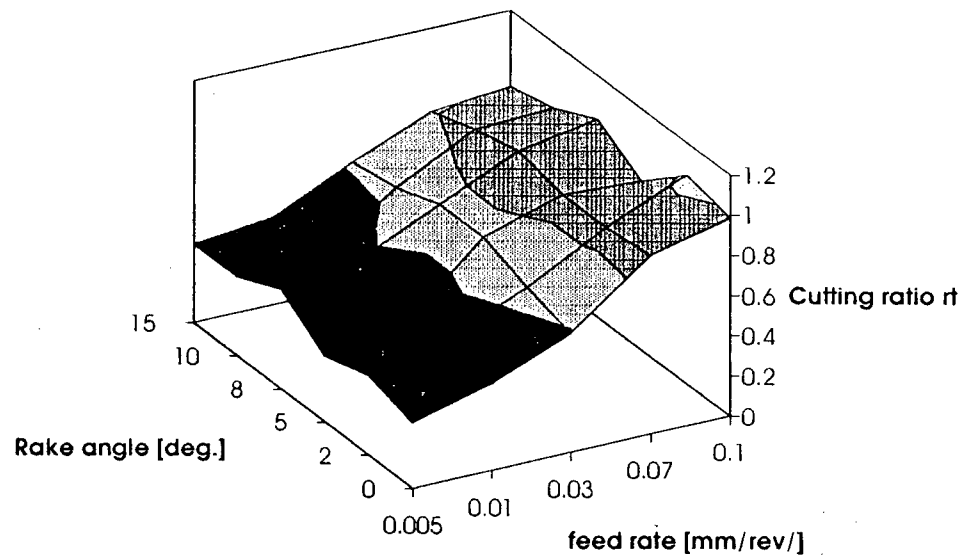


Figure 4.7: Cutting Ratio identified from Orthogonal Turning test

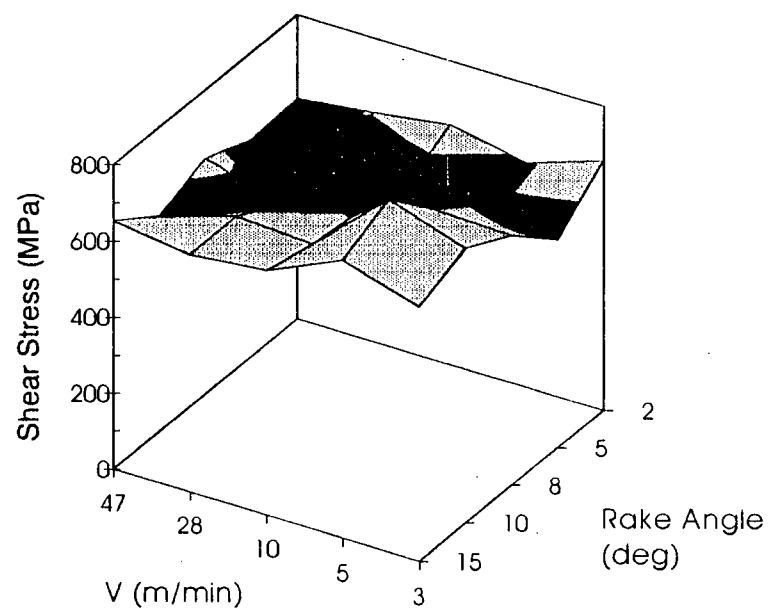


Figure 4.8: Shear Stress identified from Orthogonal Turning test

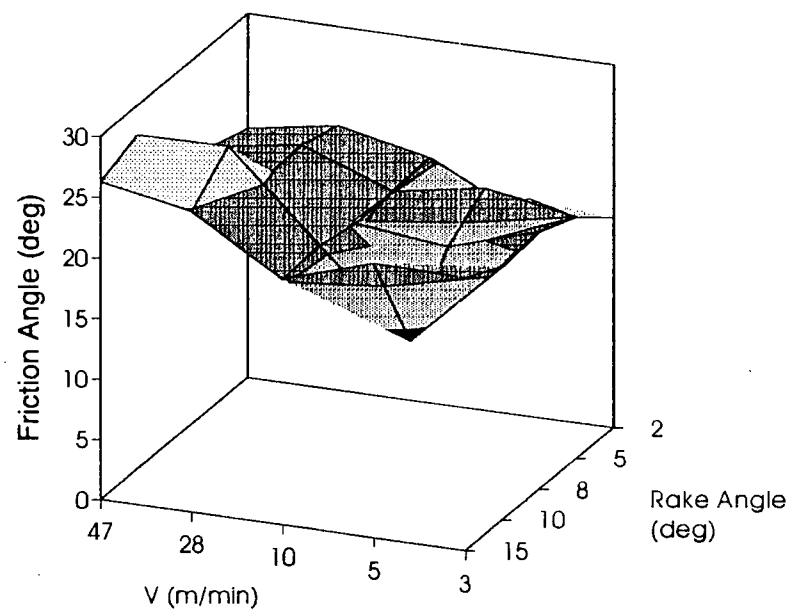


Figure 4.9: Friction angle identified from Orthogonal Turning test

The identified relationships are summarized in Table 4.1. From the results, it is observed that:

1. The shear stress does not vary significantly with either the rake angle or the cutting speed. It is higher than that found from conventional materials tests due to high shear strains, shear strain rates and temperatures involved in machining.
2. The cutting ratio, however, depends slightly on the uncut chip thickness.
3. The average friction angle on the rake face is expressed as a function of the rake angle.

These relationships are valid only for the particular workpiece material (*Ti6Al4V*) tested here, and other materials may exhibit different relationships.

Table 4.1: Orthogonal cutting data

τ	=	613 MPa
β	=	$19.1 + 0.29\alpha$
r	=	$r_o t^a$
r_o	=	$1.755 - 0.028\alpha$
a	=	$0.331 - 0.0082\alpha$
K_{te}	=	24 N/mm
K_{re}	=	43 N/mm

After the above data base is completed, milling force calculation can be made for any milling cutter geometry by using the same orthogonal data. As an example, consider the ballend mill geometry shown in Figure 3.2. Cutting velocity and helix angle vary from 0° at the ball tip to finite values at the ball/shank intersection, resulting in variable cutting conditions along each cutting flute. The in-cut portion of every cutting edge is first divided into small sections, from which each section is treated as an oblique cutting tool with a different cutting velocity and helix angle. For this reason, milling force coefficients have to be evaluated locally according to Eq. (4.12), using the un-cut

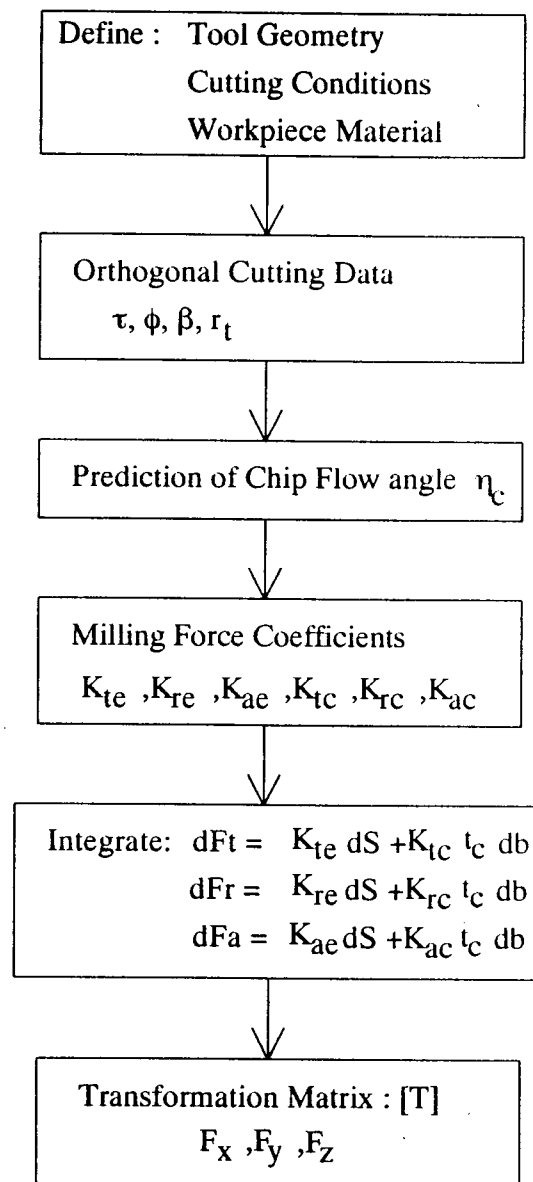


Figure 4.10: Generalized Mechanics of Cutting Approach to Milling Force Prediction

chip thickness identified from the instantaneous immersion of each section. Total milling forces at any cutter location can then be obtained by integrating all the force components dF_t , dF_r , and dF_a and transforming into the global coordinate system (X , Y and Z). The flow chart of the milling force prediction procedure based on the generalized mechanics of cutting approach can be found in Figure 4.10.

4.2.4 Simulation and Experimental Verification

The proposed cutting force models have been assessed by means of numerical simulation and experimental testing of the forces over a wide range of conditions encountered in milling. More than 60 cutting tests were conducted on a vertical SAJO CNC milling machine with 30 degrees nominal helix, single flute, carbide ball end mills.

The experimental set-up is shown in Figure 4.11. During milling tests, the cutting forces were measured with a Kistler Model 9257A three-component dynamometer and recorded by a PC equipped with a 16 channel data collection board, through charge/voltage conversion amplifiers. A microphone was also set up to measure any significant sound pressure fluctuation during machining caused by chatter vibrations. Slot cutting experiments were selected on Titanium alloy (*Ti6Al4V*) at different feeds and axial depth of cuts with cutter rake angles ranging from 0 to 15 degrees. Titanium alloy, which has high strength to weight ratio and low thermal conductivity, was selected as the workpiece material. Its application can be found mainly in the aerospace industry where high strength, high temperature resistance materials are desired on engine components. *Ti6Al4V* remains one of the most difficult material to be machined due to its high shear stress (more power in shearing the material) and low temperature gradient during cutting (thus low cutting speed).

Cutters with two different radius were used (6.35 and 9.525 mm). The tests were

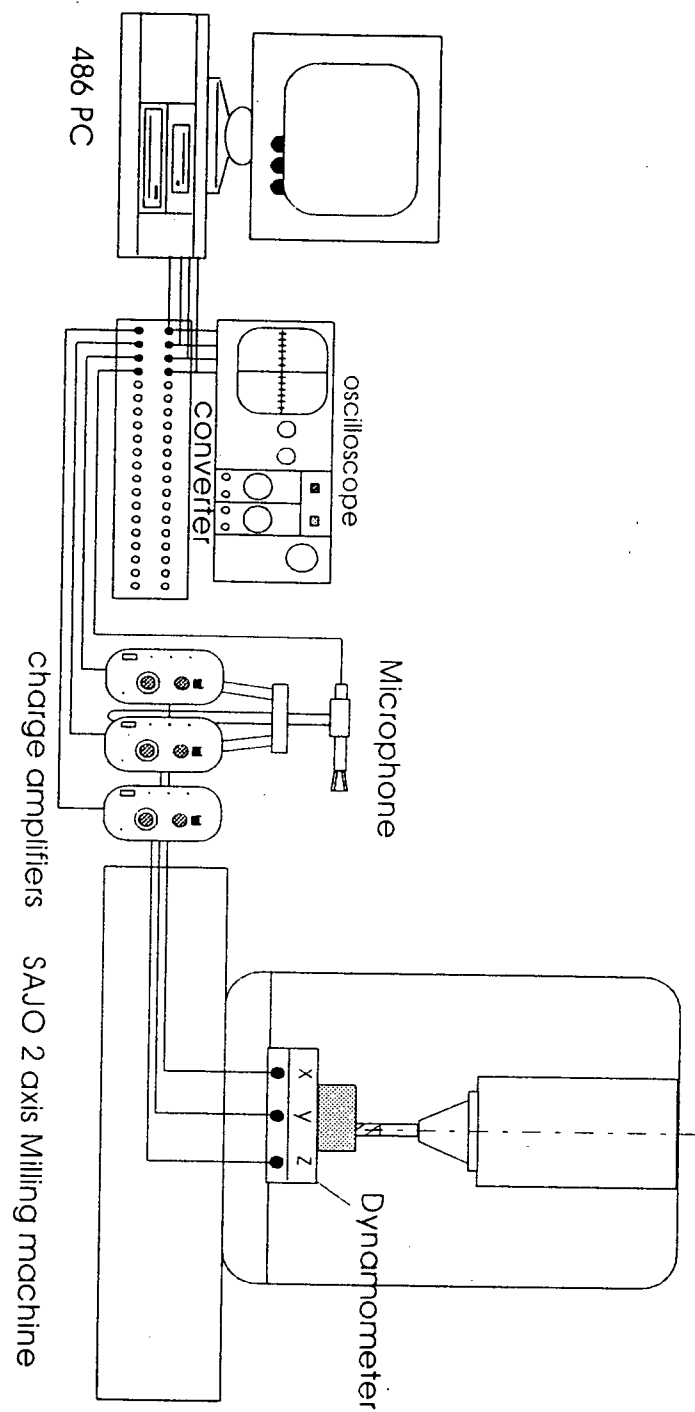


Figure 4.11: Experimental Setup for Milling Test

conducted without lubricant. Cutting conditions for the tests and simulations are summarized in Table 4.2.

Table 4.2: Cutting conditions for static ballend tests and simulations

R_0	=	6.35, 9.525 mm
α_n	=	0 - 15 degrees
i_0	=	30 degrees
N_f	=	1
s_t	=	0.0127 - 0.127 mm/tooth
a	=	1.27 - 8.89 mm
N	=	269 RPM

The solution of Eq. (4.6) is obtained by applying numerical integration technique. The cutter is first discretized axially into small discs with different radii, the lag angle of the flute j at height z in global coordinate is given by Eq. (3.12). The forces for multiple fluted cutters are obtained by summing the forces acting on the individual flutes in cut. The immersion of the cutter in the workpiece is an important factor in determining the cutting forces. In general, the contact zone between the cutter and the workpiece can be found by examining the instantaneous immersion angle of all cutting points on the cutter digitally against the entry and exit angles. At any tool rotation angle θ , it is first checked that whether the flute is in or out of cut. For example, in half immersion up milling the flute segment k is in cut if $(\psi_k)_j > 0$ and $(\psi_k)_j < \pi/2$.

Using the predictive force model with classical orthogonal cutting machining parameters, the simulation and experimental results were compared. The percentage difference between the predicted and experimental results has been used to evaluate the statistical reliability of the model.

Figure 4.12 shows the histograms of the percentage errors and the mean values of the average forces. It can be seen that the model provides, both qualitatively and quantitatively, sound predictions of the cutting forces in all three components, with mean deviation of -0.93 % for average F_x , 1.36 % for average F_y , and 3.03 % for average F_z . The corresponding ranges in percentage deviation are -30 % to 25 % for average F_x , -25 % to 15 % for average F_y , and -35 % to 40 % for average F_z . In Figure 4.13, a sample simulation of cutting forces for a slotting test with axial depth of cuts $a = 1.27mm$ and $6.35mm$ at feed-rate $f_d = 0.0508mm/tooth$ are shown for a single fluted cutter with zero rake angle. The cutting force pattern in the axial direction is dominated by the ploughing action between the flute and the material. As soon as the flutes enter into cut, the flank forces develop rapidly while the chip thickness is still small. In Figure 4.14, predicted and measured cutting forces for a slotting test with different sizes of cutters are shown. The predicted and simulated cutting forces are in good agreement. In a separate case, half immersion up-milling tests with axial depth of cut $a = 6.35mm$ but with two different feed-rates of $f_d = 0.0508mm/rev$ and $f_d = 0.1016mm/rev$ were conducted. Again, the predicted and measured cutting forces, as seen in Figure 4.15, are in good agreement except with slight phase shifts at the exit due to difficulty in selecting the reference point in the half immersion test data.

To further validate the developed geometric and cutting force models, simulations and experiments were performed on multi-fluted ballend cutters. A three fluted ballend mill with a zero rake angle and angular grinding tolerance of $(+2^\circ, -2^\circ)$ was used in the tests. For the experiments conducted, the tool holder and spindle were both very stiff, making the runout level quite small, (the maximum radial runouts measured at the ball-shank meeting region of the flutes were 0.015mm, 0.01mm and 0.0mm), therefore the effect of

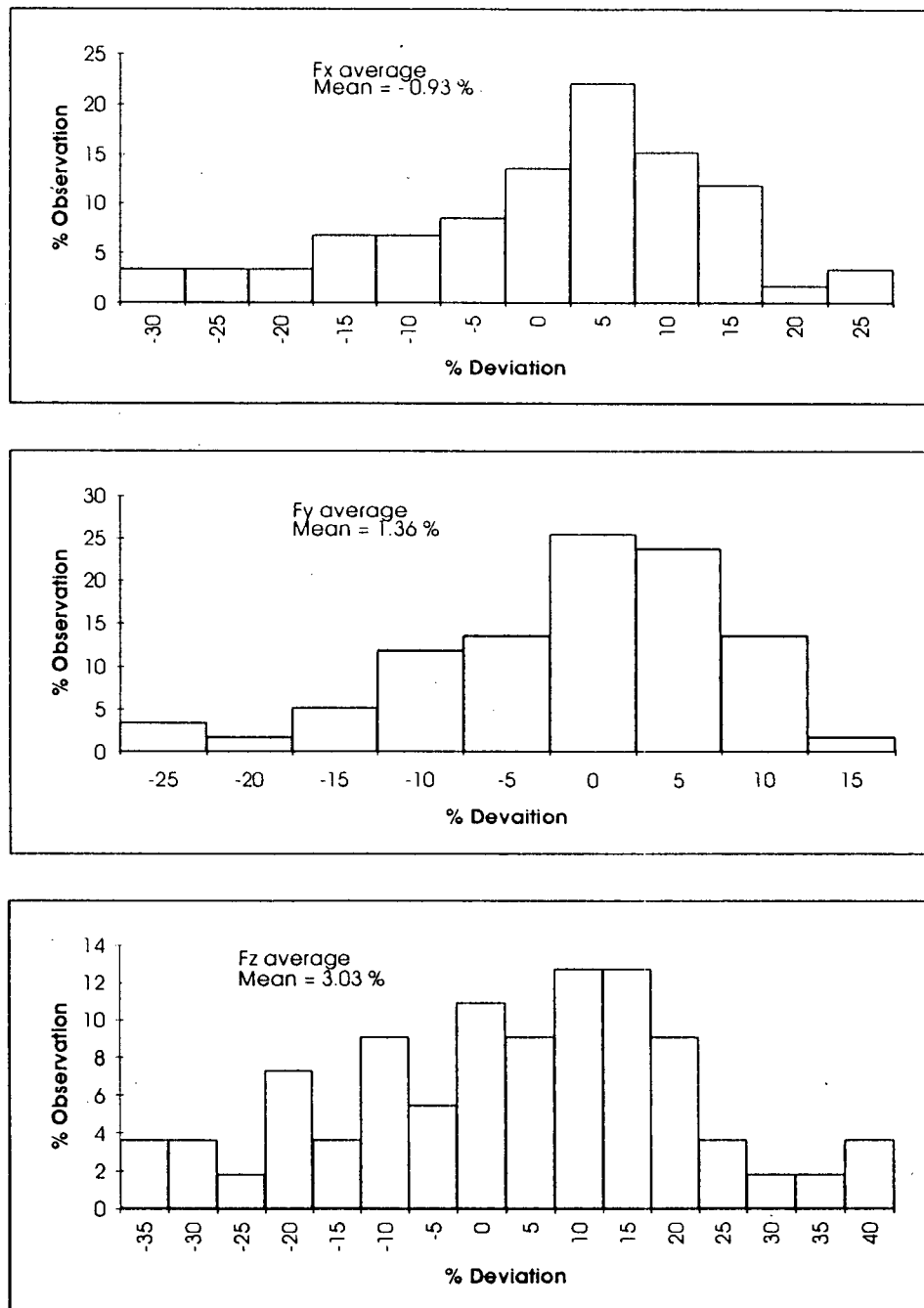


Figure 4.12: Statistical Evaluation of Model and Data

runout on the resultant cutting forces, as seen in Figure 4.16, was minimum.

4.3 Conclusions

A generalized cutting force model was developed for common milling operations in this chapter. The cutting forces were modelled by separating the shearing and edge friction components on the edge. Milling force coefficients were obtained from an orthogonal machining data base using oblique transformation, which eliminates the need of calibrating for each cutter geometry. The data base was applied on milling with ballend cutters in which the model was experimentally verified, both qualitatively and quantitatively. The results should help the process planners in designing tools and in selecting optimum cutting conditions prior to each operation to increase the productivity.

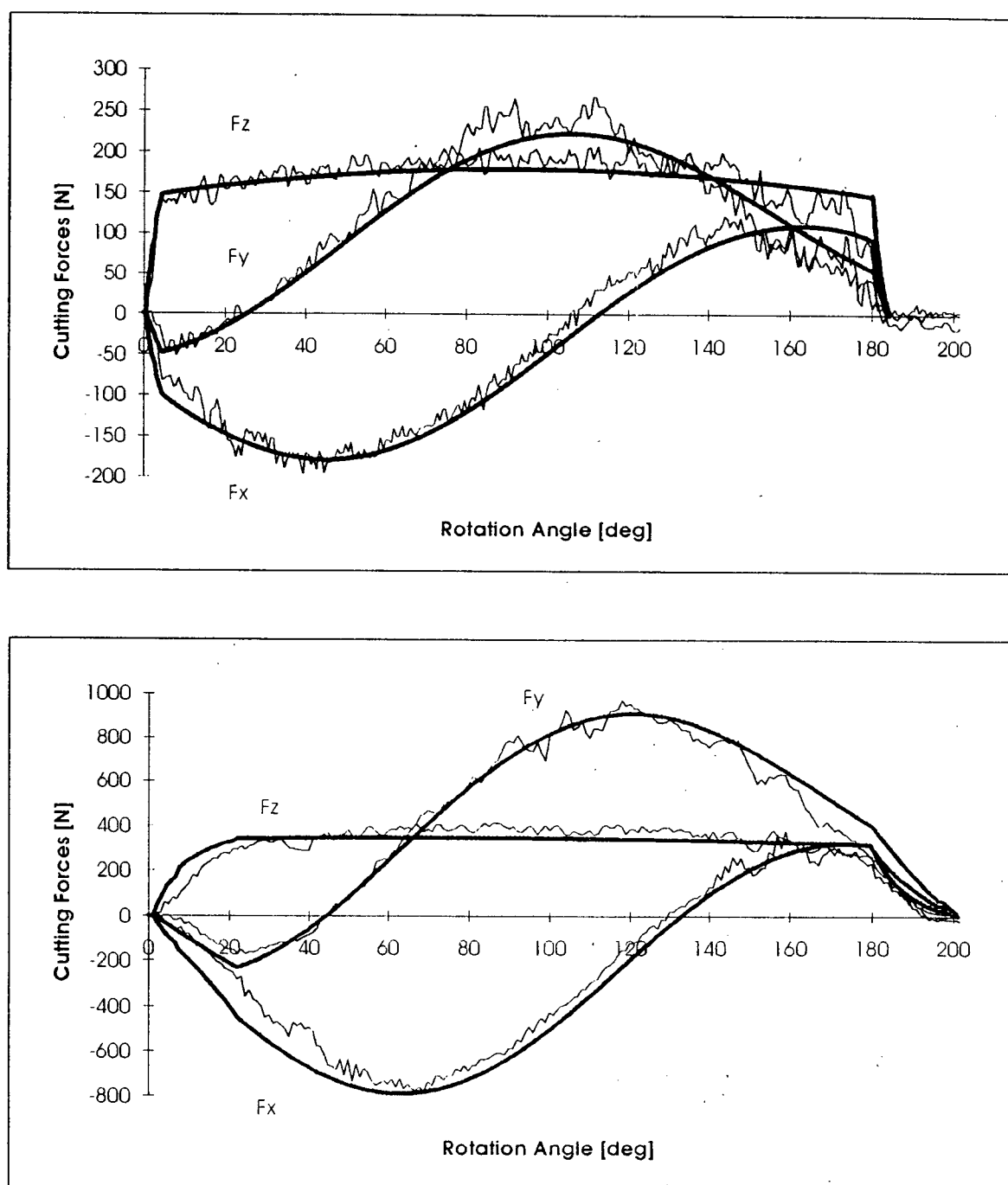


Figure 4.13: Measured and predicted cutting forces for slot cutting tests, ballend mill, spindle speed 269 rev/min , $R_0 = 9.525 \text{ mm}$, $i_0 = 30^\circ$, $s_t = 0.0508 [\text{mm}/\text{flute}]$ (a)- $a = 1.27$ [mm] (b)- $a = 6.35$ [mm], rake=0

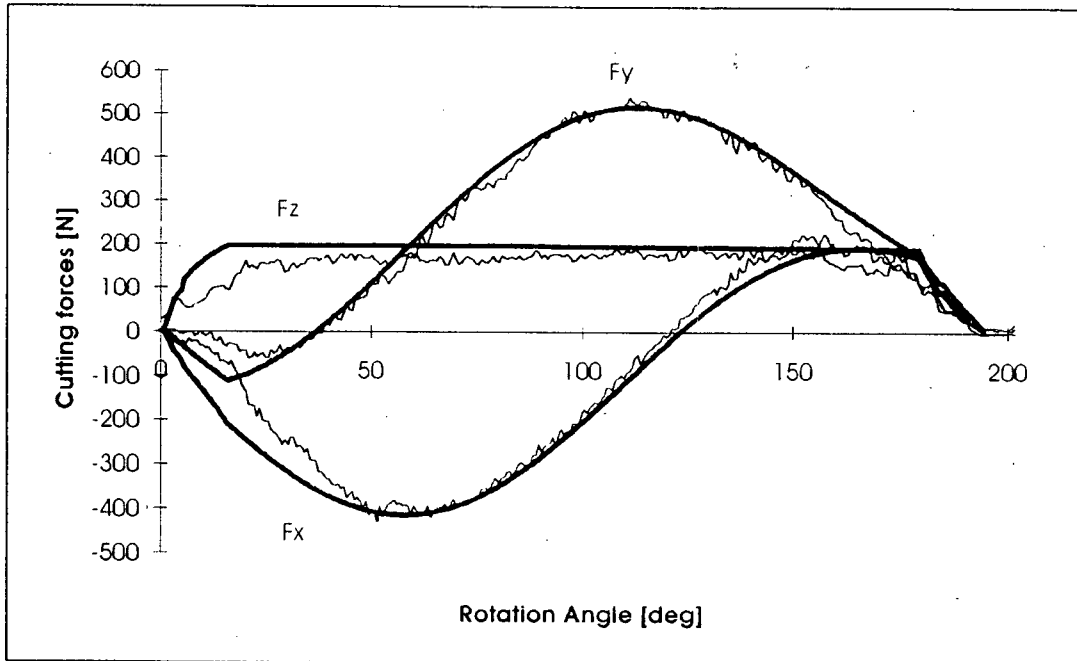
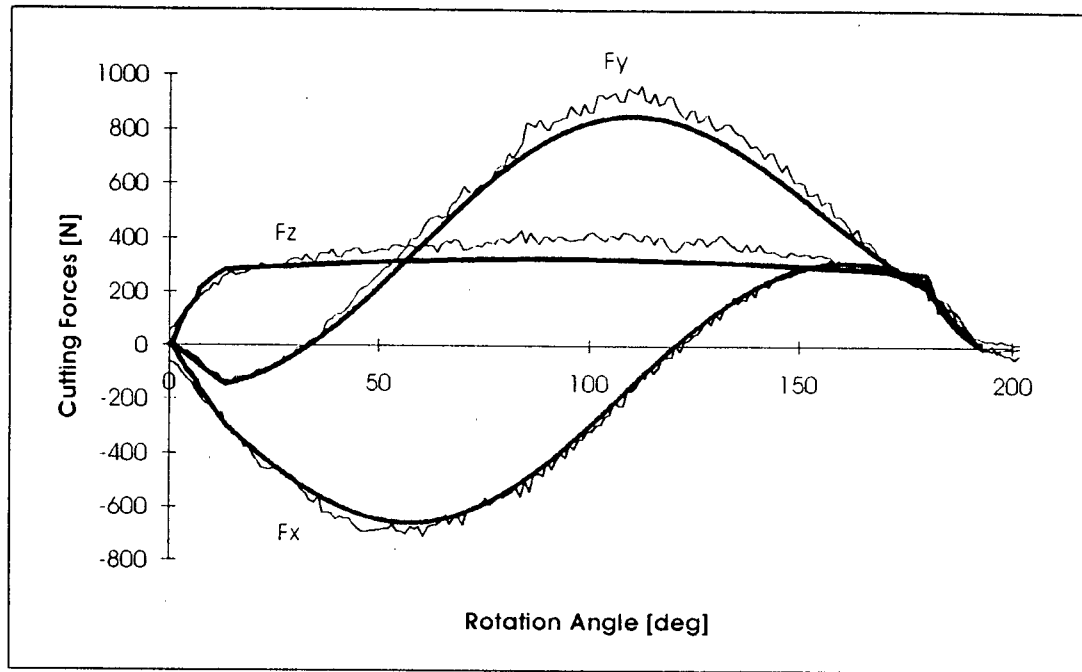


Figure 4.14: Measured and predicted cutting forces for slot cutting tests, ball-end mill, spindle speed 269rev/min, $i_0 = 30^\circ$. (a) $a=3.81$ [mm], $R_0=9.525$ mm, $s_t=0.1016$ [mm/flute], rake=5 (b) $a=3.048$ [mm], $R_0=6.35$ mm, $s_t=0.0762$ [mm/flute], rake=10

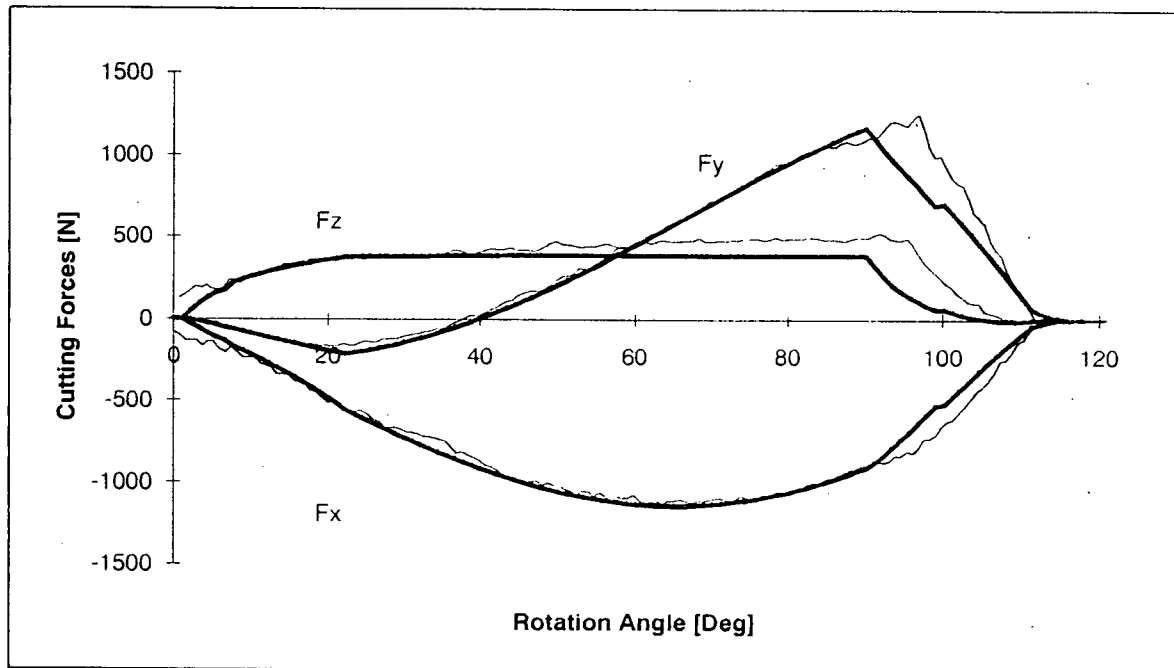
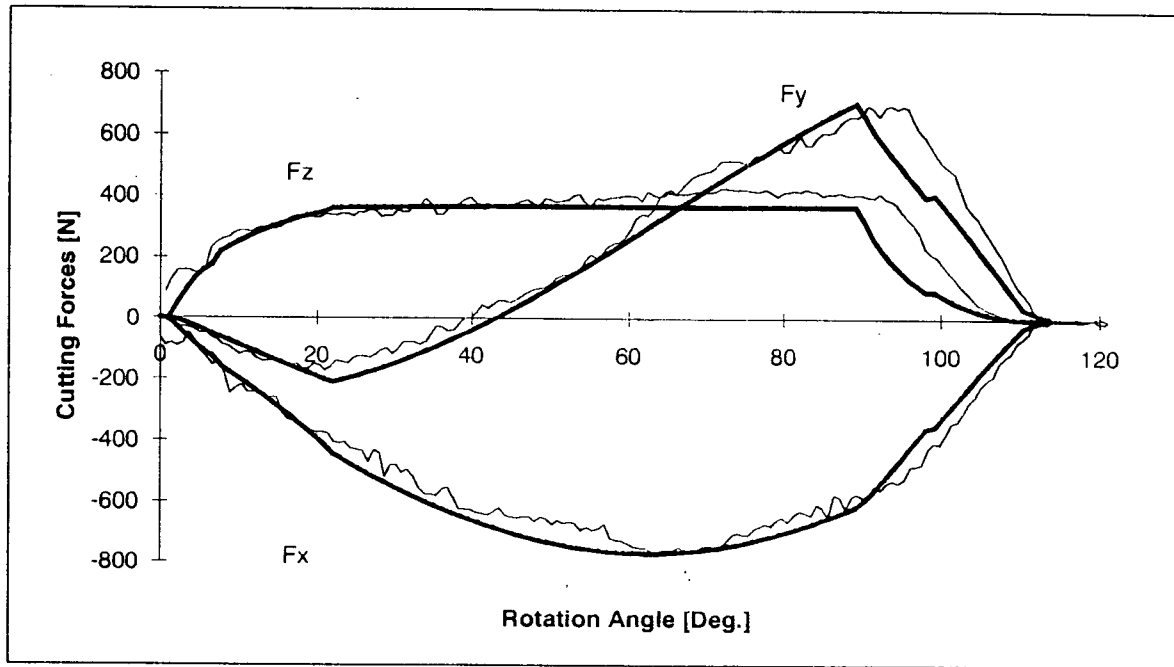
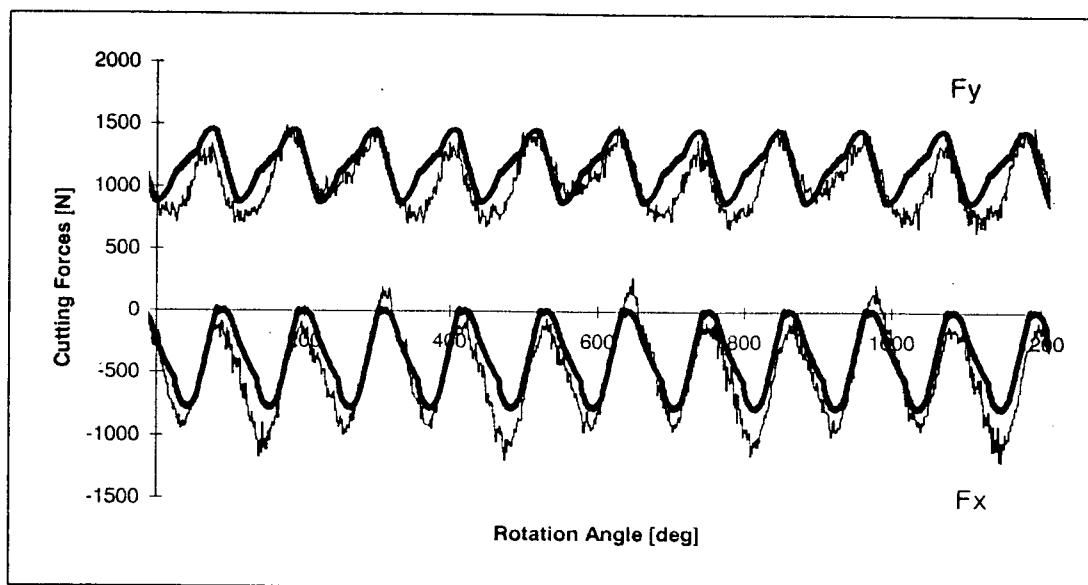
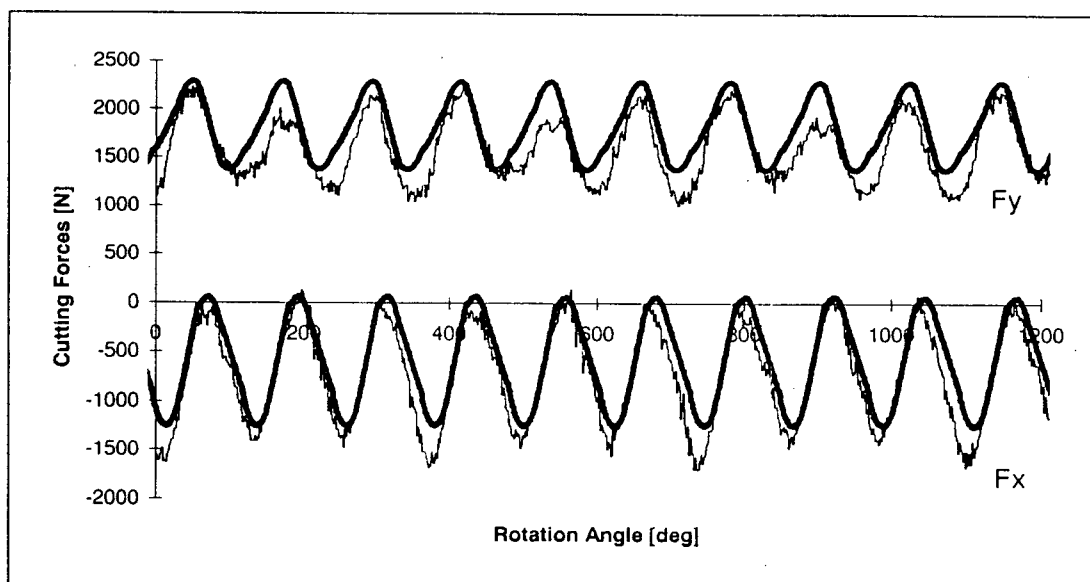


Figure 4.15: Measured and predicted cutting forces for half radial immersion cutting tests, ballend mill, $\alpha_n = 0^\circ$, $a = 6.35$ mm, spindle speed 269 rev/min , $i_0 = 30^\circ$, (a) $s_t = 0.0508$ [mm/flute], (b)- $s_t = 0.102$ [mm/flute]



a)



b)

Figure 4.16: Measured and predicted cutting forces for slot milling with a 3 fluted ball-end mill, $a = 8.9\text{mm}$, $i_0 = 30^\circ$, (a) spindle speed 480rev/min , $\alpha_n = 15^\circ$, $s_t = 0.0889$ [mm/flute], (b) spindle speed 615rev/min , $\alpha_n = 0^\circ$, $s_t = 0.127$ [mm/flute]

Chapter 5

Dynamic Milling and Chatter Stability

5.1 Introduction

A vibration system can be represented, in the most simplest case, in terms of a single degree of freedom system with a mass m on a restoring spring of stiffness k and a dashpot with damping c , as shown in Figure 5.1. The equation of motion can be obtained using Newton's second law:

$$m\ddot{q}(t) + c\dot{q}(t) + kq(t) = F_q(t) \quad (5.1)$$

This form of equation is useful in cases such as free vibration, ($F_q(t) = 0$) and forced vibration, when the forcing functions come from external sources or from the cutting process. However, there are systems for which the exciting force is a function of the motion parameters of the system, such as displacement, or velocity. Such systems, as occurred in dynamic milling, are called self-excited vibrations or chatter since the motion itself produces the exciting force.

Although very few practical structures could realistically be modelled by a single degree of freedom system, the properties of such a system are very important since those for a more complex but linear multidegree of freedom system can always be represented as the linear superposition of a number of single degree of freedom systems.

The solutions to the above equation of motion usually come in two different forms. The time domain solution which is well explored in the literature gives the response in

discrete time domain while the frequency transfer function considers the solution in terms of magnitude and phase of the system transfer function in frequency domain. These two solution forms will be briefly reviewed in the following:

Consider a SDOF system as shown in Figure 5.1, the equation of motion is:

$$m_x \ddot{x}(t) + c_x \dot{x}(t) + k_x x(t) = F_x(t) \quad (5.2)$$

The above equation can be evaluated at each discrete time interval δt with numerical techniques such as recursive, discrete equivalent of the continuous differential equation. Taking Laplace transform of Eq. (5.2) gives:

$$ms^2 x(s) + csx(s) + kx(s) = F_x(s) \quad (5.3)$$

or

$$x(s) = \frac{F_x(s)}{ms^2 + cs + k} \quad (5.4)$$

where s is the Laplace operator. The discrete time equivalent of the Laplacian operator can be approximated using the bilinear transformation (trapezoidal integration) method [40] by letting,

$$s = \frac{2(1 - z^{-1})}{T(1 + z^{-1})} \quad (5.5)$$

where z is the Z-transform operator and (T) is the time step. Substituting Eq. (5.5) into Eq. (5.3) and after simplification gives the response x in discrete time,

$$x(t) = \frac{F_x(t) + 2F_x(t-T) + F_x(t-2T) - C_1 x(t-T) - C_2 x(t-2T)}{C_3} \quad (5.6)$$

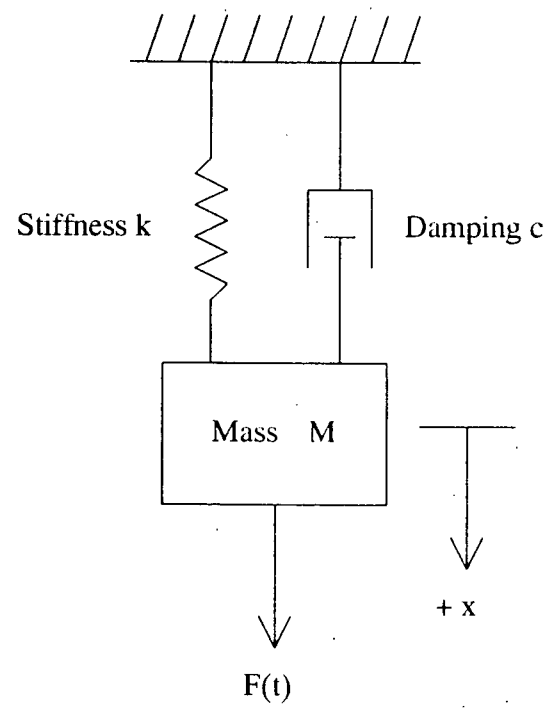


Figure 5.1: Schematic Representation of a SDOF System

where

$$\begin{aligned} C_1 &= -\frac{8}{T^2}m_x + 2K_x \\ C_2 &= \frac{4}{T^2}m_x - \frac{2}{T}c_x + k_x \\ C_3 &= \frac{4}{T^2}m_x + \frac{2}{T}c_x + k_x \end{aligned} \quad (5.7)$$

This numerical solution procedure is a rapid and robust integration scheme which is numerically stable for reasonably small time step T , making it ideal to be used on digital computers. The structural parameters in the equations above are usually identified by experimental modal analysis. Modal analysis is defined as the process which is “involved in testing components or structures with the objective of obtaining a mathematical description of their dynamic or vibration behavior [41].” Common methods include exciting the structure with a known source (e.g. impact hammer or shaker) and measuring its responses (e.g. displacement, velocity, or acceleration) at different locations. The transfer function is then obtained in the form known as frequency response function which is computed from the Fourier transforms of the excitation and the response time histories. The mathematical representation for a frequency domain transfer function is found by substituting ($s = j\omega$) into Eq. (5.4):

$$G(\omega) = \frac{X(\omega)}{F(\omega)} = \frac{1}{(k - m\omega^2) + jc\omega} \quad (5.8)$$

which can be represented graphically in terms of i) modulus and phase angle against frequency, ii) real and imaginary components of response with varying frequency, or iii) vector diagram of the real component versus the imaginary component of the response.

For a SDOF mechanical structures with light damping, a sample transfer function is shown in Figure 5.2. As described by Eq. (5.3), it gives a complete physical description of the dynamic characteristics such as the natural frequency, damping ratio, and the stiffness of the system based on some well-established mathematical relationships:

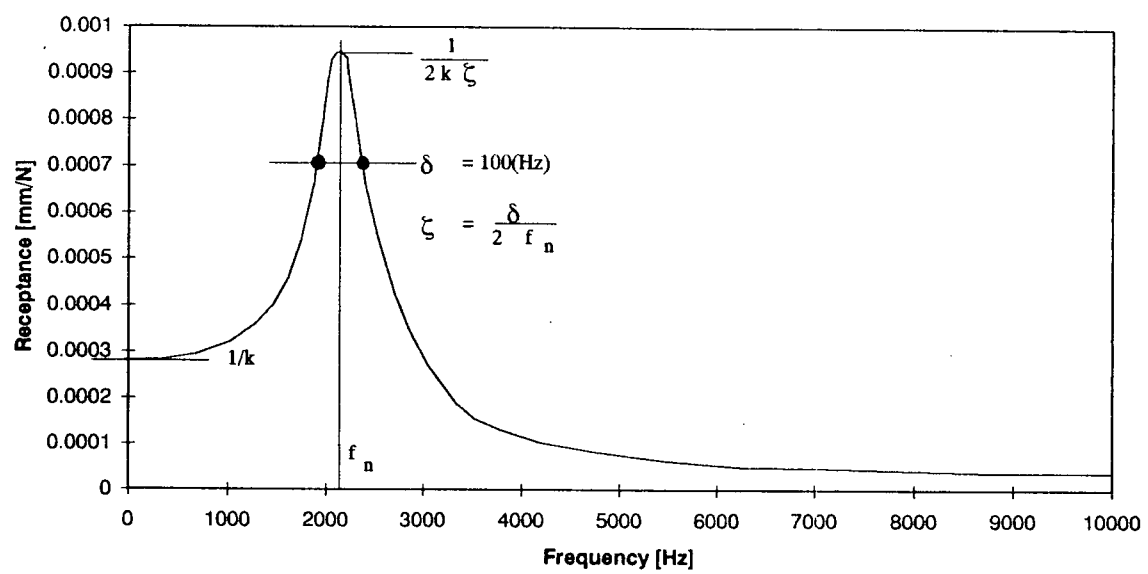


Figure 5.2: Frequency Domain characteristic curve for a SDOF Dynamic System

$$\omega_n = \sqrt{k/m} \quad \xi = \frac{c}{2\sqrt{km}} \quad \omega_d = \omega_n \sqrt{1 - \xi^2} \quad (5.9)$$

The system parameters can be used to predict the response to various excitations or to improve the dynamic behavior of the system by design modifications. In the modal analysis performed in this study, the structure is assumed to be linear and the parameters to be time-invariant.

This chapter presents a comprehensive simulation model for dynamic milling in which the milling cutter attached to the spindle is modelled by two orthogonal structural modes in the feed and normal directions at the tool tip. For a given cutter geometry, the cutting coefficients are transformed from an orthogonal cutting data base using an oblique cutting transformation model as presented in the previous chapter. The surface finish is digitized using the true trochoidal kinematics of milling process at each tooth period. The dynamically regenerated chip thickness, which consists of rigid body motion of the tooth and structural displacements, is evaluated at discrete time intervals by comparing the present and previous tooth marks left on the finish surface. The process is simulated by considering the instantaneous regenerative chip load, local cutting force coefficients, structural transfer functions and the geometry of milling process. The proposed model is capable of providing information about the severity of any resulting vibration, the magnitude of the cutting forces, and the surface finish by combining the kinematics of both chatter free static and dynamic cutting with chatter vibrations in a unified mathematical model.

5.2 Modelling of Dynamic Milling

The simulation model presented in this section is similar to the earlier dynamic face milling work presented by Montgomery and Altintas [1] with modifications being made

for ballend milling analysis. The combination of the translating motion of the workpiece and the rotatory motion of the cutter results in a non-circular tooth path, or described as trochoidal. In previous investigations of the milling process [2, 12], it has been customary, for the sake of simplicity, to assume that the path generated by the cutter tooth is circular, which results in simple chip thickness expression. However, as shown in chapter 3, the error introduced by the approximation becomes significant when the feed is high, or for cutters with small radii, such as ballend mills which have variable radii. As the axial depth of cut and feed per tooth are usually very small in ball end milling operations, especially when machining hard die and tool steels, the circular tooth path assumption may be insufficient to be applied in the analysis. Therefore, the true kinematics of milling presented by Martellotti [2, 42] are used to obtain accurate cutting force predictions.

It should be noted that, although emphasis has been placed mainly on ballend milling, the model presented in this chapter is general enough to be used in the prediction of dynamic milling process for other cutter geometries outlined in chapter 3 and other cutting conditions.

5.2.1 Dynamic Milling Implementation

In order to model the dynamic motion of the cutting edges in discrete time domain, the process is digitized and simulated at $\Delta t[s]$ time intervals. Both the cutter and the workpiece kinematics are modelled as follows:

Geometry of Tool Motion: The geometry of dynamic milling with ballend mill is shown in Figure 5.3. The cutter is digitized into k_z slices axially with a step size of δz . The center of the coordinate system is selected as the stationary spindle axis at $(0, 0, 0)$, coincides with the tip of the cutter initially. The cutter rotates with a speed ω clockwise. Each point on the flute j at height z is referenced by its immersion angle Ψ in global coordinate. During dynamic milling, the center of the cutter shifts by an amount

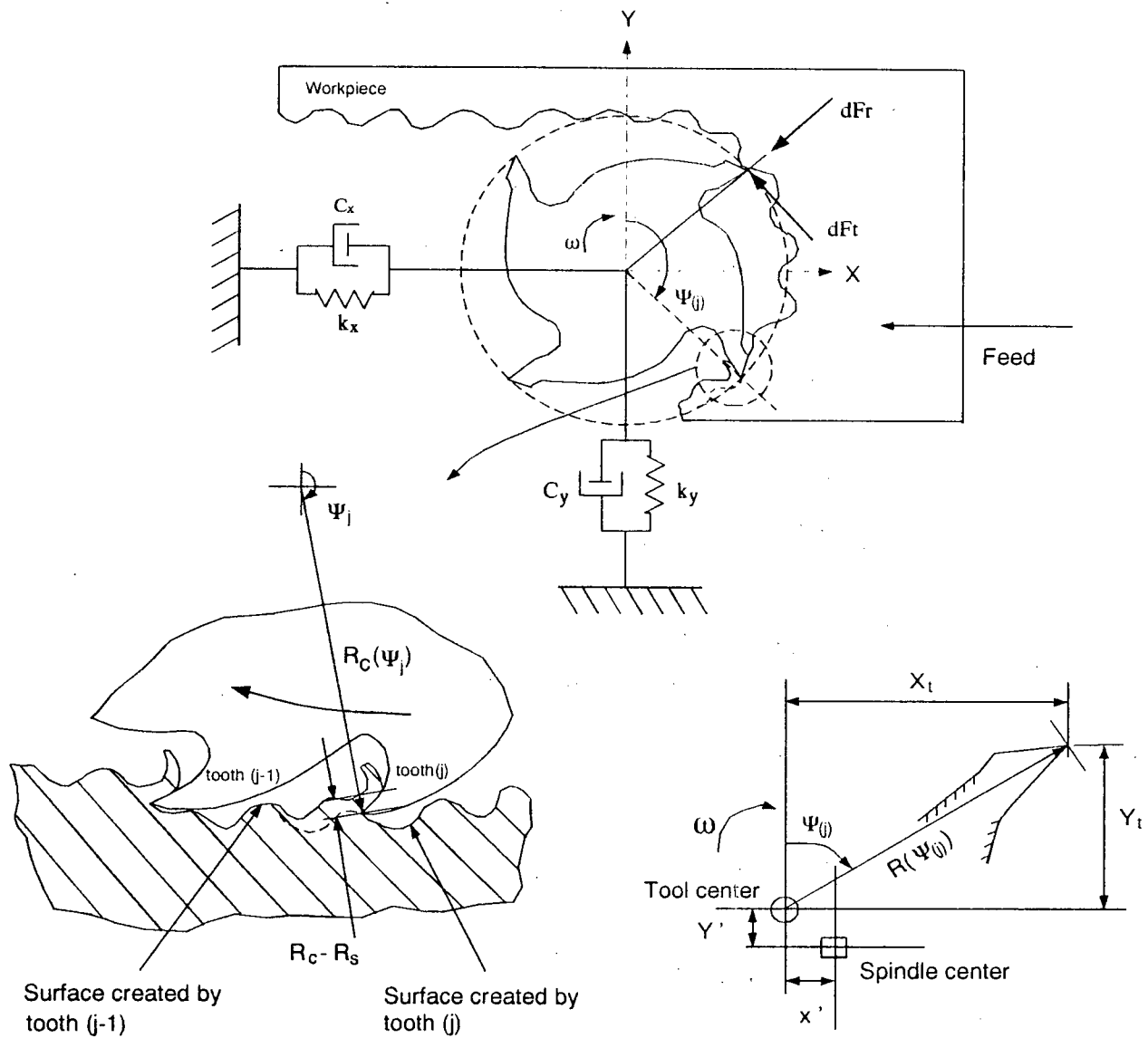


Figure 5.3: Evaluation of chip thickness from the dynamically generated surfaces at present and previous tooth periods

determined by the structural vibrations in the feed and normal directions:

$$x_c(t) = x'(t) \quad \& \quad y_c(t) = y'(t) \quad (5.10)$$

where $[x'(t), y'(t)]$ are the displacements of the cutter center relative to the stationary spindle axis due to structural vibrations at time t .

Therefore, at any time t , the coordinates of a cutting edge point are calculated for each axial depth of cut k_z as,

$$\left. \begin{aligned} x(k_z, t) &= R(\psi)\sin(\Psi) + x'(t) \\ y(k_z, t) &= R(\psi)\cos(\Psi) + y'(t) \\ z(k_z, t) &= k_z \Delta z \end{aligned} \right\} \quad (5.11)$$

The radial distance between the center of the spindle and the cutting edge point is,

$$R_c(k_z, t) = \sqrt{x(k_z, t)^2 + y(k_z, t)^2}. \quad (5.12)$$

The corresponding discrete angular rotation interval becomes $\Delta\theta = \omega\Delta t$. In the beginning of the simulation, the cutter is assumed to reach its steady state immersion (Θ_s) without any vibrations, therefore the static and dynamic displacements are not considered and a smooth surface is generated by the rigid body motion of the milling system.

One factor which influences the accuracy of the model is cutter runout, first studied in detail by Kline and Devor [10]. The effect of cutter runout is often induced by the tightening action of a set screw which causes the cutter to offset the tool holder. Other sources of runout include spindle runout, and cutter errors result from grinding. As a result, the teeth on the offset side of the holder have a larger effective radius than those on the other side. The presence of runout increases the average chip thickness (or uneven chip load distribution) which leads to higher force fluctuations, hence greater surface

error. The general modelling technique is to replace the radius of each tooth, which can be a function of the axial depth of cut, by an effective radius. Although the effect of the runout will not be investigated in this study to simplify the analysis, it can be easily included in the proposed cutter model.

Another possible modification to the cutter model is to include the effect of gash generation for some complex cutters. In the case of multiple fluted ballend mills, one of the flute is always grounded up to the ball tip while the rest of the flutes are grounded both radially and axially away from the tip to eliminate the finished surface marks. Again, this effect will be ignored in the following study for simplicity, although it can be considered in the general model.

Geometry of Workpiece Motion: The workpiece surface is digitized by a number of points and stored in Cartesian coordinates format in an array, see Figure 5.4. The center of the coordinate system is the same as the cutters' and it is initialized to the workpiece geometry. The digitized surface is represented by M points at each axial layer, each having the coordinates $SURF(P(m), z_k)$, where point $P(m) = \{x(m), y(m)\}$ is located at axial depth $z_k = k_z \Delta z$. For example, the in plane coordinates of the digitized surface point at an axial depth of cut $z = k_z \Delta z$ is stored in computer as :

$$\left. \begin{aligned} x_s(m) &= SURF(m, z_k, x) \\ y_s(m) &= SURF(m, z_k, y) \end{aligned} \right\} \quad (5.13)$$

The surface at axial layer z_k is represented by points $m = 0, 1, 2, \dots, M$, and their coordinates are updated at each time interval Δt as a result of the feed motion. Unlike in the cutter model where structural vibrations are superimposed onto the tool motion, the workpiece used in milling, in particular die machining with ballend mills, usually has shallow depth, tight clamping and is more rigid than the machine tool/cutter assembly. Therefore, although vibrations can be included in the workpiece model, for the sake of

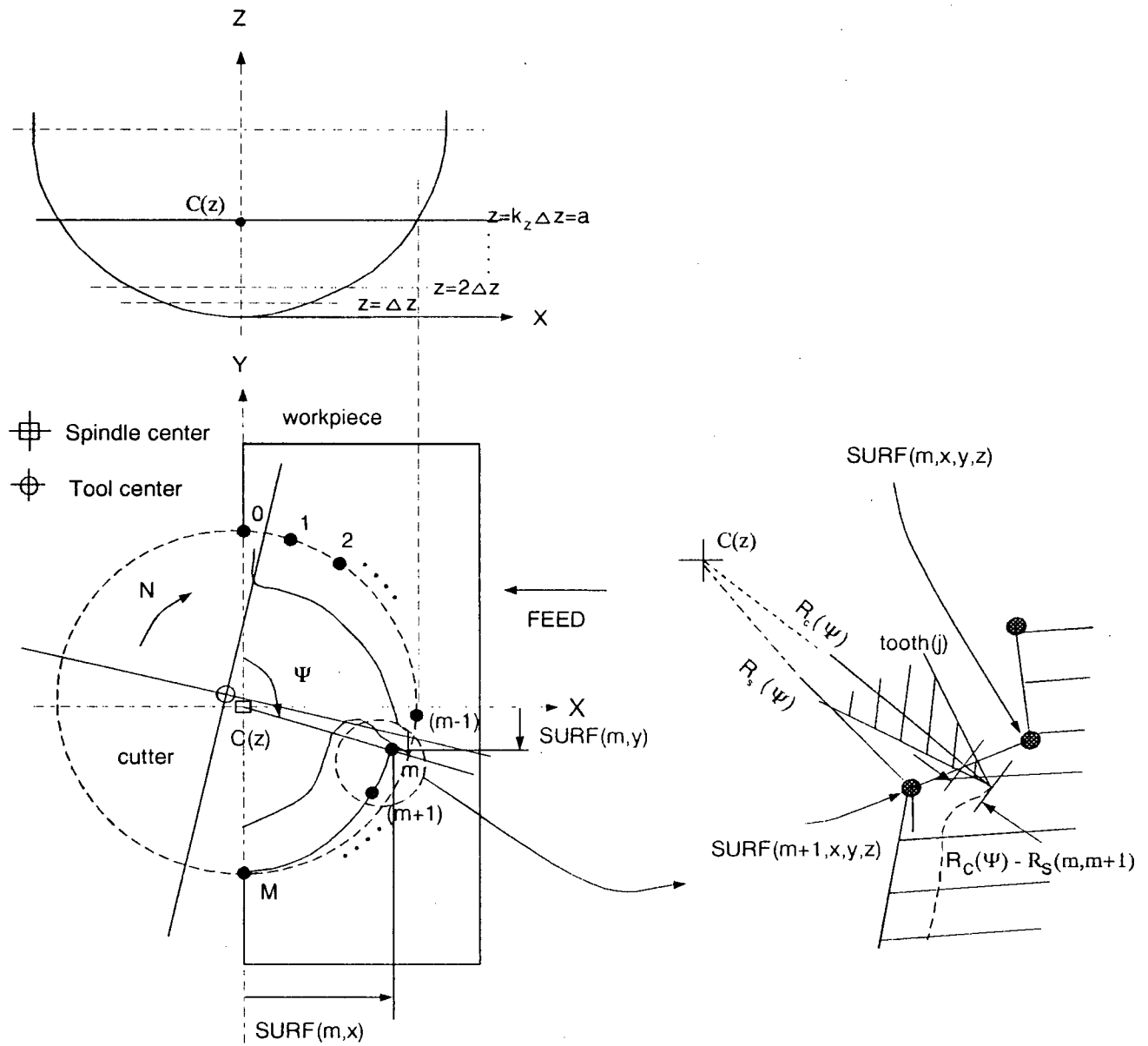


Figure 5.4: Dynamic model and Chip thickness regeneration mechanism in milling

simplifying the analysis, it is reasonable to assume that the structural vibrations from the workpiece are negligible compared to the tools'.

5.2.2 Structural Dynamic Model

Since the depth of cut is small in ball end milling operations, the spindle-cutting tool assembly can be represented by two orthogonal degrees of freedom in the the feed (x) and normal (y) directions lumped at the tool tip, see Figure 5.3. The cutter-spindle assembly is assumed to be rigid in the axial direction. The modal parameters of the structure are experimentally identified, and represented by two mutually perpendicular orthogonal modes in the x and y directions.

$$\begin{aligned}\ddot{x}'(t) + 2\zeta_x\omega_{nx}\dot{x}'(t) + \omega_{nx}^2x'(t) &= \frac{\omega_{nx}^2}{k_x}F_x(t) \\ \ddot{y}'(t) + 2\zeta_y\omega_{ny}\dot{y}'(t) + \omega_{ny}^2y'(t) &= \frac{\omega_{ny}^2}{k_y}F_y(t)\end{aligned}\tag{5.14}$$

where $(\omega_{nx}, \omega_{ny})$, (ζ_x, ζ_y) and (k_x, k_y) are the natural frequencies, structural damping ratios and stiffness in feed (x) and normal (y) directions, respectively. The $F_x(t)$ and $F_y(t)$ are the dynamic cutting forces calculated according to the model presented in the previous section. The equations of motion (Eq. 5.14) are evaluated separately at each discrete time interval Δt using recursive, discrete equivalent of the continuous differential equation. The discrete time domain solution of Eq. (5.14) was given earlier in Eqs. (5.6) and (5.7).

Chip Thickness Estimation: The arc of cut is divided into $M = \Theta_s/\Delta\theta$ angular segments, and the corresponding points on the arc of cut are stored in an array for each discrete axial element, see Figure 5.4. In the subsequent revolutions, the structural displacements are considered. The cutting edge penetrates into the workpiece due to the

rigid body feed motion combined with the structural vibrations of the milling system.

At each time interval t , the cutter undergoes a rotation angle of $\theta(t) = \omega \times t$, where $\omega[\text{rad/s}] = 2\pi N$ is the angular speed and $N[\text{rev/s}]$ is the spindle speed. The table moves in the negative x direction with a feed speed of $f[\text{mm/s}]$. Therefore, the x coordinates of all points on each axial layer z_k of the surface, represented by points $m = 0, 1, 2, \dots, M$, are updated at each time interval Δt by amount of incremental feed motion $f \times \Delta t$.

$$SURF(m, z_k, x) = SURF(m, z(k), x) - f\Delta t \quad (5.15)$$

for all m , and k

Depending on the magnitude and velocity of the vibration, the cutting edge point may be anywhere in the $x - y$ plane of the cut. The two points, which are generated in the previous tooth period and are closest to the new cutting edge location, are identified by searching the previous surface array, see Figure 5.4. Using a linear interpolation between the two points, the point $P_s(m) = \{x_s(m), y_s(m)\}$, which lies on the radial vector $R_c(k_z, t)$ but on the previously generated surface is evaluated.

The radial distance between the point $P_s(m)$ and the spindle center is given by,

$$R_s(k_z, m, t) = \sqrt{x_s(k_z, m, t)^2 + y_s(k_z, m, t)^2} \quad (5.16)$$

The actual chip thickness is found by projecting the difference in the radial distances on the line which is passing through the ball center (figures 5.3 and 5.4),

$$h(t) = [R_c(k_z, t) - R_s(k_z, m, t)] \sin \kappa \quad (5.17)$$

where κ has been given in chapter 3 as:

$$\kappa = \sin^{-1} \frac{R(\psi)}{R_0} \quad (3.19)$$

If the value of the chip thickness is positive, the tooth is in cut and the milling force model presented in chapter 4 is used to determine the cutting force. Otherwise, the tooth has jumped out of the cut due to excessive vibrations and the cutting force in that case will be zero.

The chip thickness evaluation geometry is given in figures 5.3 and 5.4. As the cutter rotates at discrete ($\Delta\theta$) intervals, the material, which is swept by the cutting edge due to its rigid body and vibration motions, is identified and the surface points are updated. Thus, at any time, the surface array *SURF* has M number of points per axial level which represent the instantaneous arc of cut. Since the axial depth of cut is divided into K_z number of layers, $M \times K_z$ number of points represent the entire, semi-spherical shape cut surface.

The simulation strategy is summarized as follows:

- The cutter is divided into equal number of elements in the axial direction.
- The radial planes of all axial elements, the arc of cut at each level, are digitized by equal number of points.
- Using the exact kinematic of milling the rigid body motion of each point on the cutting edge is calculated, and subtracted from the surface point left in the previous tooth period to calculate the chip thickness. By including static or dynamic displacements of the cutting edge point, the regenerative chip thickness can be calculated as well.
- The cutting force coefficients are evaluated for each local chip thickness from orthogonal cutting data base using oblique transformation model.
- The cutting forces for all cutting edge points which are in contact with the material are evaluated one by one, and summed and resolved in the x, y and z directions.

- The cutting forces are applied on the structure, vibrations are obtained. (or static deflections if the mass and damping are neglected).
- The surface is updated, the cutter is rotated one angular increment, and the solution is repeated.

5.3 Chatter Stability

The previous section provides an effective tool in predicting the onset of chatter in various milling operations and forms a basis to the “stability lobe” diagram, where the values for chatter free depth of cuts are shown like the one in Figure 5.5 analyzed by Smith and Tlustý [23]. The diagram is plotted on axes of axial depth of cut versus spindle speed. The curve shown in the diagram represents the limit of stability and separates the unstable machining conditions from the stable conditions. The stability chart provides useful information for a range of milling operations, indicating which combinations of axial depth of cut and spindle speed will be stable.

The stability lobe diagram can be best explained by examining the regeneration mechanism, in particular, the phase difference between the inner and outer modulations on the surface. As shown by Tlustý [23], the “regeneration of waviness” is the dominant factor in self-excited vibration. In vibratory milling, each cutting tooth removes a wavy surface created by the preceding tooth, and due to excessive vibration, creates another wavy surface. The phasing ϵ between these subsequent undulations is determined as:

$$N_w + \frac{\epsilon}{2\pi} = \frac{f_c}{N * N_f} \quad (5.18)$$

where N_w and ϵ are the integral and fractional number of waves between current and previous surfaces, and f_c is the chatter frequency [Hz].

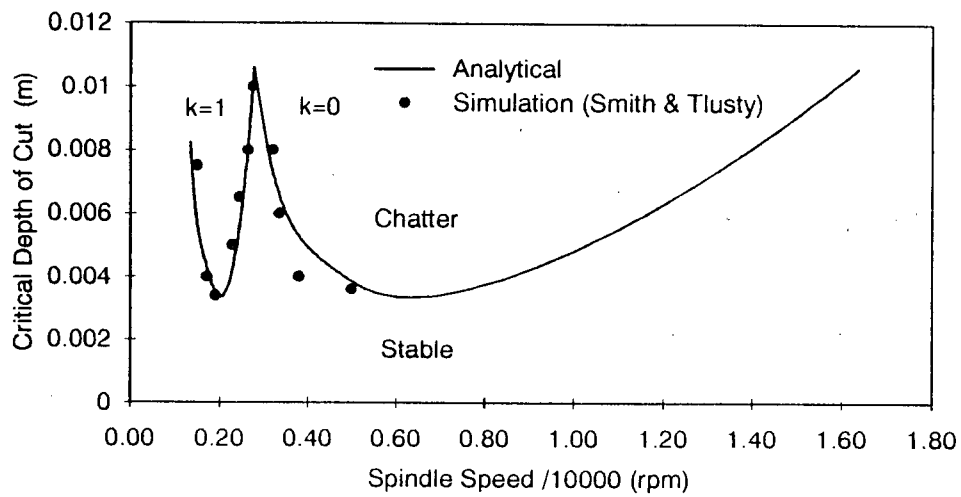
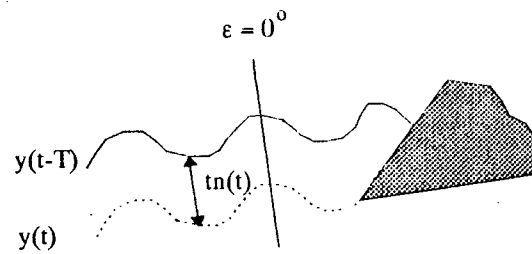
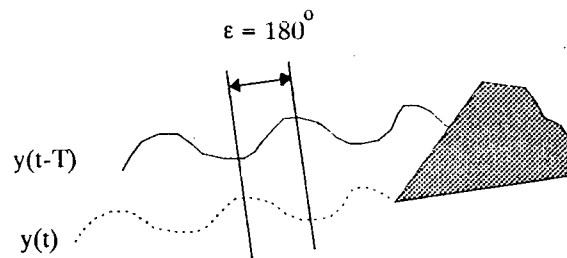


Figure 5.5: Analytical and time domain stability limit predictions for a case analyzed by Smith and Tlustý



a)



b)

Figure 5.6: Phase difference between the current and previous surfaces resulting from tool vibration

As shown in Figure 5.6, maximum variation in chip thickness occurs when the phase shift between two surfaces is π , which causes cutting force variation to excite vibration. On the other hand, constant chip thickness (stable cutting) is obtained when there is zero phase shift, and at certain values of ϵ , maximum self-excitation results. For each integral number of wave number N_w , due to different possible values of ϵ , the stability of the system changes, as reflected in the changing height of each "lobe". At low cutting speeds, the stability is high due to the presence of process damping associated with the tool flank face/workpiece interference [43]. Extensive efforts have been spent on the estimation of the process damping. Montgomery [1] modelled the process damping by estimating the interference between the vibrating tool's flank face and the cut surface. Others [44, 45, 46, 47] have tried to identify the damping during the chip formation process by using the Dynamic Cutting Force Coefficients (DCFC), which are determined mainly from experiments. In general, the process gains additional stability at low speeds where there are more steeper and shorter vibration waves and hence larger damping. On the other hand, as the cutting speed increases, the stability lobes "expand", indicating a trend of increasing stability. Mathematically, this can be explained by the larger change in spindle speed required to produce the same change in ϵ according to Eq. (5.18). Therefore, the stable region between each lobe becomes wider as the spindle speed increases.

5.3.1 Prediction of Chatter Stability from Time Domain Simulation

This section presents a useful method for deriving the chatter stability diagram from the results obtained by using the time-domain simulation program developed which has the capability to predict the occurrence and severity of chatter vibrations under any practical milling conditions. In order to develop the stability charts as explained above, PTP (Peak-to-Peak) graphs are used. As indicated by Smith [33], the peak to peak values,

calculated by scanning the maximums and minimums of the vibration and cutting force signals, provide a useful and convenient way to interpret the results obtained from the simulations. A closed examination of the PTP values gives a good indication of the process's stability, which can be used to construct a stability diagram. The stability algorithm is set up as follows:

- Specify milling operation, tool geometry and cutting conditions.
- Select a range of spindle speeds and spindle speed step size.
- At each speed, a simulation with a small axial depth of cut (e.g. base $a = 0.5mm$ in our simulations) is performed initially to obtain the PTP data for chatter-free conditions.
- Normalize the PTP values (no chatter) for unit axial depth of cut.
- Run simulation program, stores maximum and minimum values of cutting forces and vibrations when the program reaches its steady state. Evaluate normalized PTP for each new axial depth of cut.
- Compare normalized PTP values with those obtained in the based case (without chatter). If they exceed the chatter-free values by a wide margin (25 percents in our simulations), the axial depth of cut is reduced, and vice versa.
- Simulations are then re-run with the new axial depth of cut.
- Simulation stops when the borderline axial depth of cut is found. Resets and re-starts for new cutting speed.

A detailed break down of the algorithm is provided in Figure 5.7. The simulation time step should be kept constant for the selected range of speeds, therefore longer

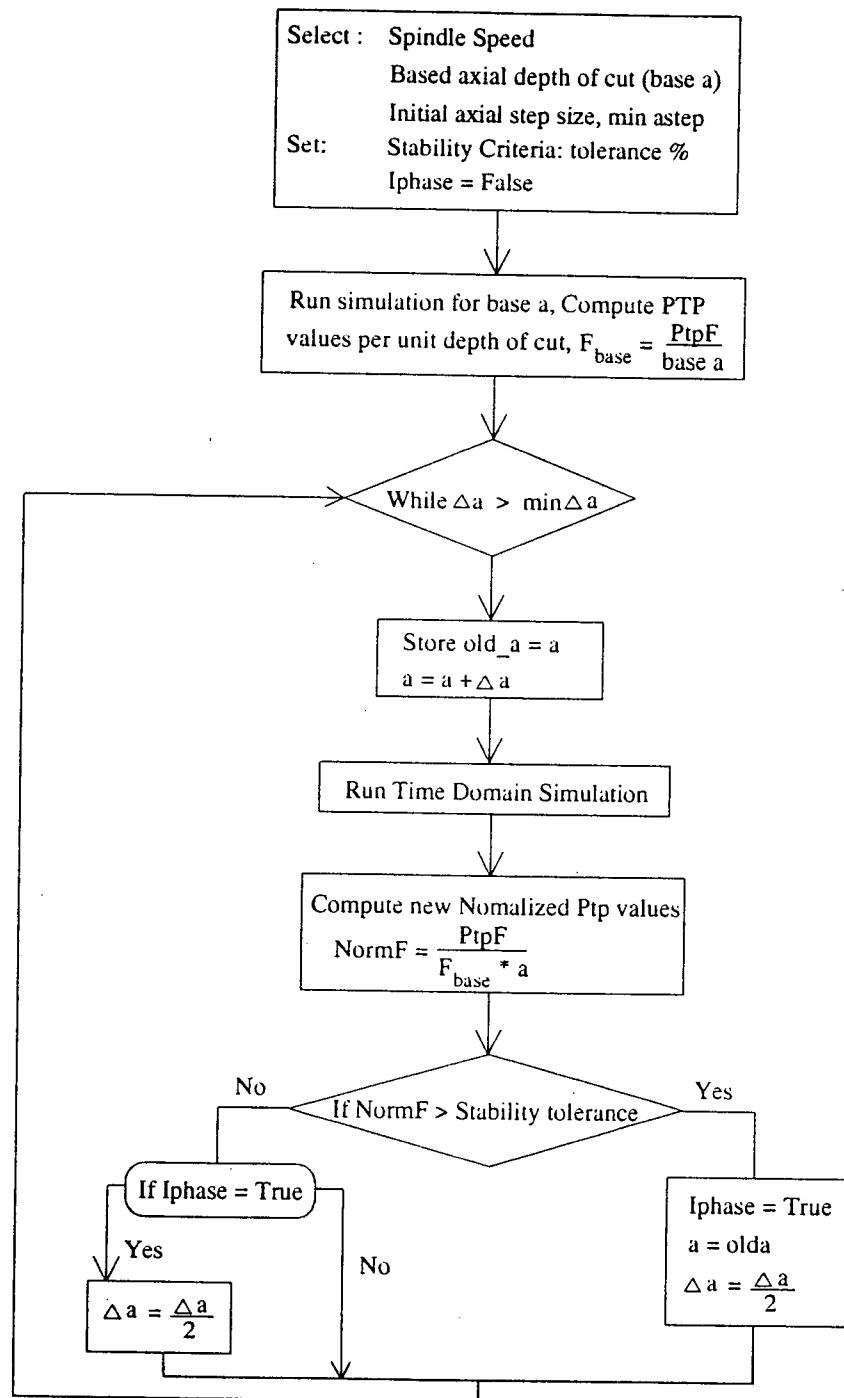


Figure 5.7: Time Domain Stability Limit Calculation Algorithm

time is required in computing the stability lobes at low cutting speed. Furthermore, it was noticed that, during the simulations, there is always a transient region before the simulation reaches a steady state, and that part of the signal should not be used in the PTP computation. The length of each simulation run can be shorten considerably, for the interest of efficiency, or experience, by reducing the number of cycles. However, in general, a simulation period of at least 25-30 cutter rotations should be used, to allow the simulation to reach a steady state condition.

Although the time domain model provides a clear and rather precise picture of each milling operation such as the structural displacements, chip thickness and cutting force variations, and the cut surface generation during the machining process, it often requires multiple runs, and each run sometimes involves extensive computation load, as in the case of simulating the cutting at low speed range, which makes it sometimes unacceptable for practical use. Recently, Budak [48, 31] presented a new method for the analytical prediction of stability lobes in milling. The method is based on the formulation of dynamic milling with regeneration in chip thickness, time varying directional factors and the interaction with the machine tool structure. A brief discussion of the method is given in the following:

The dynamic milling model is first expressed in terms of the time varying directional dynamic milling force coefficients $[A(t)]$ as,

$$\{F(t)\} = \frac{1}{2}aK_t[A(t)]\{\Delta(t)\} \quad (5.19)$$

where $\Delta(t)$ represent the dynamic displacements of the cutter structure at the present and previous tooth periods respectively. K_t is the constant cutting force coefficient. Due to the variable force vector in milling, the *time varying* directional matrix $[A(t)]$ is periodic at tooth passing frequency $\omega = N_f\Omega$ or tooth period $T = 2\pi/\omega$. It depends on the

immersion conditions and the number of teeth in cut. In a most simplistic approximation, Budak considered only the average component of the Fourier series expansion of $[A(t)]$, i.e. $r = 0$,

$$[A_0] = \frac{1}{T} \int_0^T [A(t)] dt \quad (5.20)$$

Transfer function matrix of the machine tool system ($[G(i\omega)]$) is then experimentally identified at the cutter/workpiece contact zone. By replacing the dynamic displacement term in Eq. (5.19) by the vibrations in frequency domain using harmonic functions, i.e.

$$\{\Delta(i\omega_c)\} = [1 - e^{-i\omega_c T}] e^{i\omega_c t} [G(i\omega_c)] \{F\}$$

where $\omega_c T$ is the phase delay between the vibrations at successive tooth periods T . Substituting $\{\Delta(i\omega_c)\}$ into the dynamic milling Eq. (5.19) gives,

$$\{F\} e^{i\omega_c t} = \frac{1}{2} a K_t [1 - e^{-i\omega_c T}] [A_0] [G(i\omega_c)] \{F\} e^{i\omega_c t} \quad (5.21)$$

To be able to obtain a non-trivial solution, the determinant of Eq. (5.21) has to be zero, i.e.

$$\det[[I] + \Lambda [G_o(i\omega_c)]] = 0 \quad (5.22)$$

The eigenvalue of the above equation can easily be solved for a given chatter frequency ω_c , static cutting factors (K_t, K_r) which can be stored as a material dependent quantity for any milling cutter geometry [19], radial immersion (ϕ_{st}, ϕ_{ex}) and transfer function of the structure.

Assuming only the two orthogonal modes are considered in $[G(i\omega)]$ (i.e. $G_{xy} = G_{yx} = 0.0$), the eigenvalue Λ is obtained as:

$$\Lambda = -\frac{1}{2a_0}(a_1 \pm \sqrt{a_1^2 - 4a_0}) \quad (5.23)$$

where a_0 and a_1 are constants and known for a given cutting geometry and structure.

The critical axial depth of cut at chatter frequency ω_c is obtained by taking the real part of the eigen value,

$$a_{lim} = -\frac{2\pi\Lambda_R}{N_f K_t}(1 + \kappa^2) \quad (5.24)$$

Therefore, given the chatter frequency (ω_c), the chatter limit in terms of the axial depth of cut can directly be determined from equation (5.24).

From Eq. (3.19), the angular distance travelled by the tooth due to chatter frequency ω_c at tooth period T is found as

$$\omega_c T = \cos^{-1} \frac{\kappa_p^2 - 1}{\kappa_p^2 + 1} = -\cos^{-1} 2\psi \quad (5.25)$$

Note that $\kappa_p = \Lambda_I/\Lambda_R = \tan \psi$ and ψ is the phase shift of the eigenvalue. Thus if k is the integer number of full vibration waves (i.e. lobes) imprinted on the cut arc,

$$\omega_c T = \pi - 2\psi + 2k\pi = \epsilon + 2k\pi \quad (5.26)$$

where $\psi = \tan^{-1} \kappa_p$ and $\epsilon = \pi - 2\psi$ is the phase shift between inner and outer modulations (present and previous vibration marks). The spindle speed $N(\text{rev/min})$ is simply calculated by finding the tooth passing period $T(s)$,

$$T = \frac{1}{\omega_c}(\epsilon + 2k\pi) \rightarrow N = \frac{60}{N_f T} \quad (5.27)$$

Therefore, by approximating the time varying milling directional factors by an average value, the stability limit can be solved analytically. For each chatter frequency, the eigen

value and the critical depth of cut are first obtained, then the corresponding spindle speed is computed for each stability lobe. The analytical formulation presented in this section was used as an additional tool to verify the predictions obtained from the time domain simulation. Preliminary evaluations of this method gave reliable and promising results. However, its adaptation to other complex cutter, such as ballend mills where there is a strong variation in the cutter and cutting geometries (hence variable directional coefficients) in the axial direction, is still unknown and will be kept out of the scope in this study.

5.4 Simulations and Experimental Verification

The dynamic milling model has been implemented in C programming language on SUN /SPARC workstation. The input data to the program includes the cutter geometry, workpiece material and dimensions, cutting conditions (axial depth of cut, radial immersion, chip load, spindle speed), machine tool dynamics, force model and coefficients, and other miscellaneous variables such as number of discretizing points on the cut surface and simulation time step. The simulation time step (sampling frequency) is selected to capture the highest vibration frequency in interest. As noted by Thusty [23], the sampling frequency should be at least ten times larger than the highest natural frequency of the system encountered. Each simulation runs in a series of small time steps for the chosen duration. At each instant, the cutting forces and tool deflections are recomputed, the surface geometry is updated and stored. The output of the simulation program contains milling force prediction, dynamic displacements of the machine tool structure, and the finished surface profile. In the following sections, the proposed simulation model will be tested on two different milling cutters under various cutting conditions. The simulated and experimental results will be provided in each case.

5.4.1 Verifications with Cylindrical End Mill

Static Cutting Simulations

The simulation model is first tested on a simple cylindrical cutter geometry. In the first run, rigid milling forces are simulated for a slotting operation and compared with the experimental results, see Figure 5.8. The work material *Ti6AL4V* was milled by a single fluted carbide end mill ($R_0 = 9.525mm$) with 30 degree helix angle. Different feed rates were chosen at an axial depth of cut $a = 7.62mm$ and a spindle speed of $269RPM$. The cutting force pattern is periodic at a tooth passing frequency. In a slotting operation, the tooth, due to helix, has a total immersion period of $\pi + \tan(i_0) * a/R_0 = 206.5degrees$. The axial forces are usually small in endmilling due to negligible cutting velocity in the axial direction. It can be seen that there is good agreement between the predictions and the experiments.

Dynamic Cutting Simulations and Verifications

To verify the dynamic model established, the chatter simulation program is tested in an end milling experiment with a cylindrical cutter investigated by Weck, Altintas and Beer [49] at the Machine Tool Laboratory of Technical University of Aachen. The workpiece material is aluminum alloy AlZnMgCu 1.5 which is machined with a 30 mm diameter, three fluted helical end mill with 30° helix angle and 110 mm gauge length. The measured milling force coefficients are $K_t = 600MPa$ and $K_r = 0.07$. The tests were conducted under a wide range of spindle speeds, axial depth of cuts, and radial width of cuts. The dynamic parameters of the end mill, which has one dominant mode in each direction, were determined from modal tests as:

$$\begin{aligned} k_x &= 5590N/mm & \xi_x &= 0.039 & \omega_x &= 603Hz \\ k_y &= 5715N/mm & \xi_y &= 0.035 & \omega_y &= 666Hz \end{aligned} \quad (5.28)$$

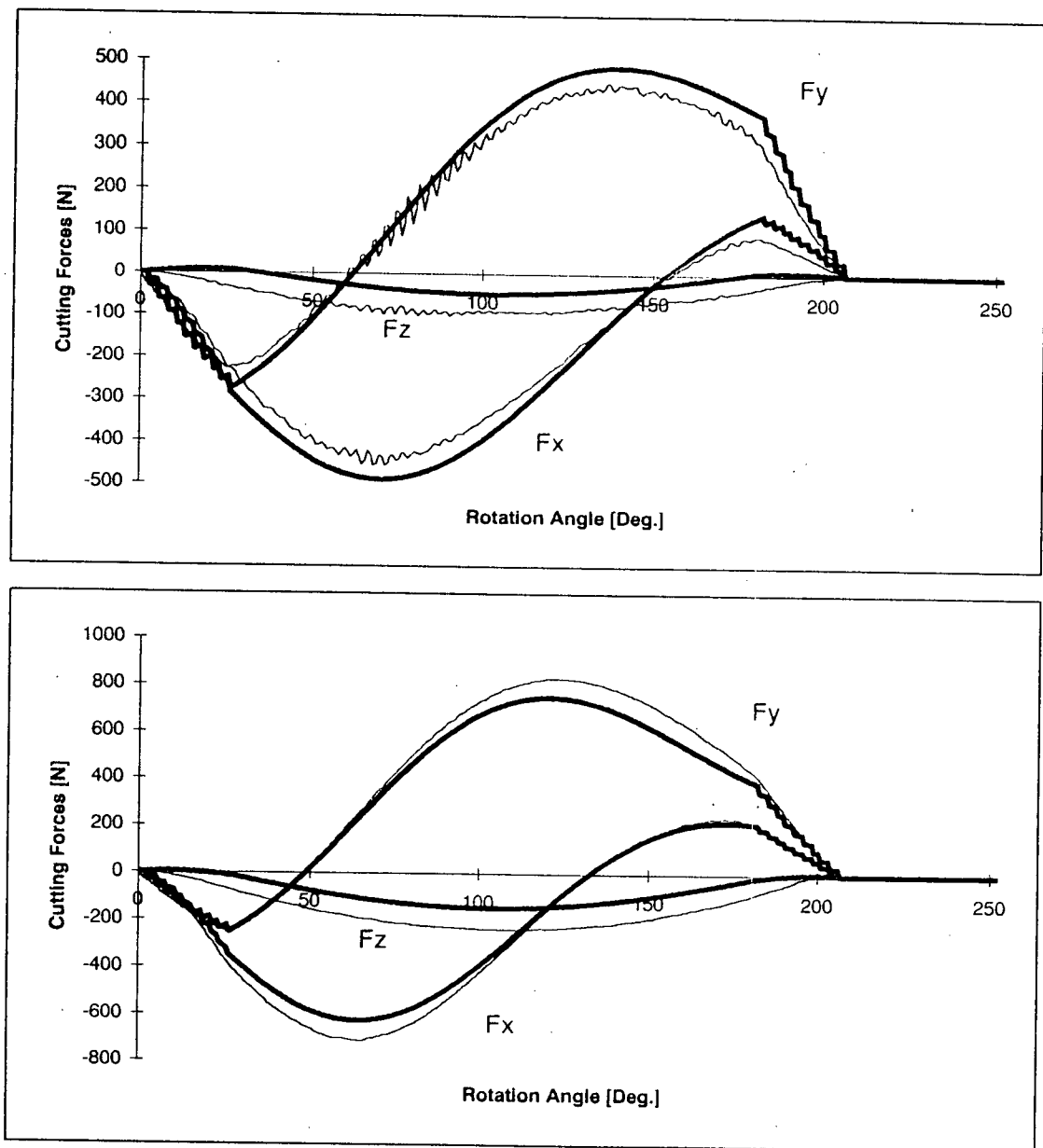


Figure 5.8: Experimental and Simulated Cutting Forces, cylindrical end milling

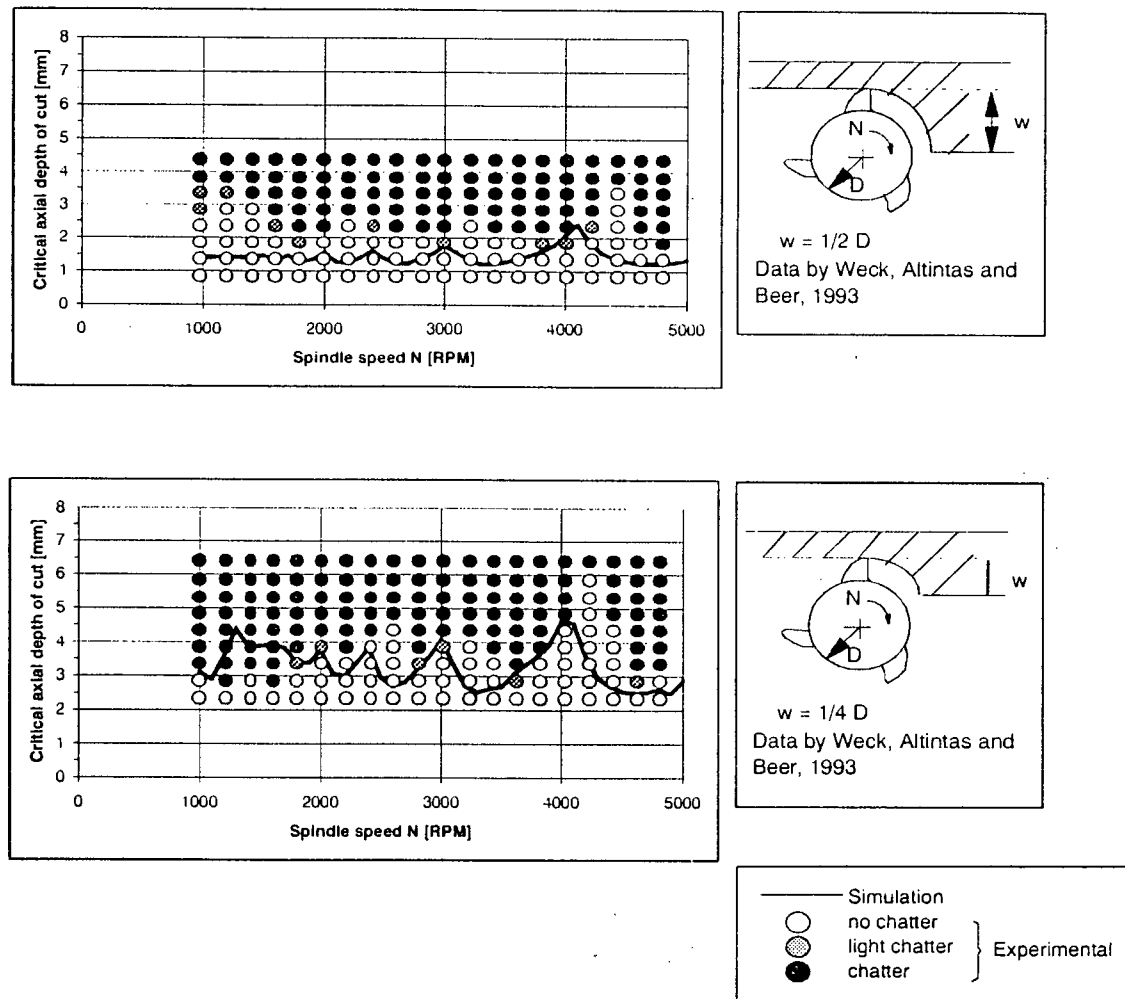


Figure 5.9: Stability Lobe Diagram for Cylindrical End milling. Weck's Experiments

Their results, summarized in the form of stability curves, are reproduced and shown in Figure 5.9 for two up-milling cases. A fixed feed rate of $s_t = 0.07\text{mm/tooth}$ was used in all tests and those stable and unstable cutting conditions are identified. Each small circle represents one experimental observation at a particular cutting speed and axial depth of cut. While an empty circle implies that a stable cutting condition was achieved, a solid circle represents a clear occurrence of chatter under that particular cutting condition, characterized by a rapid and significant increase in the energy level (both cutting force and vibration amplitudes) concentrated at the chatter frequency.

A series of chatter simulations were then run to verify Weck's experimental results. The spindle speed was chosen as 3000RPM and the occurrence of chatter was monitored by increasing the axial depth of cut in small steps ($\delta_a = 0.5\text{mm}$). All other cutting parameters are the same as those employed in Weck's experiments. The results of the simulated cutting forces and vibrations are shown in figures 5.10 and 5.11. A close examination of the simulation results reveals that chatter has developed substantially at approximately $a = 2.5\text{mm}$ to $a = 3\text{mm}$, signifies by a more than 100 percent jump in the magnitudes of both the cutting forces and vibrations. After this critical axial depth of cut ($a = 3\text{mm}$), the cutting forces continue to increase in a non-linear fashion and become unrealistically high. The system finally appears to have saturated and is no longer increasing with time.

After obtaining positive feedback from the initial simulations, a series of half immersion up-milling simulations were set up to generate a stability lobe chart. Figure 5.12 shows the PTP values recorded for different axial depth of cuts, ranging from 1mm to 3.25mm , and spindle speeds. Other cutting conditions are kept constant. Each simulation was allowed to run long enough to assure that steady state has been reached before the PTP are being evaluated. The PTP values for the last 5 revolutions (a total of 25 are used in all simulations) are shown here for a selected speed and axial depth

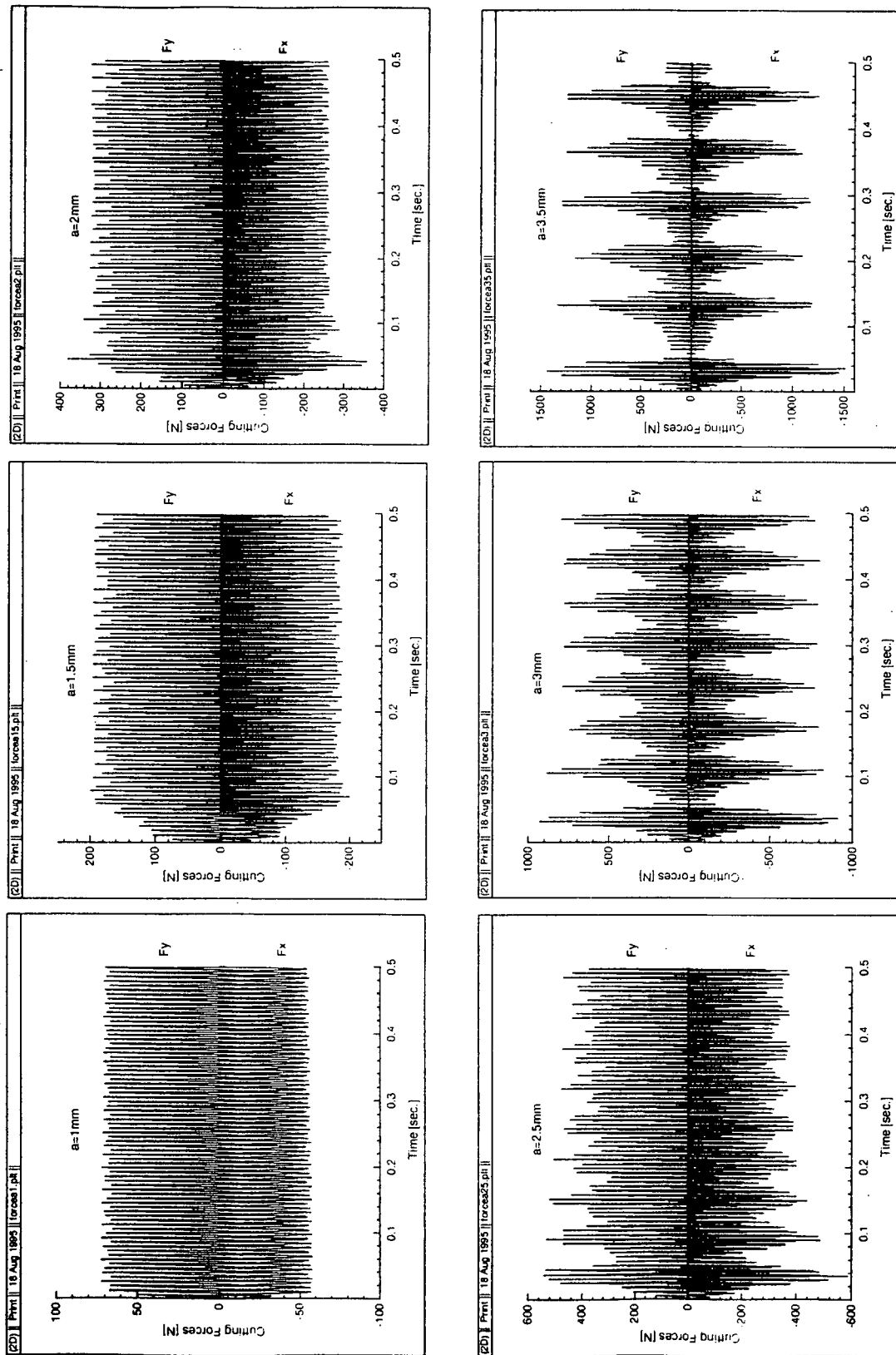


Figure 5.10: Cutting Force Simulation I, cylindrical cutter, Weck's experiments

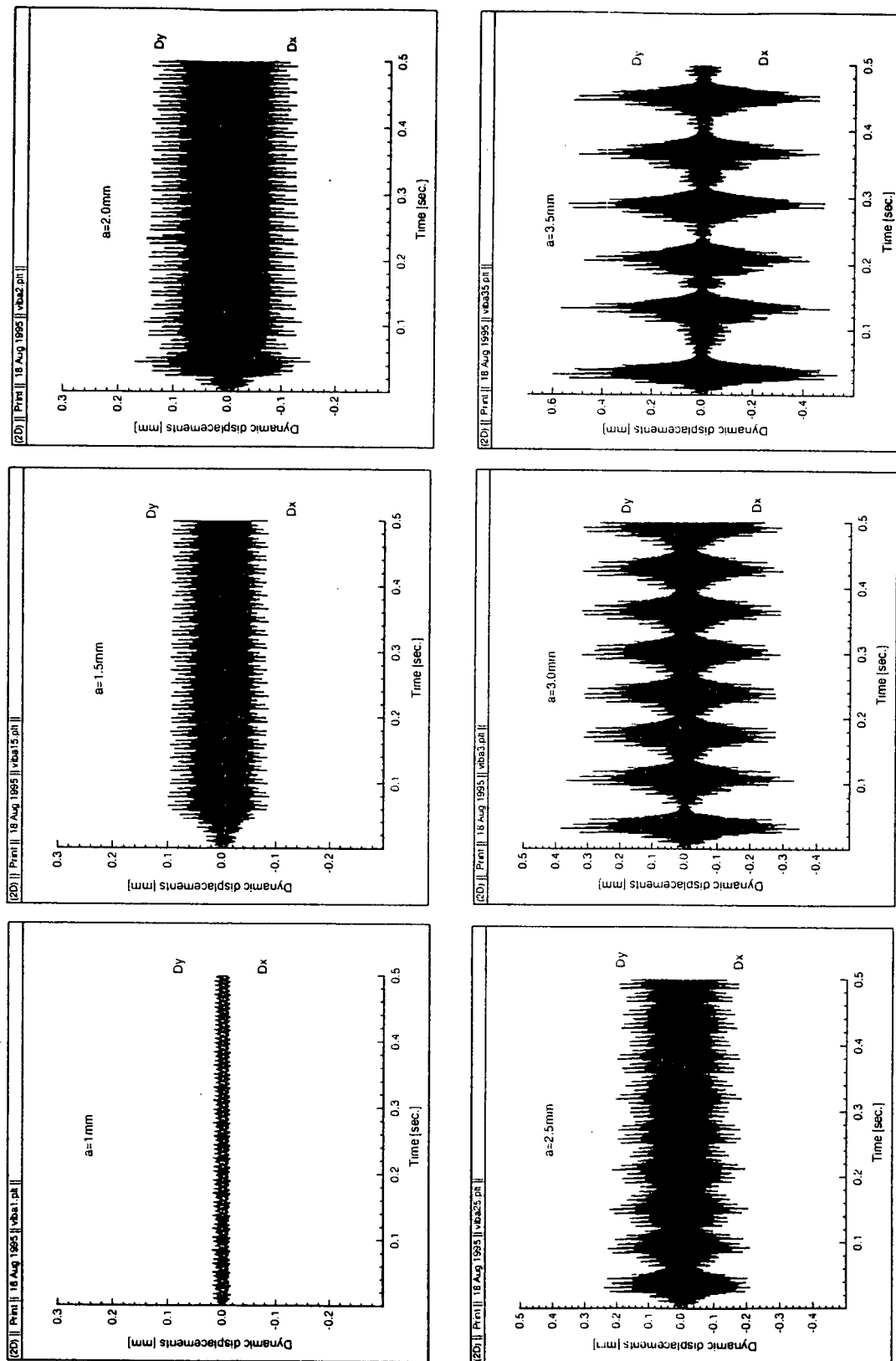


Figure 5.11: Vibrations Simulation I, cylindrical cutter, Weck's experiments

range. It can be seen that, the peak amplitude varies both axially and horizontally, implying that there exists some combination of axial depth of cut and spindle speed in which the cutting process is stable. Although the PTP graph gives good indication on the magnitude of the forces and vibrations for each cutting condition, it does not give direct information (interpolation of data required) to the process planners on selecting the stable axial depth of cuts and spindle speeds. Therefore, the algorithm presented in section 5.3.1 is tested on the PTP information for various speeds starting from 1000RPM up to 10000RPM in steps of 100RPM. The result is plotted on top of the experimental results observed by Weck in Figure 5.9. Discrepancy occurs due to the difference in the stability criteria employed in two cases. For instance, Weck's simulation algorithm "assumes that the process is unstable when the peak values of the vibration grow in thirty consecutive oscillation periods, otherwise the process is assumed to be stable" [49], while the method of PTP identification technique, which was proven to be a reliable tool, was used in this study. Furthermore, there exists no precise definition of chatter to be relied upon in conducting the experimental observations. In other words, the choice between assigning a "light chatte" and "chatter" to the observation, as indicated in Figure 5.9, is rather a subjective decision and remains to be justified. Although there are differences between the two, Figure 5.9 indicates that, the values predicted by the analysis are at least consistent and reasonably closed to those obtained by the experiments.

A separate simulation run, from which the results are shown in Figure 5.13, was performed at a lower speed of $N = 1000RPM$ to provide more understanding of machining under unstable conditions. A very high axial depth of cut ($a = 4mm$ which exceeds the stability limit based on the experimental results from Weck) was selected. Three characteristic regions can be identified in the tool's responses and the cutting force patterns. The first few revolutions represent the signals prior to the onset of chatter, where the amplitude of oscillation is small, increasing slowly with time. Its Fourier spectrum is

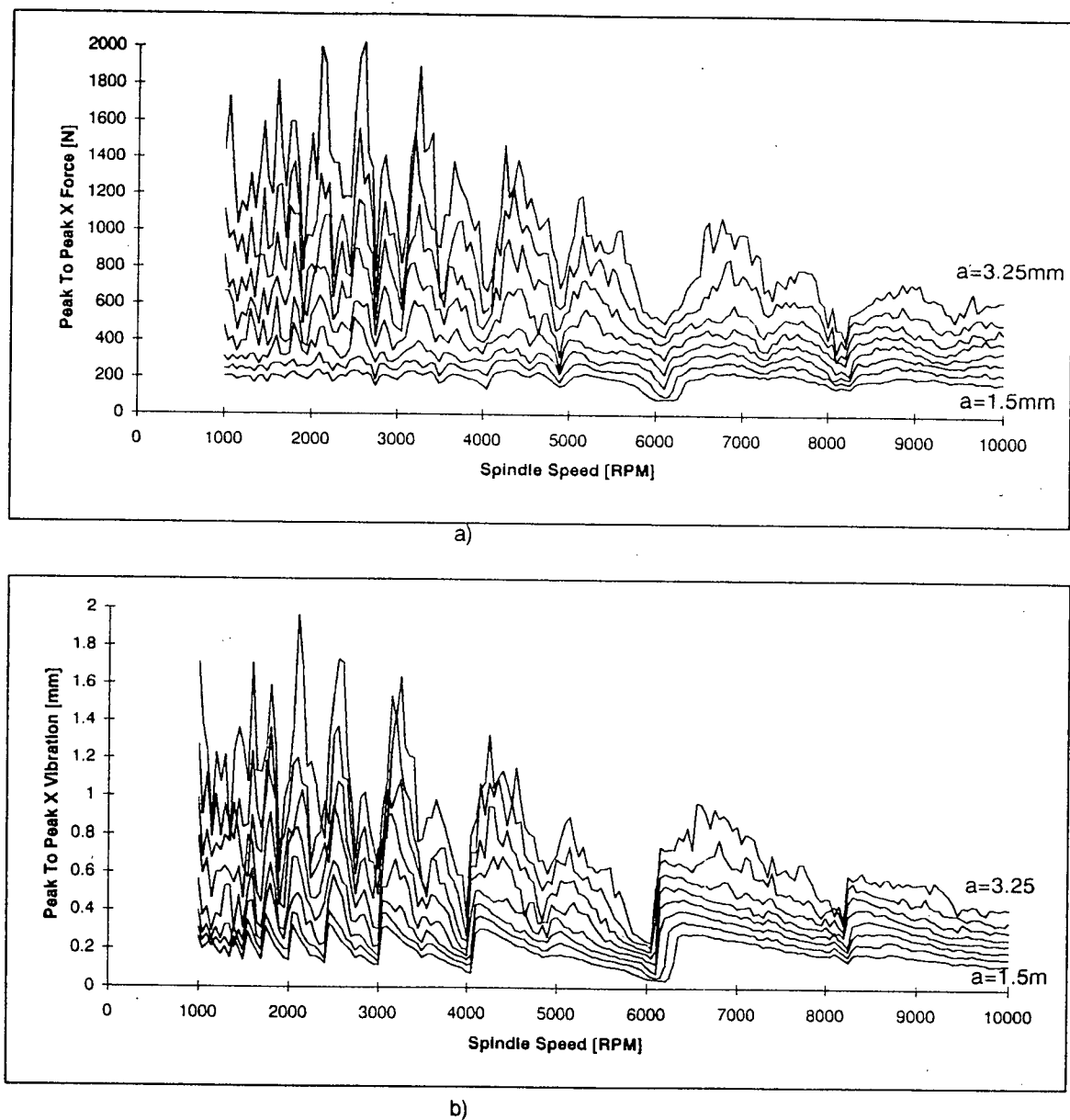


Figure 5.12: Peak To Peak Graphs from Time Domain Simulation I, cylindrical cutter. Weck's Experiments

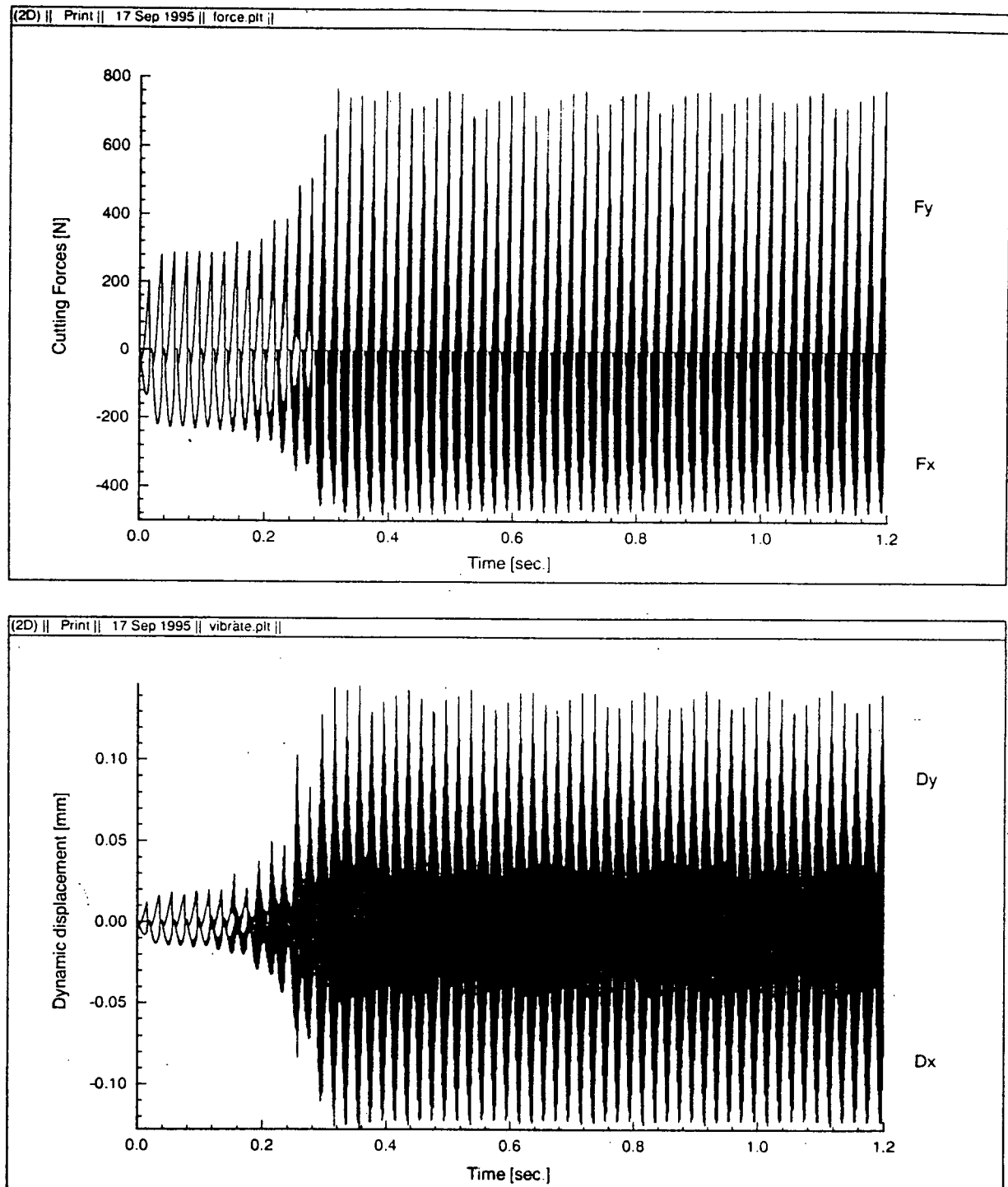


Figure 5.13: Cutting Forces and Vibrations Simulation II, Weck's Experiments

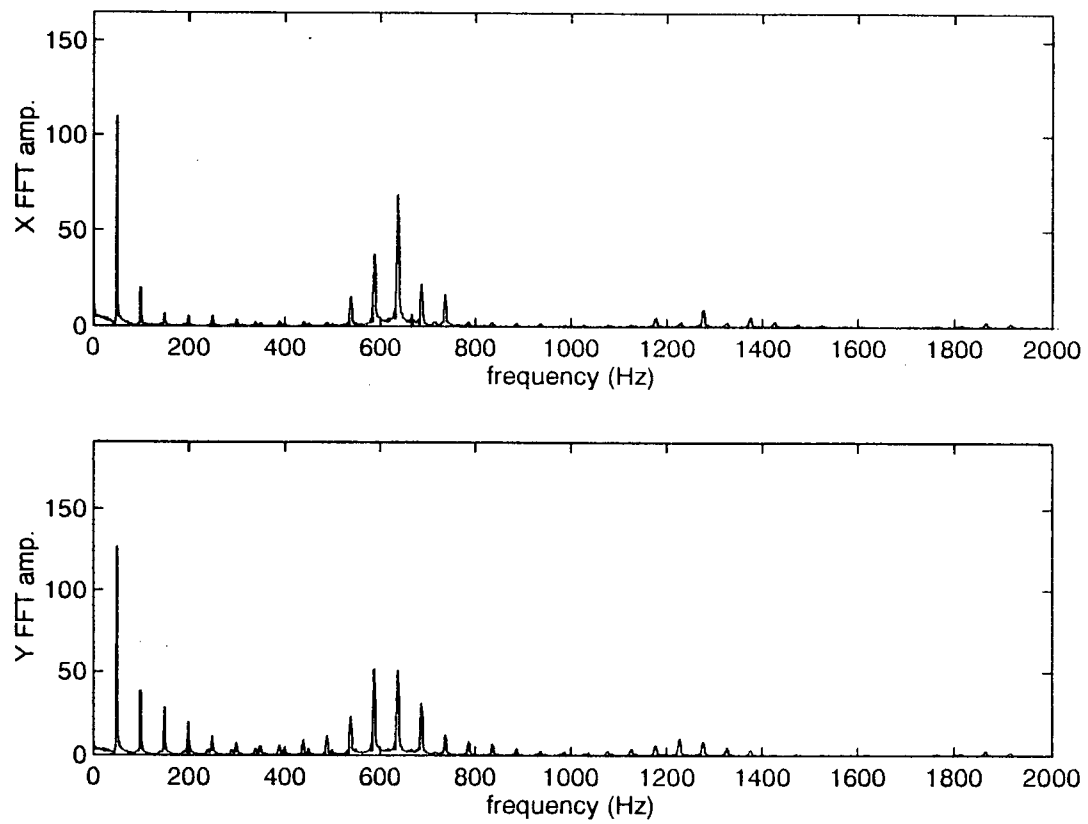


Figure 5.14: Fourier Spectrums from Simulations II, Weck's Experiments

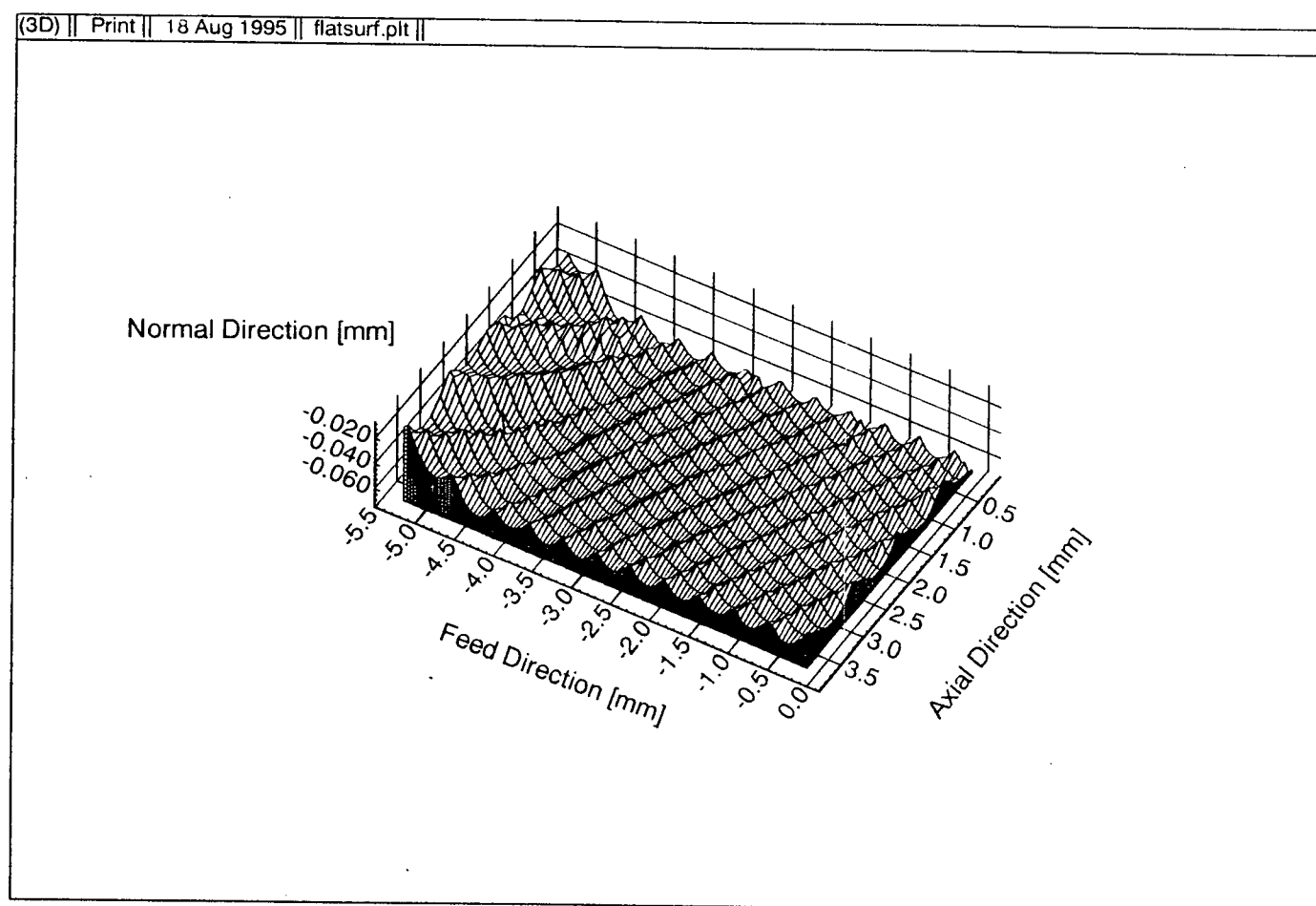


Figure 5.15: Simulated Surface under Chatter Condition, from Simulations II

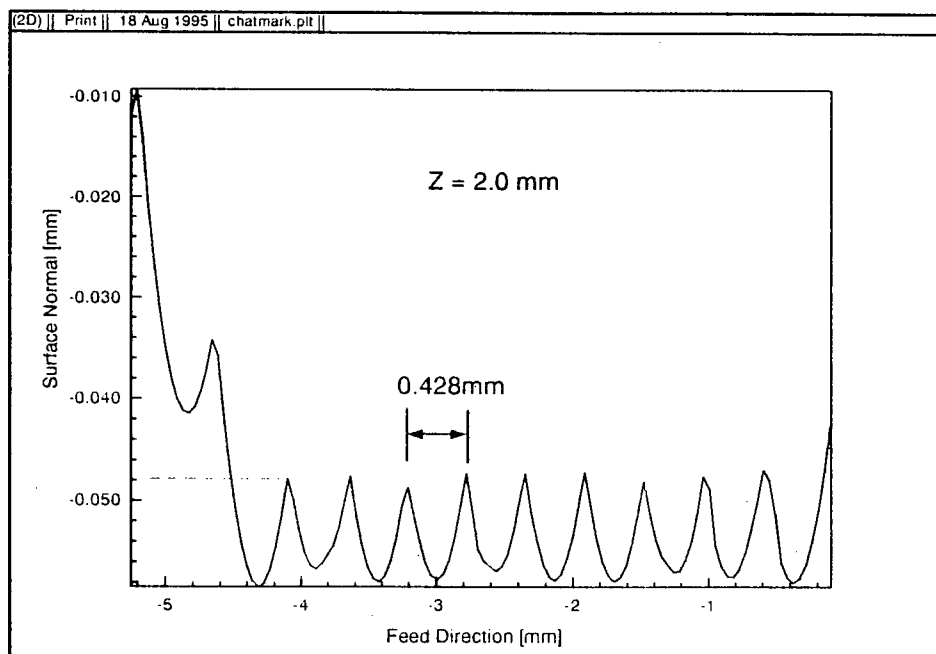


Figure 5.16: Simulated Surface Mark at $z = 2.0\text{mm}$ under Chatter Condition, from Simulations II

distributed in a wide bandwidth around the tooth's passing frequency (333Hz). During the next several revolutions, vibrations increase which modulate the chip thickness distribution and influence the cutting forces. This finally results in fully developed chatter in which the tool oscillates with a very high amplitude and at a frequency (chatter frequency) close to the structure's dominant natural frequency (600 Hz), see Figure 5.14. Figure 5.15 shows the simulated finished surface. As seen, the surface roughness is dominated by severe vibration marks which leave undulations of approximately 10 microns on the surfaces. The vibration marks left on the surface has a wave length λ of approximately 0.428mm. Since the workpiece is moving at a speed of 3.5mm/s, and the tooth period is $T_c = 0.02\text{sec.}$, that is, the wavy surface has a period of $T_{wb} = \lambda/f = 0.122\text{sec.}$, which is much greater than tooth period T_c or the vibration periods in either direction ($w_x = 594\text{Hz}(0.00168\text{sec.}), w_y = 675\text{Hz}(0.00148\text{sec.})$). This phenomena is consistent with the observation made by Montgomery [1], and referred to as *washboarding*, which exists due to the dynamic interaction between the vibrating (and rotating) cutter and the moving workpiece. As a result, there is an integral number plus a fraction of vibration cycles between successive tooth periods. The fractional waves accumulate in every N_w tooth periods, which leads to the low frequency wave left on the surface. In general, if the vibration frequency is different in the two directions, the resultant vibration frequency has to be known for accurate N_w estimation.

The time domain stability lobe simulation is further verified with the analytical chatter prediction outlined in section 5.3.1. The analytical formulation was implemented and tested under the cutting conditions similar to Weck's experiments. Figure 5.17 shows the results of two milling cases obtained from the analytical predictions and time domain simulations respectively. The excellent agreement confirms the accuracy and reliability of the time domain simulation model.

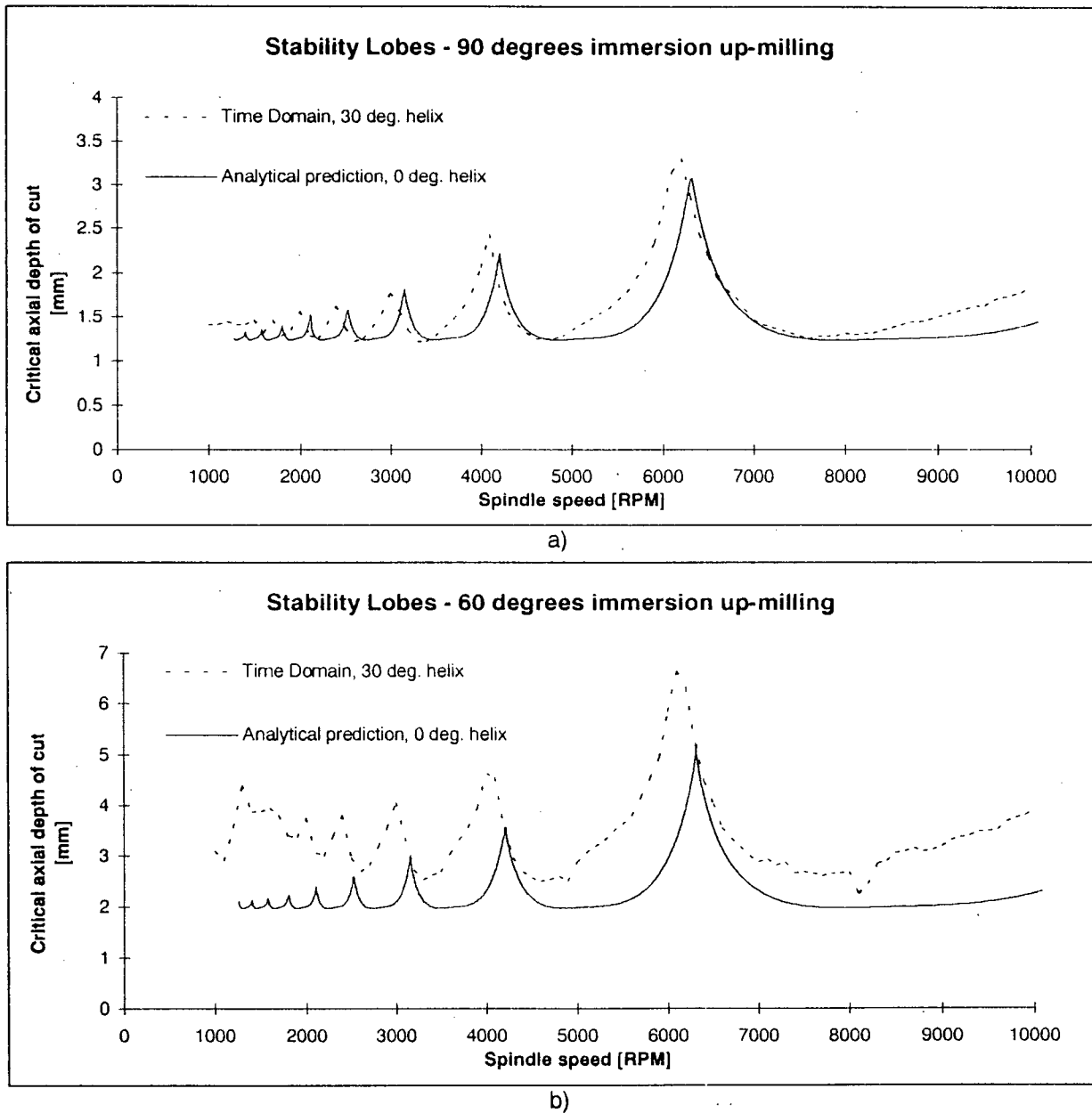


Figure 5.17: Analytical and Time Domain Predicted Stability Lobes, cylindrical cutter

5.4.2 Verifications with Ballend Mill

Static Cutting Simulations

In this section, rigid milling forces with ballend cutters are simulated and compared with the experimental tests shown in the previous chapter. The results of both the simulations and measured cutting forces are plotted for two different cutting geometries. Figure 5.18 shows the chip thickness profile at the cutting edge for a slotting operation. It can be seen that, during the first revolution, the chip thickness has not developed fully ($s_t = 0.0508\text{mm/tooth}$) as the cut surface has been initialized to the tool's geometry. The profile for the subsequent revolutions verify the correctness of the chip thickness prediction by the simulation. In figures 5.19, simulations of milling force with ballend cutter are shown separately for a slot cutting and a half immersion up milling operations. Comparison of the two shows good agreement between the predicted and the experimental cutting force patterns, except the slight numerical instability arises when the tooth leaves or enters the cut abruptly such as in the half-immersion case shown in the bottom diagram of Figure 5.19. This problem can be solved by increasing the integration step size.

The model is further tested by examining the simulated surface profile in rigid milling. Since there is no vibration in the process, the expected magnitude of the surface feed mark should be close to the analytical prediction derived by Martellotti [2]:

$$h = \frac{s_t^2}{8[R(z) + s_t N_f / \pi]} \quad (5.29)$$

where h is the height of the tooth mark above point of lowest level. It is a function of the feed rate s_t , the number of flutes N_f , and the radius of cutter R . For cutters which have variable radius in the axial direction, the height of the feed mark changes axially, as shown in Figure 5.20. Here, the variation of the feed marks at two axial locations ($z_1 = 0.27\text{mm}$, $z_2 = 1.08\text{mm}$) resulting from a single fluted ballend milling operation

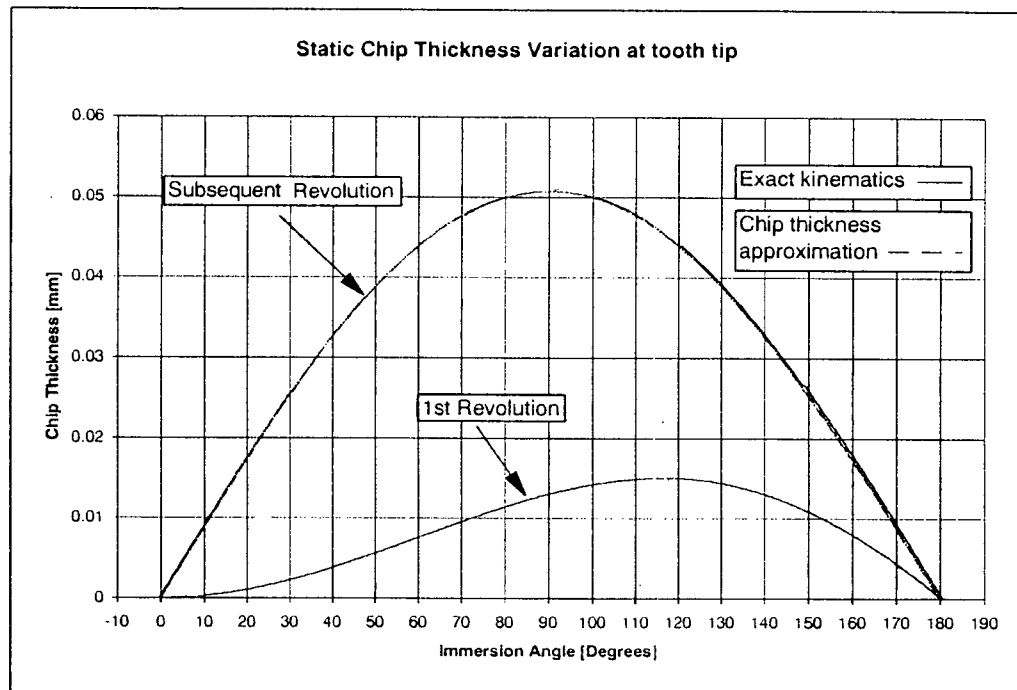


Figure 5.18: Model Verification I - Chip Thickness Profile

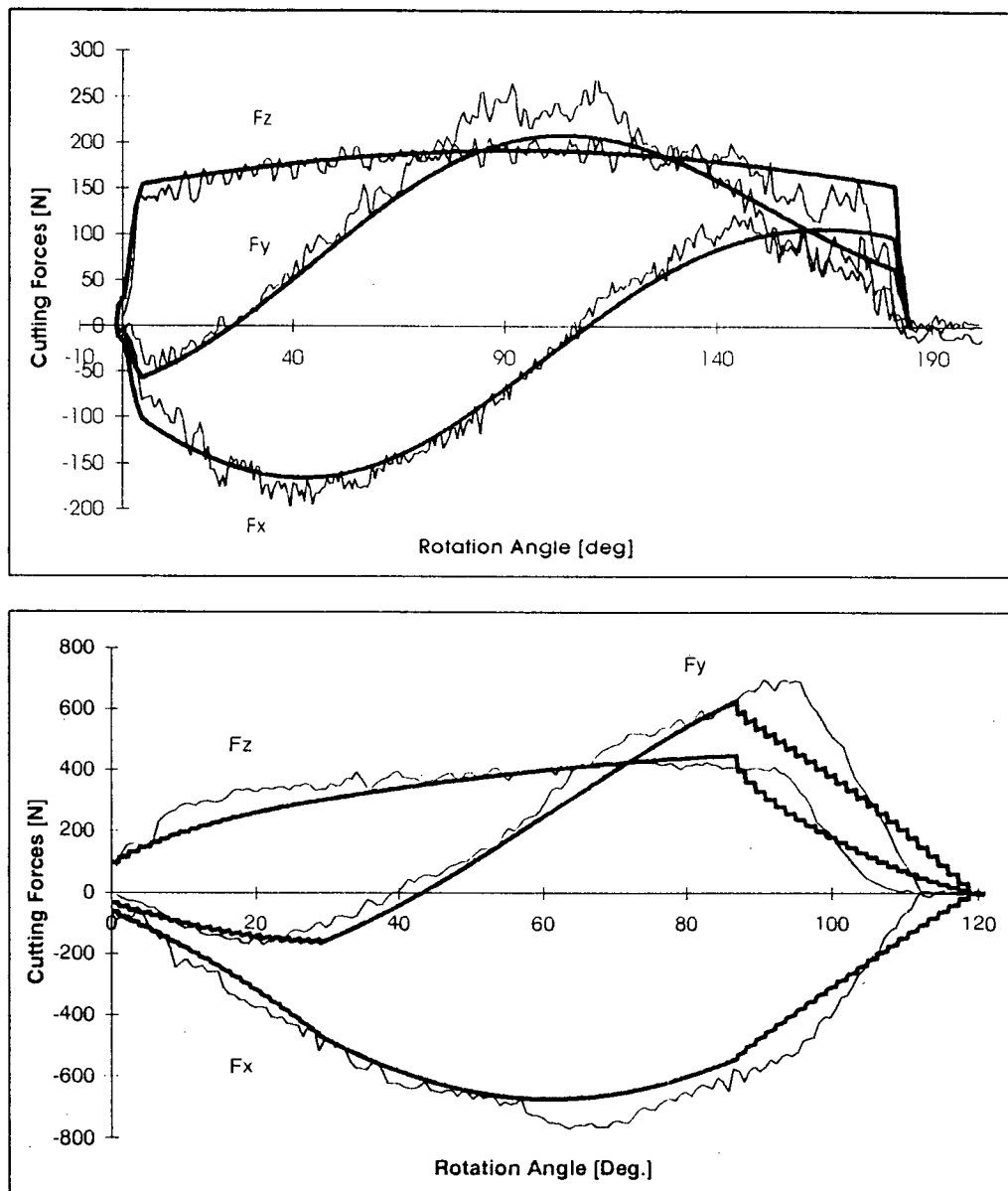


Figure 5.19: Model Verification II - Cutting Force Patterns

are shown. The feed rate, which is 0.0508mm/tooth , can be seen between the peaks of the marks. The value of h , calculated with Eq. 5.29, gives a value of 0.0001272mm at $R(z = 0.127) = 2.52\text{mm}$ and 0.00007296mm at $R(z = 1.08) = 4.405\text{mm}$, both showing good agreements with the predicted values.

The accurate prediction of vibration free, static milling forces on both cylindrical and ballend cutters verify the following facts about the model:

- The kinematic model of chip thickness calculation is correct.
- The oblique transformation method used in calculating the milling force coefficients from a general orthogonal cutting parameters is sufficiently accurate.

Dynamic Test and Simulation I

Ballend milling tests at different speeds were conducted to verify the dynamic simulations. A single fluted carbide ball end mill with 9.525 radius, 30 degree nominal helix and zero degree rake angle was used in slot milling of the titanium alloy with $a = 2.54\text{mm}$ axial depth of cut and feed rate of $s_t = 0.0508\text{mm/tooth/rev}$. The following sections outline the experimental procedure in identifying the dynamic characteristics of the ball mill attached to the spindle assembly of a SAJO vertical milling machine as well as presenting the experimental and simulation results.

Experimental Set-up: A PCB accelerometer is attached onto the structure close to the tip of the ballend cutter (see Figure 5.21). Transfer function at the tool tip is obtained by exciting the structure with an impact hammer and recording its force response through a HP 3562A dynamic signal analyzer. The identified dynamic parameters and cutting conditions are given in 5.1.

$$\begin{aligned} k_x &= 5590\text{N/mm} & \xi_x &= 0.039 & \omega_x &= 593.75\text{Hz} \\ k_y &= 5710\text{N/mm} & \xi_y &= 0.035 & \omega_y &= 675\text{Hz} \end{aligned} \quad (5.30)$$

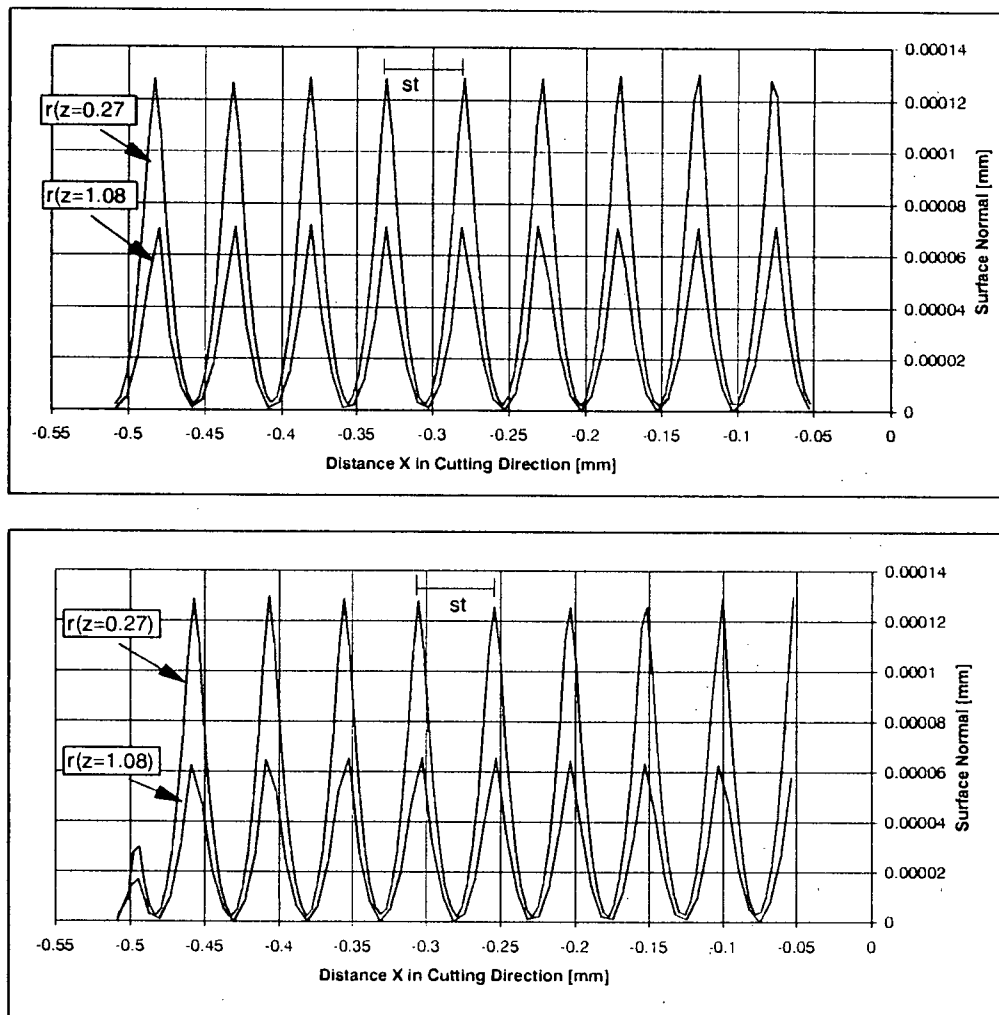


Figure 5.20: Model Verification III - Surface Feed Marks: a) $\Psi = 0^\circ$ (up milling side), b) $\Psi = 90^\circ$ (down milling side)

Due to the large static error results from integrating the signal measured by the accelerometer, the static stiffness of the system is measured by performing a static stiffness test and the result is shown in Figure 5.23. To verify the rigid workpiece assumption, the transfer function of the Titanium workpiece (150 X 100 X 80mm) is also measured and shown in Figure 5.24. In die machining, the workpiece is usually stiffer than the tool. Therefore, as proven by the measurement (about 3 times higher than the tool), only the dynamics of the tool is considered.

The performance of the model in predicting the dynamic milling process is illustrated by two sample time domain simulations and milling experiments. The tests were performed on a SAJO milling machine retrofitted with an in-house developed research CNC, and cutting forces were recorded on a PC through Kistler dynamometer and charge amplifiers. The cutting conditions for all cases were identical except the spindle speed and damping coefficients (see table 5.1) ¹. First the experimental results are shown in figures 5.25 and 5.26, together with the Fourier spectrums (see Figure 5.27). The experiments were repeated at spindle speeds $N=115$ rev/min to $N=1100$ rev/min in roughly 6 equal steps, at identical cutting conditions.

The measured and simulated cutting forces during low and higher speed milling tests are shown in figures 5.28 to 5.30 respectively. It was observed from the experimental results that the chatter vibrations are quite evident during the higher speed machining (figure 5.30), whereas there is almost no chatter at $N=115$ rev/min (figure 5.28). Since all the cutting conditions are identical except the cutting speed, the absence of chatter vibrations is attributed to the process damping which is known to be quite effective when the tooth passing frequency (i.e. cutting speed) is significantly lower than the vibration frequency. The process damping reflects the combined effects of tool flank penetrating,

¹Note: Damping Ratios of $\zeta_x = \zeta_y = 0.15$ are used at the low spindle speed ($N = 115RPM$) in milling simulation.

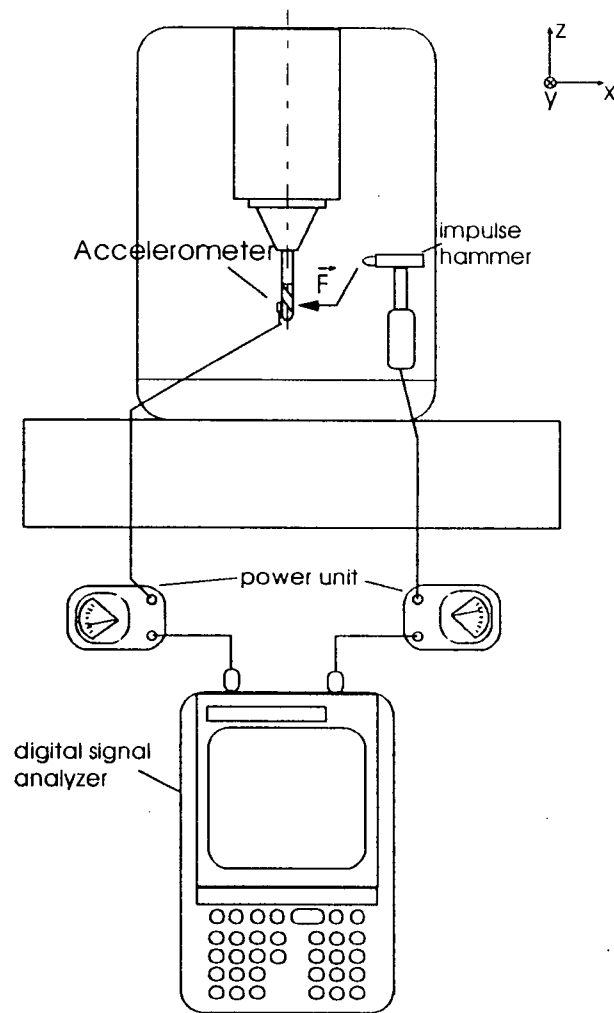


Figure 5.21: Experimental Setup - Dynamic Test

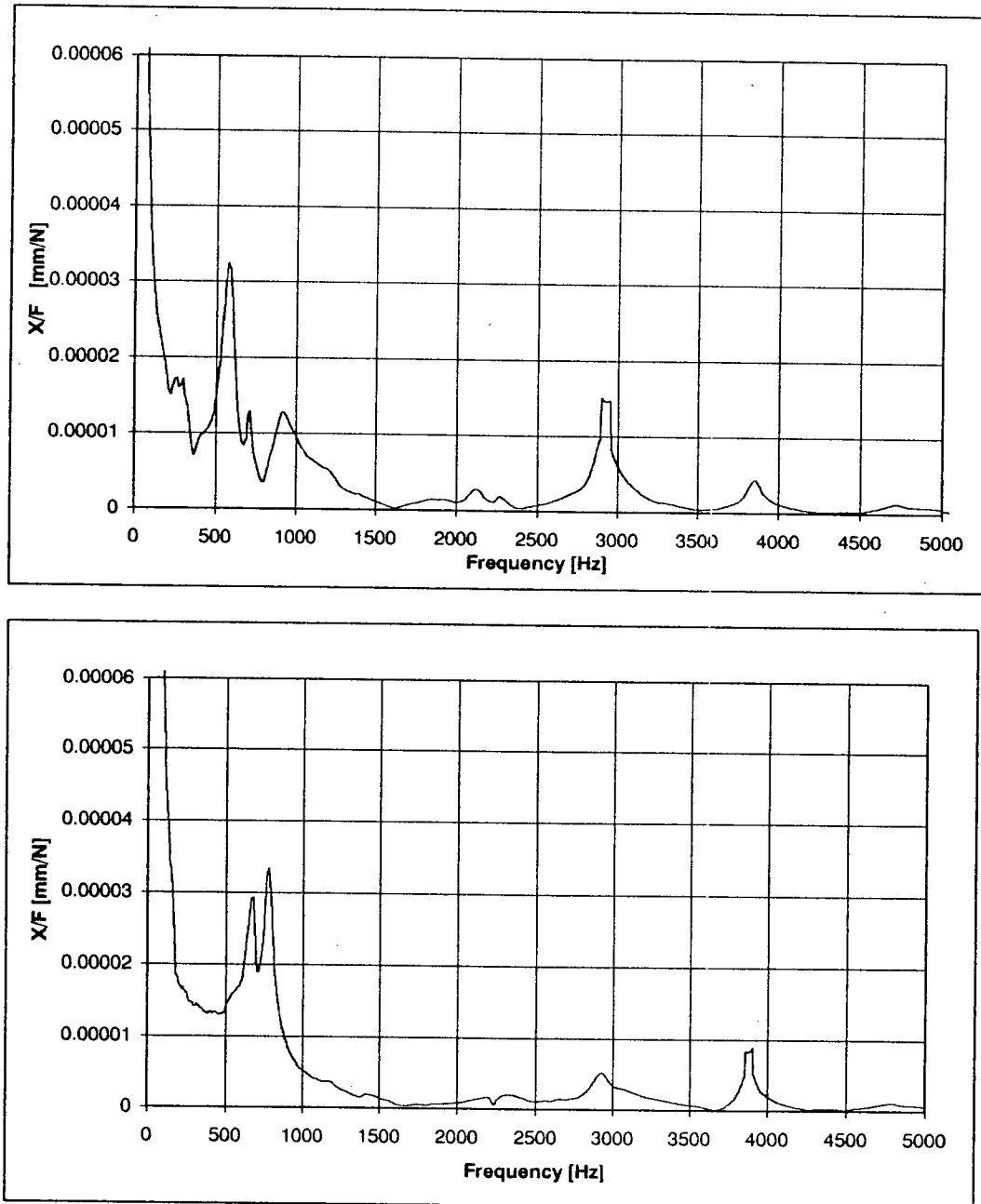


Figure 5.22: Measured Transfer Function at Tool Tip, Ballend Milling Test I

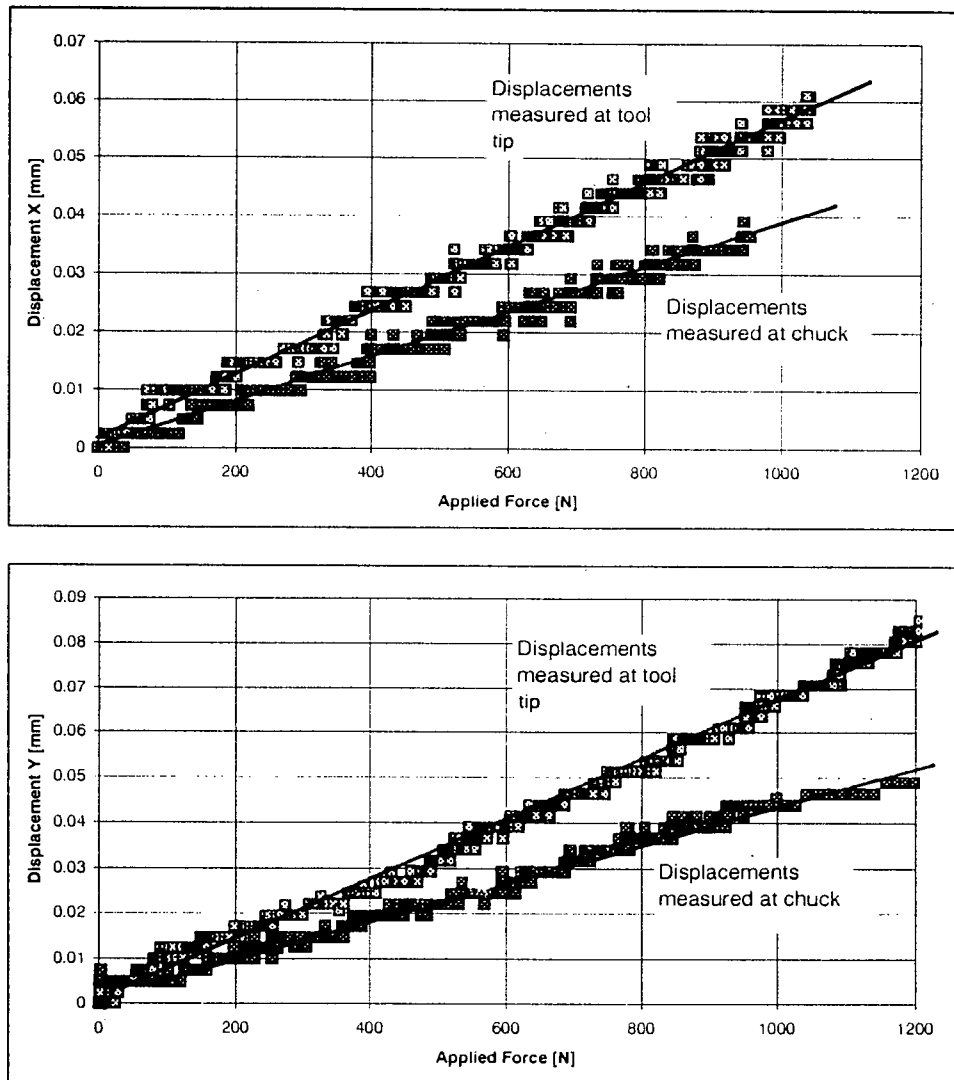


Figure 5.23: Static Stiffness Measurements, Ballend Milling Test I

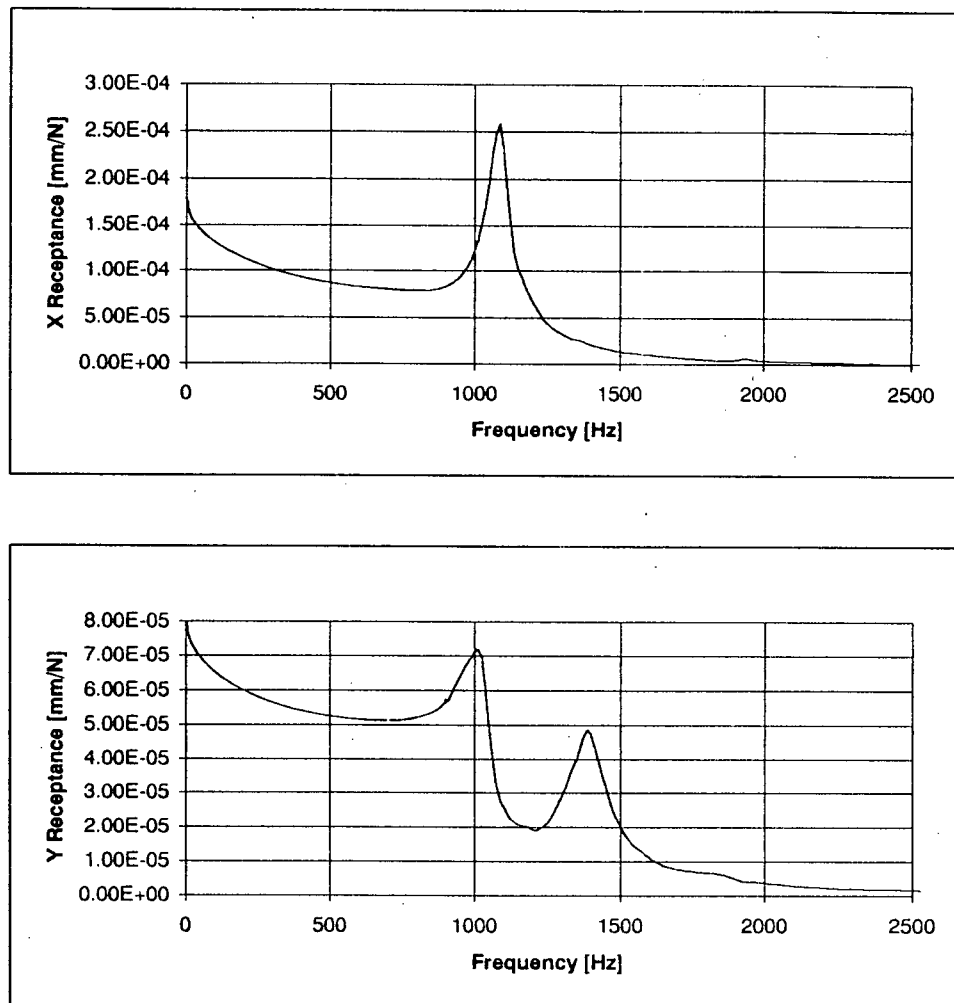


Figure 5.24: Measured Workpiece Transfer Function, Ballend Milling Test I

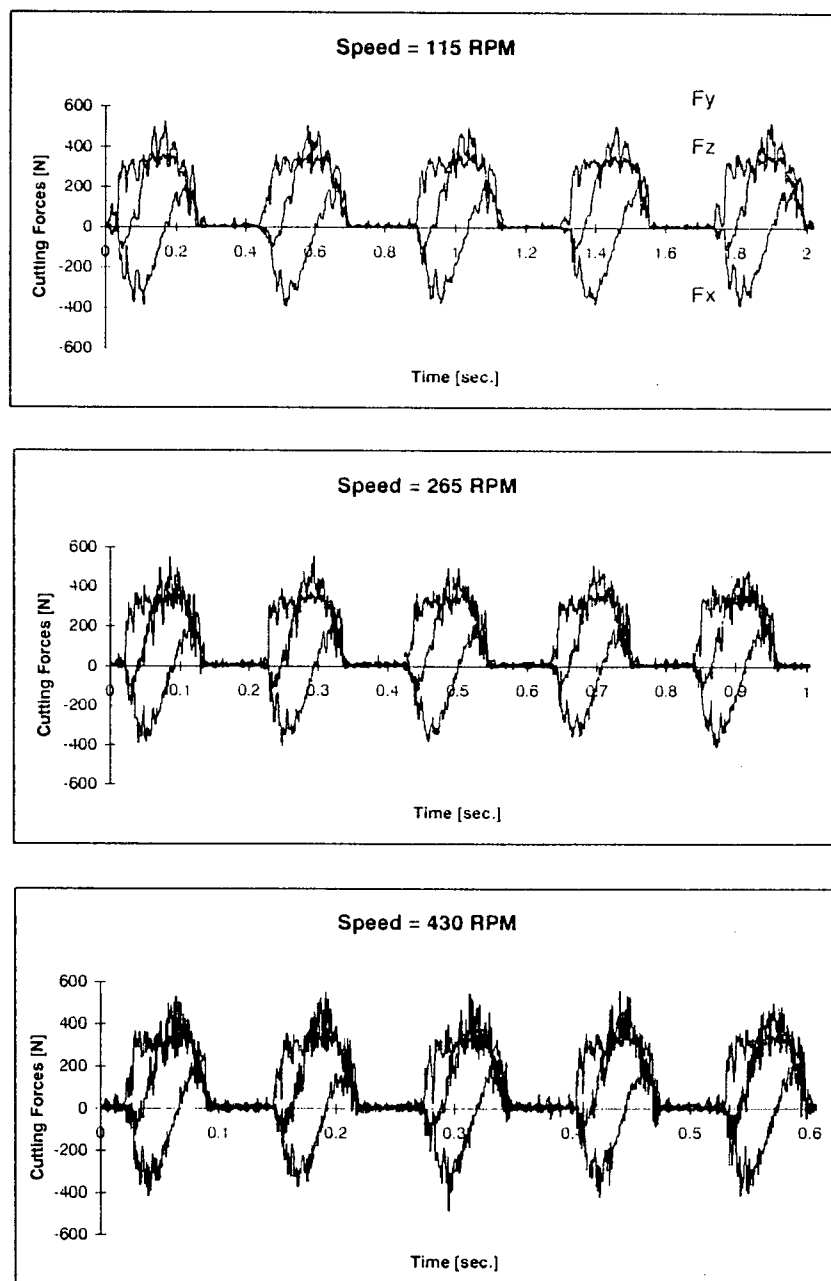


Figure 5.25: Dynamic Ballend Milling Test I, Speed = 115-430 RPM

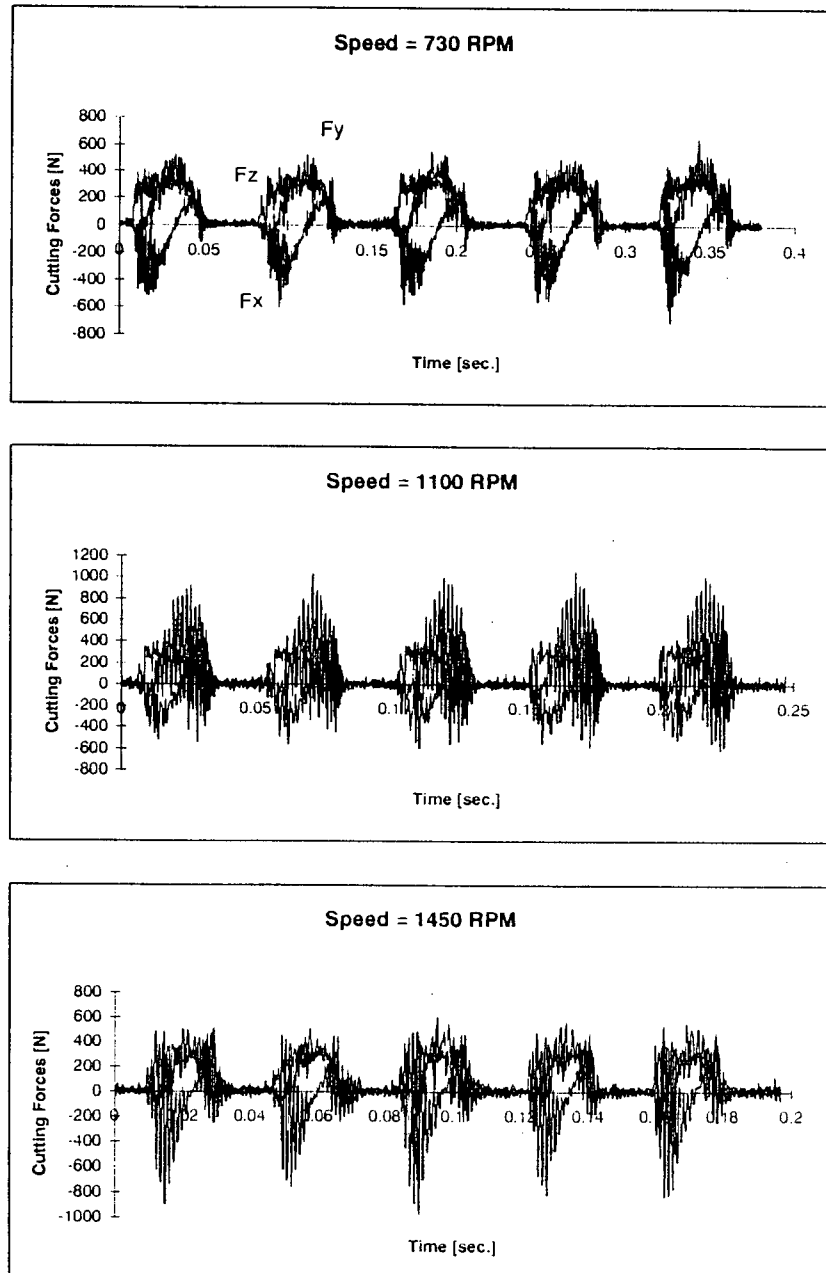
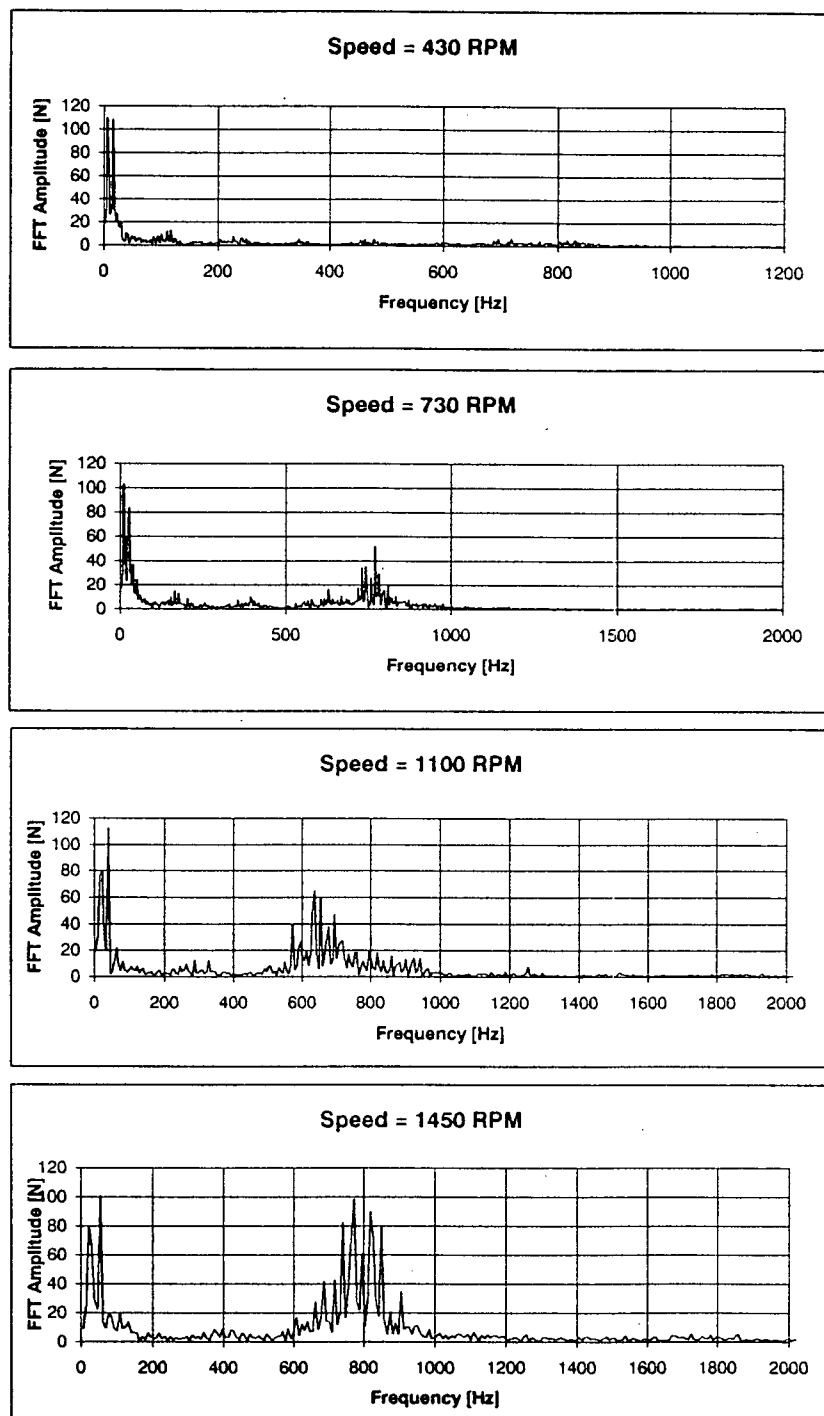


Figure 5.26: Dynamic Ballend Milling Test I, Speed = 730-1450 RPM

Figure 5.27: Fourier Spectrum of F_x from Ballend Milling Test I

contacting and rubbing against finished wavy surface of the workpiece. Analytical modelling of such a contact and rubbing phenomenon has been proven to be difficult [1], and it is usually obtained by comparing the cutting forces or vibrations obtained from time domain simulations and measurements [50]. The analysis of the test results indicated that the damping ratio at the low speed cutting test is 15%, which is approximately four times larger than the measured structural damping ratio of 4%. Consequently 15% and 4% damping ratios were used in the simulations of milling tests at $N=115\text{rev/min}$ and $N=1100\text{rev/min}$, respectively. The agreement between the amplitudes and chatter behavior of the milling tests and simulations is quite reasonable. The Fourier spectrums of the simulated and experimentally measured cutting forces are also provided in figures 5.29 and 5.31. The spectrum of the low speed test is dominated by the average value of the cutting forces (0Hz), and the strength of the force at tooth passing frequency (1.91Hz) and its first harmonic (3.82Hz). Since there are no chatter vibrations, the spectrum is dominated by the static cutting forces generated by the rigid body motion of the milling system. At $N=1100\text{ rev/min}$ however, in addition to the static force components at tooth passing frequency range (18.33Hz), the spectrum indicates the presence of chatter vibrations at 600 to 700 Hz range which corresponds to the structural modes in feed (x) and normal (y) directions. Again, the agreement between the simulation and experimental results are quite satisfactory. The dynamic milling simulation model can be used to prepare stability lobes for the generation of chatter free NC tool paths, as suggested by Weck et al. [49].

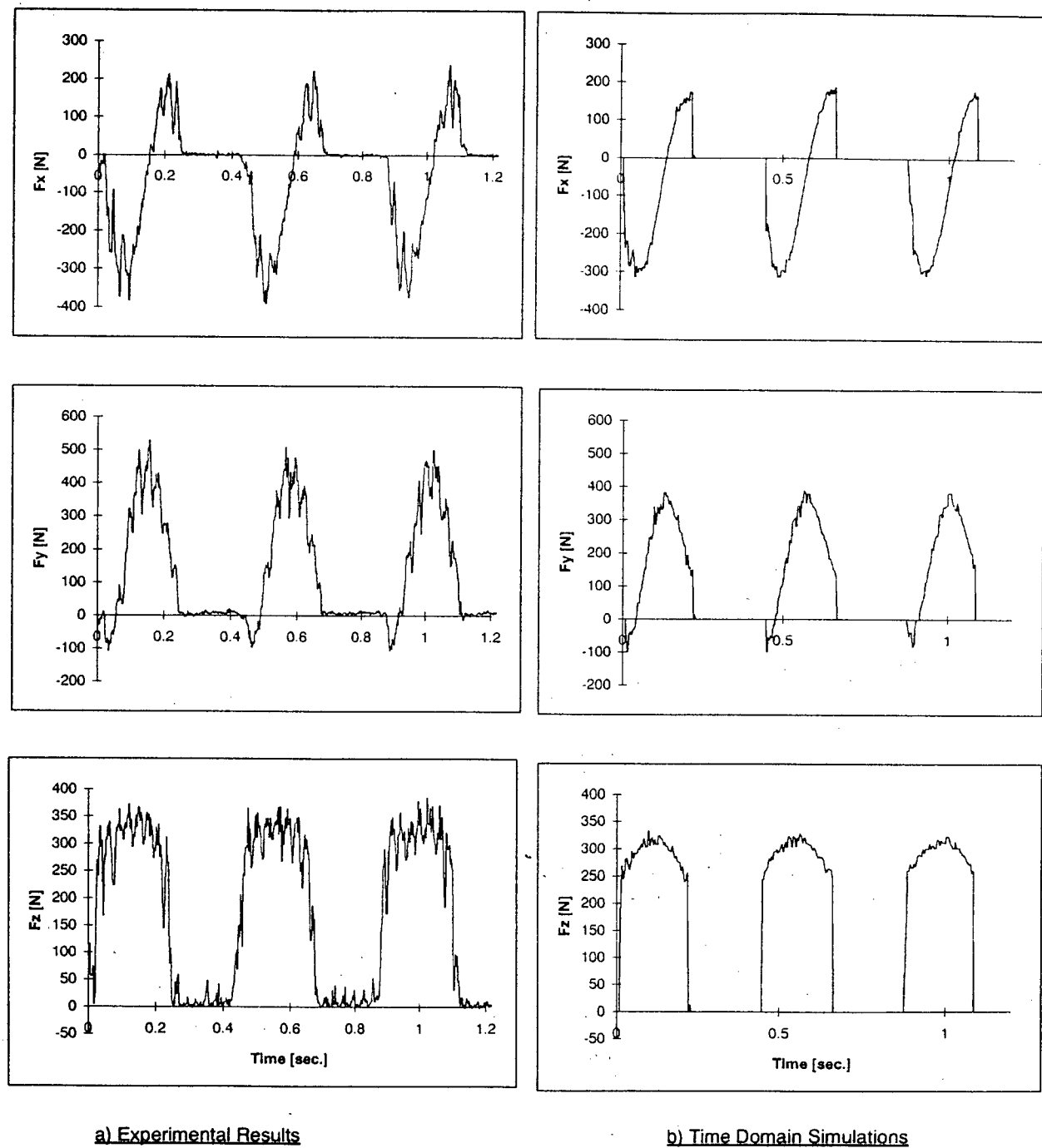


Figure 5.28: Measured and Simulated Cutting Forces, N=115 RPM, Ballend Milling Test I

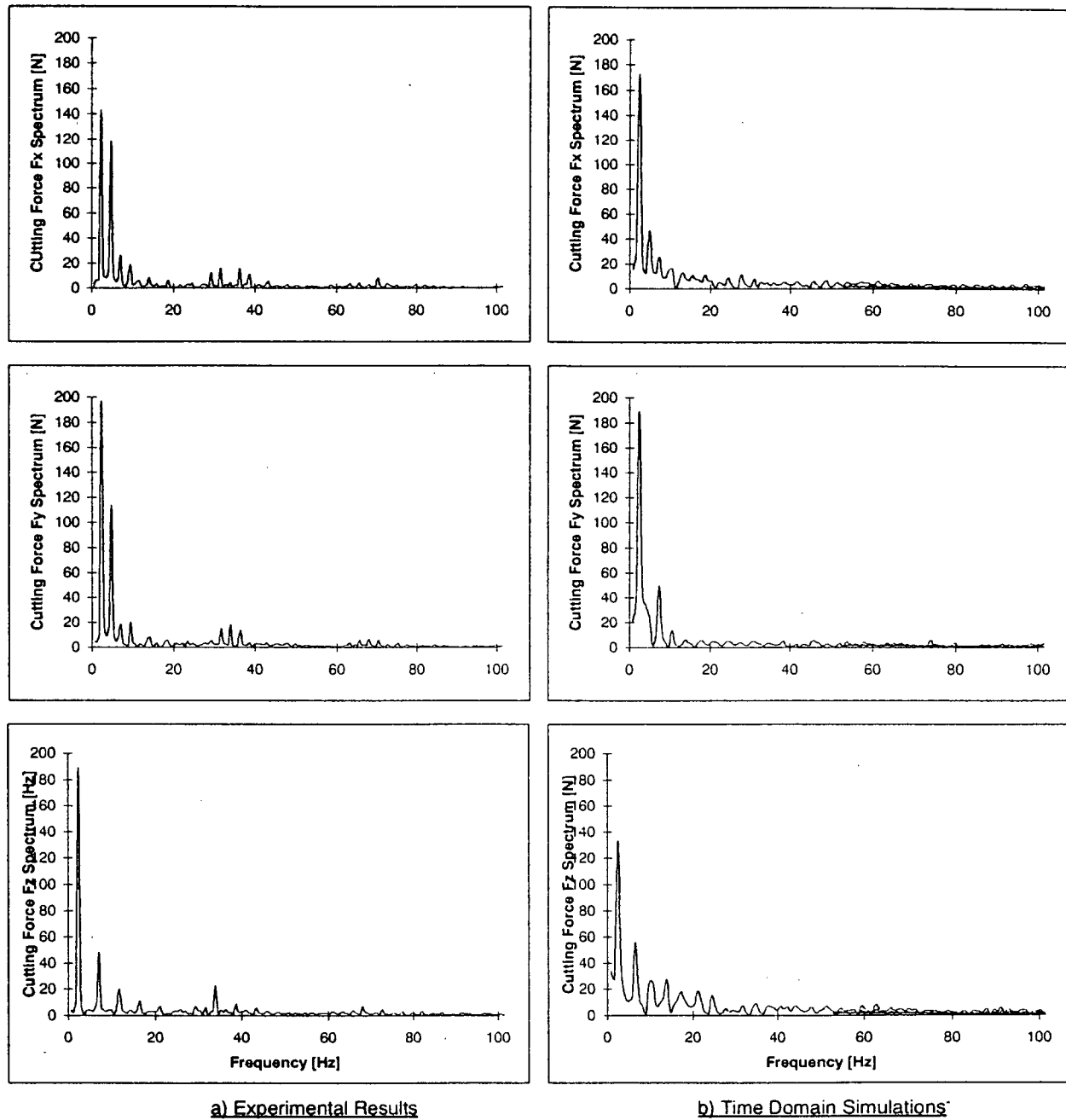


Figure 5.29: Fourier Spectrum from Ballend Milling Test I, N=115 RPM

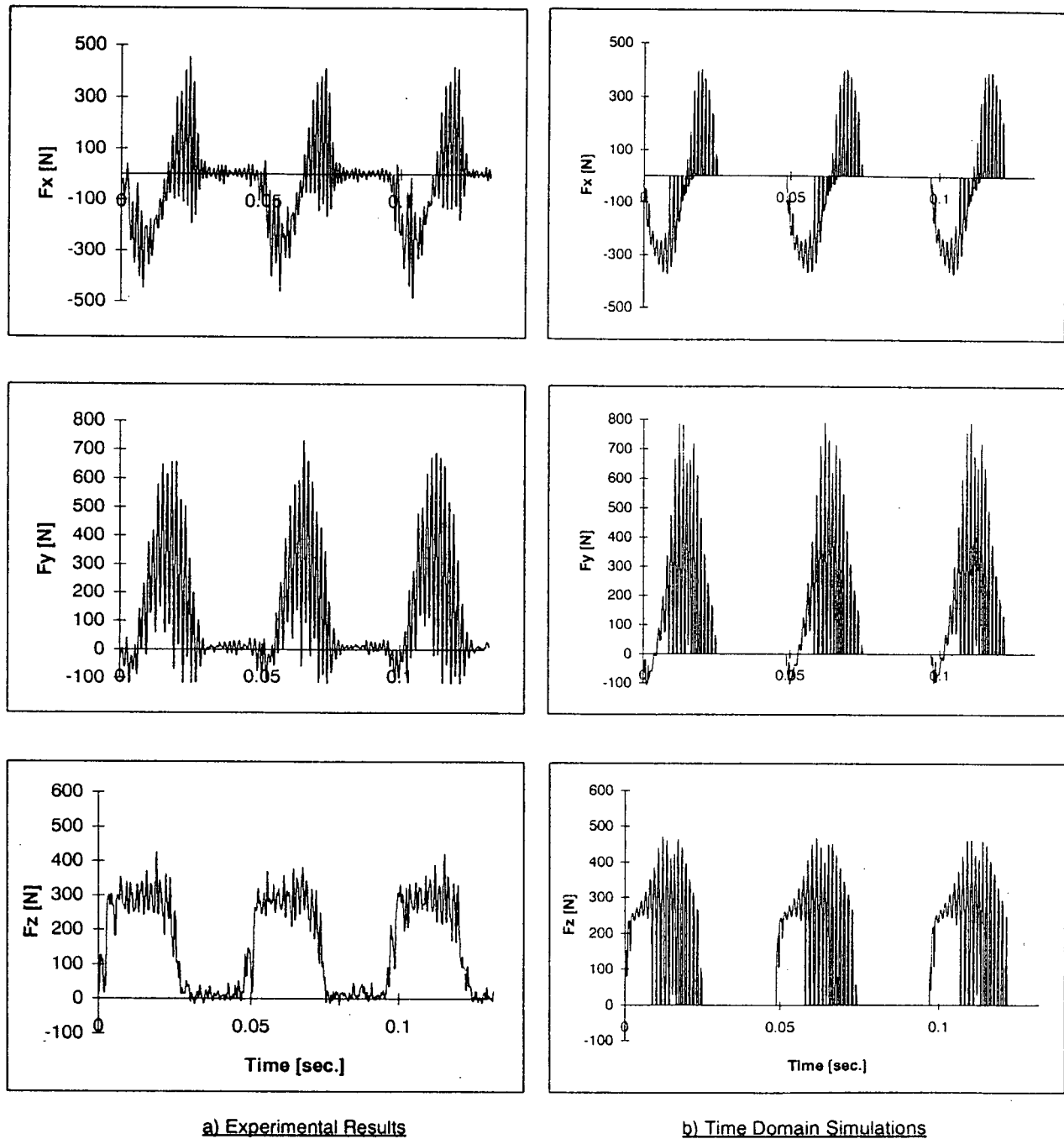


Figure 5.30: Measured and Simulated Cutting Forces, $N=1000$ RPM, Ballend Milling Test I

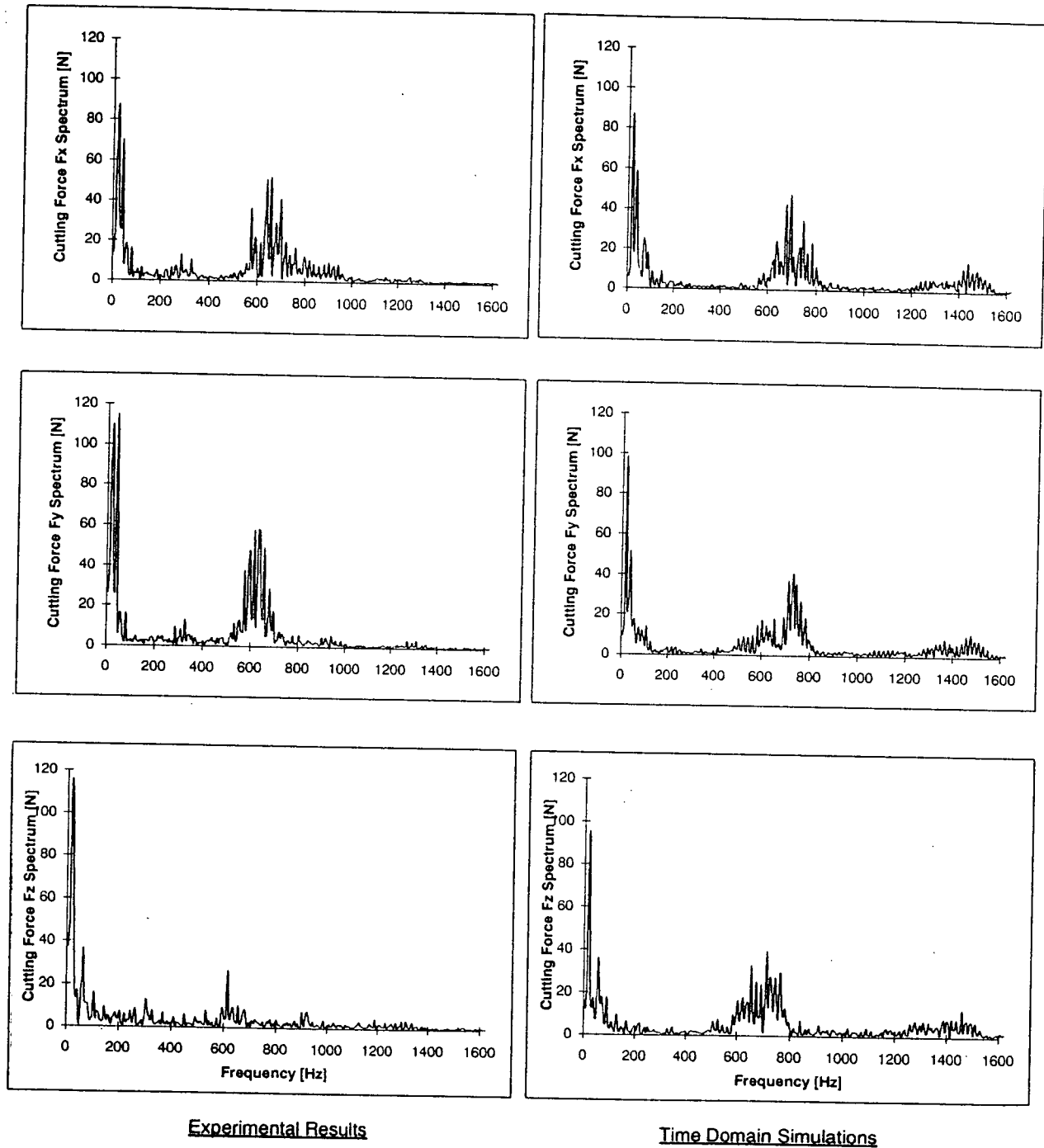
Figure 5.31: Fourier Spectrum from Ballend Milling Test I, $N=1100$ RPM

Table 5.1: Time Domain Simulation Conditions for Dynamic Ball End Milling Tests I

Workpiece material	Titanium Ti_6AlV_4
Milling mode	Slotting
Spindle speeds (N)	Test 1: 115 - 1100 [rev/min]
Feed rate (s_t)	0.0508 mm/tooth
Axial depth (a)	2.54 mm
Cutter material	Solid carbide
Ball radius (R_0)	9.525 mm
Rake angle (α_n)	0 degree
Helix angle (i_0)	30 degree
Number of flutes	1

Dynamic Test and Simulation II

The stability method is applied to a practical ballend milling operation. Experiments were conducted on a FADAL CNC machining center. The milling system under consideration is similar to the one shown in Figure 5.3. It is represented by a single degree-of-freedom system with the following parameters identified from impact test (see Figure 5.32):

$$\begin{aligned} k_x &= 5725 \text{ N/mm} & \xi_x &= 0.04 & \omega_x &= 1150 \text{ Hz} \\ k_y &= 5740 \text{ N/mm} & \xi_y &= 0.05 & \omega_y &= 880 \text{ Hz} \end{aligned} \quad (5.31)$$

Table 5.2: Cutting Conditions for Dynamic Ball End Milling Tests II

Workpiece material	Titanium Ti_6AlV_4
Milling mode	Half immersion Upmilling
Spindle speeds (N)	1000 - 6000 [rev/min] in 1000 RPM steps
Feed rate (s_t)	0.0508 mm/tooth
Width of cut (w)	6.35 mm (fixed)
Axial depth (a)	Variable
Cutter material	Solid carbide
Ball radius (R_0)	6.35 mm
Rake angle (α_n)	0 degree
Helix angle (i_0)	30 degree
Number of flutes	1

A single fluted ballend cutter was used in an up milling operation with Titanium alloy workpiece, which is assumed to remain rigid in all simulations. A range of spindle speeds and axial depth of cuts were selected and the measured cutting forces of two particular cases are showed in figures 5.33 and 5.34. At each spindle speed, all the cutting conditions (see table 5.2) except the axial depth of cut are kept constant. Increasing increments of axial depth of cut a are taken until the point of chatter onset occurs. Then the procedure is repeated for a new spindle speed. Chatter onset was determined by

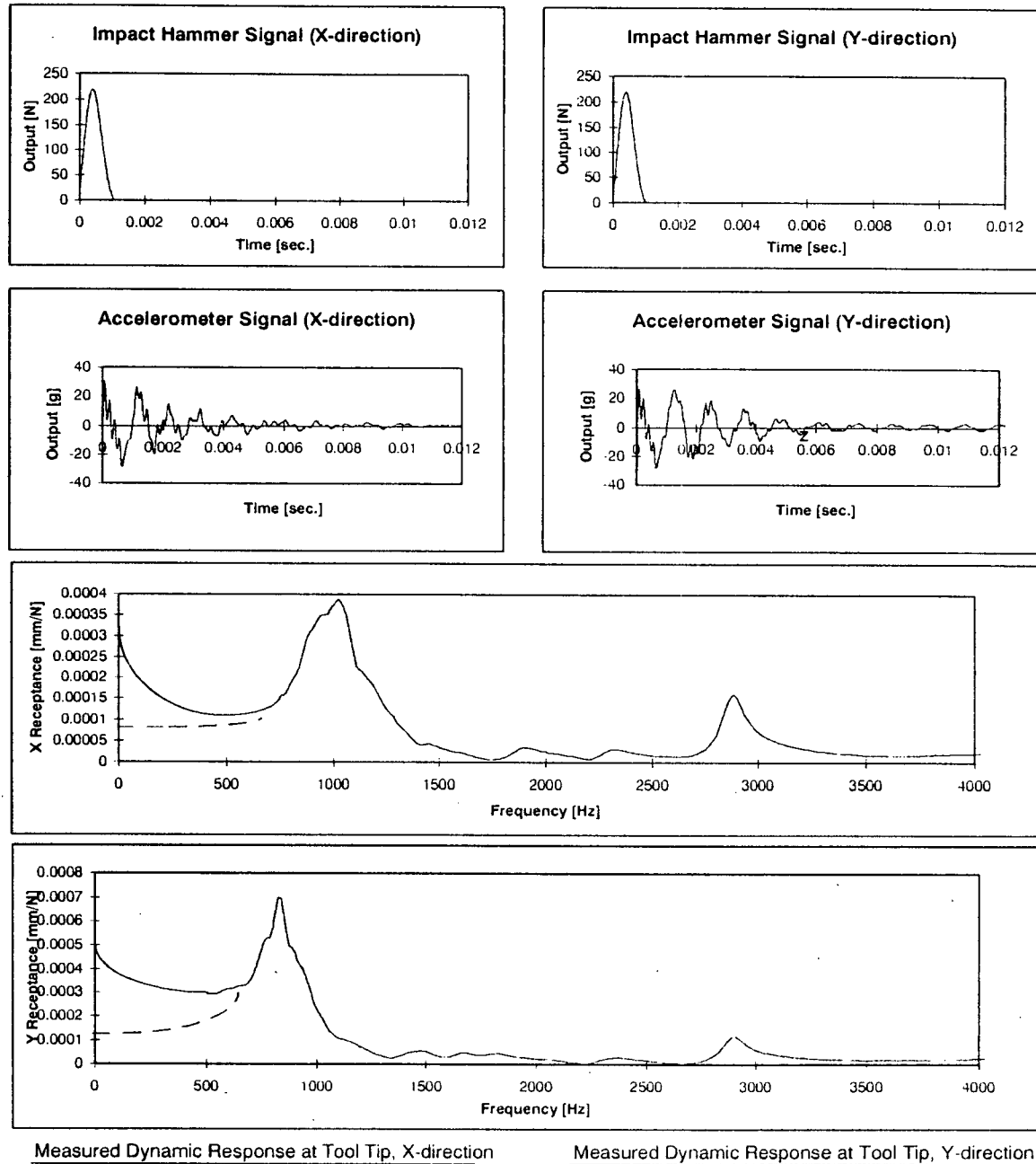
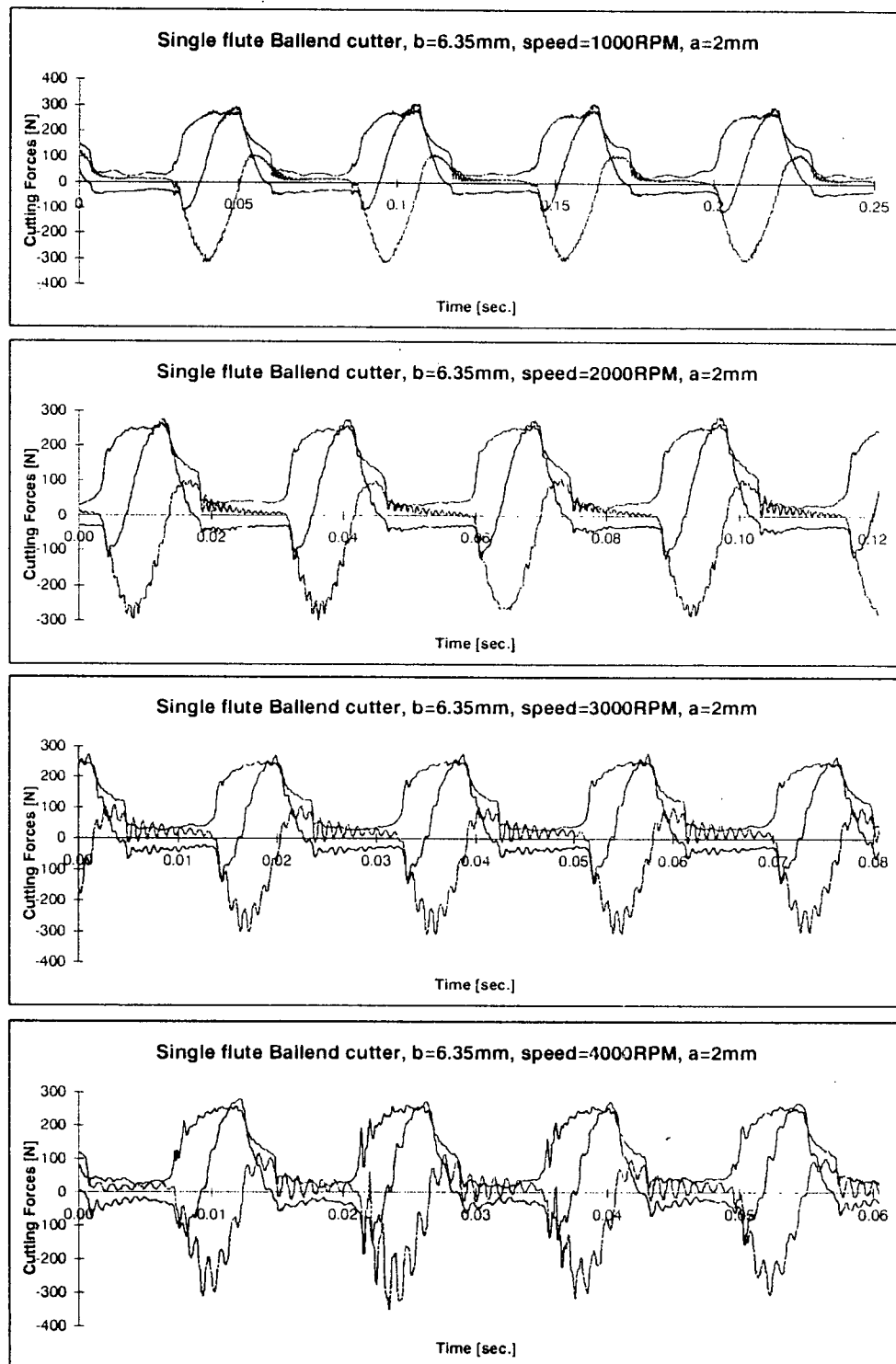
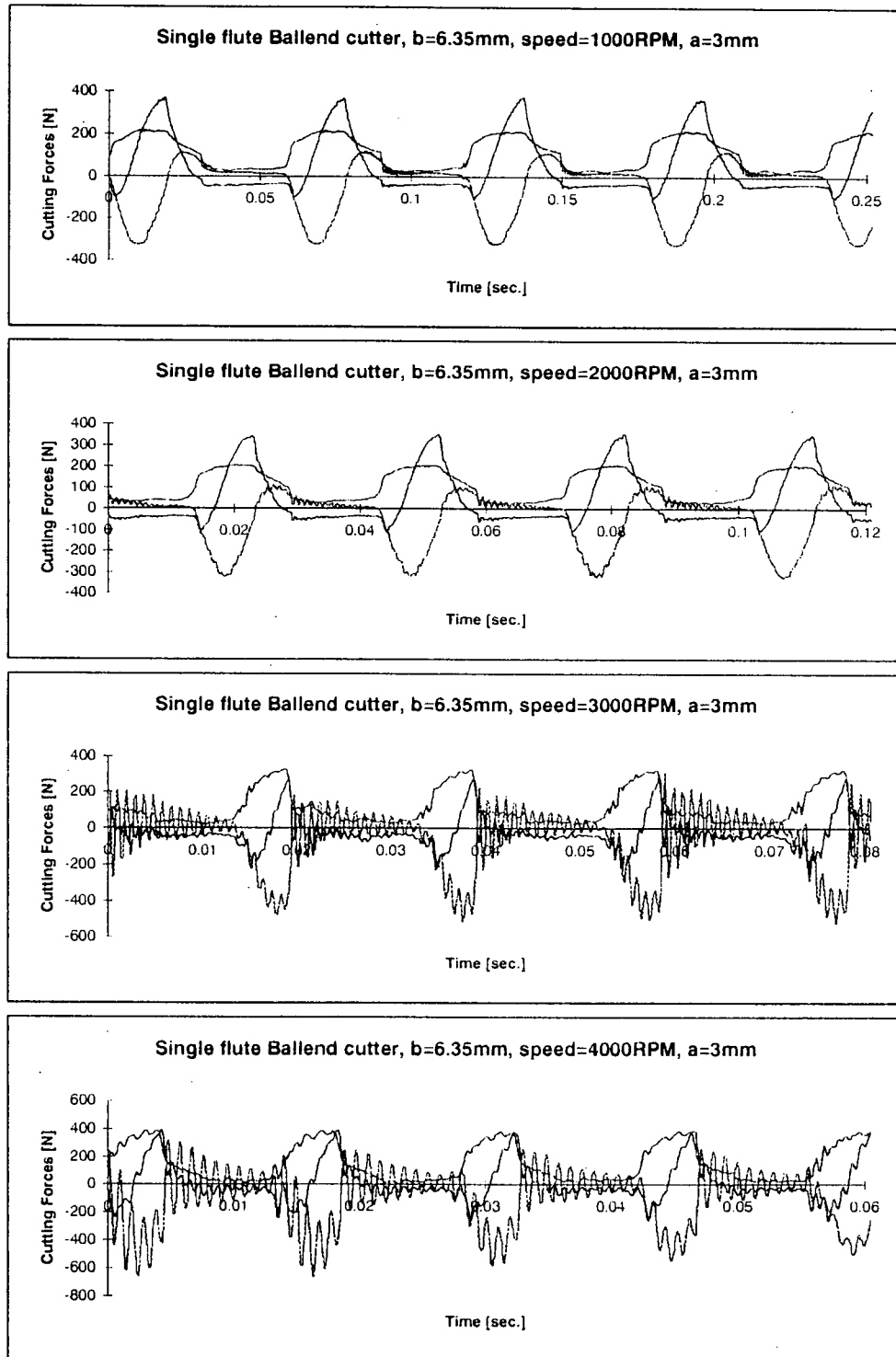


Figure 5.32: Transfer Function Measured at tool tip. Ballend Test II

Figure 5.33: Ballend Milling Experiments II, $a = 2\text{mm}$

Figure 5.34: Ballend Milling Experiments II, $a = 3\text{mm}$

observing the output of the cutting forces, as well as the sound pressure recorded by the microphone. The audible sound associated with high amplitude oscillation can be used as a further check of an unstable machining operation. It should be noted that, due to the extremely high strength property of *Ti6AL4V*, difficulties were experienced especially during those tests at high cutting speeds (above 4000RPM or 160 m/min). During high speed machining, the cutting tool deteriorates and wears out very fast, which may introduce inconsistency and inaccuracy into the data collected. Therefore, each tool was monitored closely throughout the tests to report any significant tool wear problem, a small chip load was chosen in all the tests to prolong tool life, and replacement of tools was done after every 20-30 tests, depending on the cutting conditions and the condition of that particular tool.

The experimental results are presented in a way similar to Wecks' (Figure 5.9) in Figure 5.36 where the classical stability chart obtained from the experiments is plotted, on top of the simulation results. Fine step size was chosen in the simulations: the minimum step size of the axial depth of cut was 0.0125mm and the spindle speeds were run from 1000 to 5000RPM in 100RPM steps. For the 1mm axial depth of cut experiments, all the tests and simulations showed no significant vibrations and cutting force fluctuations, implying stable cutting was achieved. As the depth of cut increases, the onset of chatter was recognized and recorded, as indicated in the chart. At the same time, the simulation program searches for the limit of stability by applying the PTP algorithm given above. For example, both the measured and simulated PTP forces in the feed direction are plotted in Figure 5.35 for three different axial depth of cuts. From the experiments, chatter was noticeable at a few spindle speeds ($N = 3000, 4000, 5000RPM$) when $a = 3mm$. A further examination of Figure 5.35 reveals that at the limit of stability, the PTP forces have jumped significantly (more than 150 percents) with a 50 percent increase in the depth of cut, as noted by Thusty [23]. Although force vibrations will

always present in the process, it does not significantly influence the DC component of the cutting forces, as the waves (resulting from force vibrations) left on the surface are repeating at the tooth passing frequency, thus making “the chip thickness independent of the amplitude of the forced vibration” [33] as long as the cut is stable. From Figure 5.35, it can be seen that the process becomes unstable at $N = 3000 \text{ RPM}$ and $a = 3 \text{ mm}$ in which there is a substantial jump in the cutting forces.

Although the agreement between the chatter behavior of the milling tests and simulations is quite reasonable, the simulated stability lobes are all “squeezed” and “packed” together and have a rather flat shape especially at low cutting speeds, which deserves some further explanation. Firstly, the simulation model predicts a lower stability limit especially at low speeds because it doesn’t take into account the effect of process damping. Furthermore, due to the high chatter frequency to tooth passing frequency ratio ($f_c/N * N_f$) at low speeds, there are numerous number of vibration waves left on the surface, which requires an extremely high sampling frequency to capture the “regeneration of waviness” mechanism (vibration waves left on surface). In the simulation, the sampling frequency was chosen as 35 times the natural frequency of the system and the predictions appeared to be more stable. The third reason can be explained by the chip thinning effect which is a unique characteristic in ballend milling. At low axial depth of cut, the stiffness of the system is high due to the increased cutting pressures at small chip thickness.

The immersion condition also influences the stability lobe prediction. Two different cutting modes are shown in Figure 5.39. Figure 5.39a shows the cutting geometry used in the ballend experiments II and in the stability simulation. The width of cut is constant ($w = 6.35 \text{ mm}$). A close examination of the wave regeneration mechanism along the axial direction reveals that, due to the changing immersion angle, the number of vibration waves left on the surface changes along the axial direction. There is no longer a constant

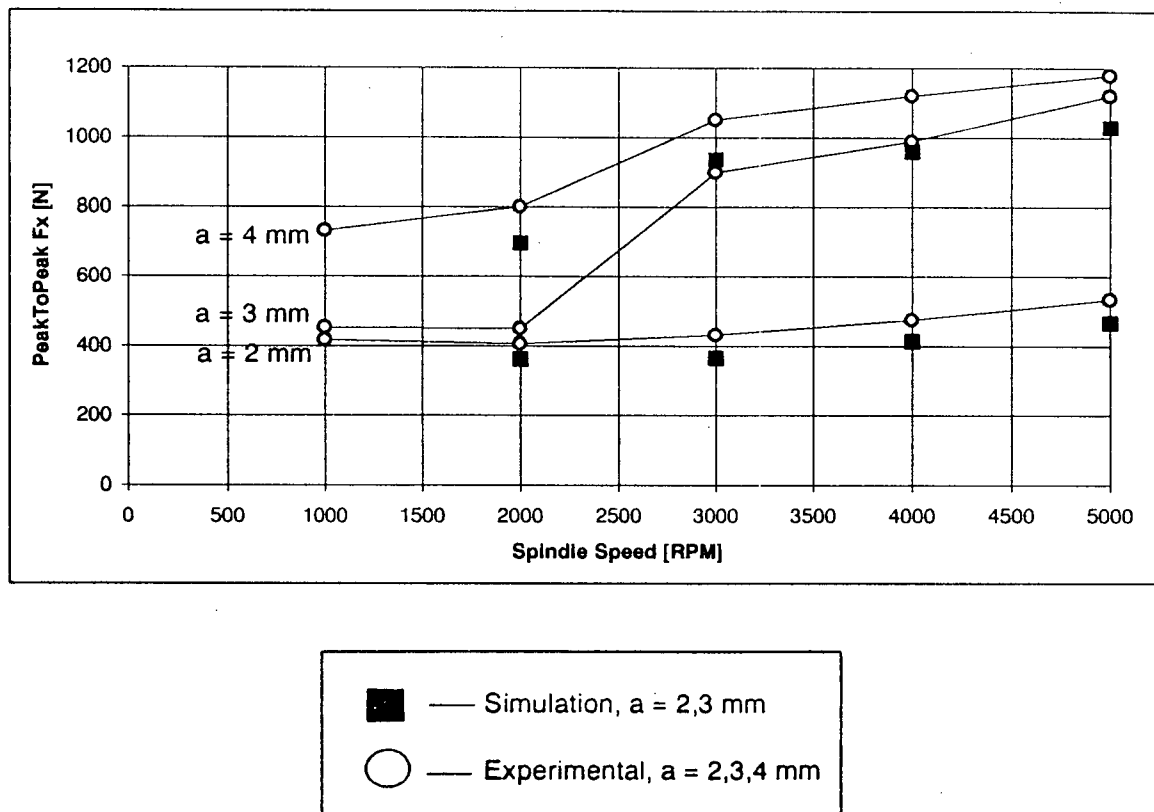


Figure 5.35: Experimental and Simulated PTP results. Ballend Milling Test II

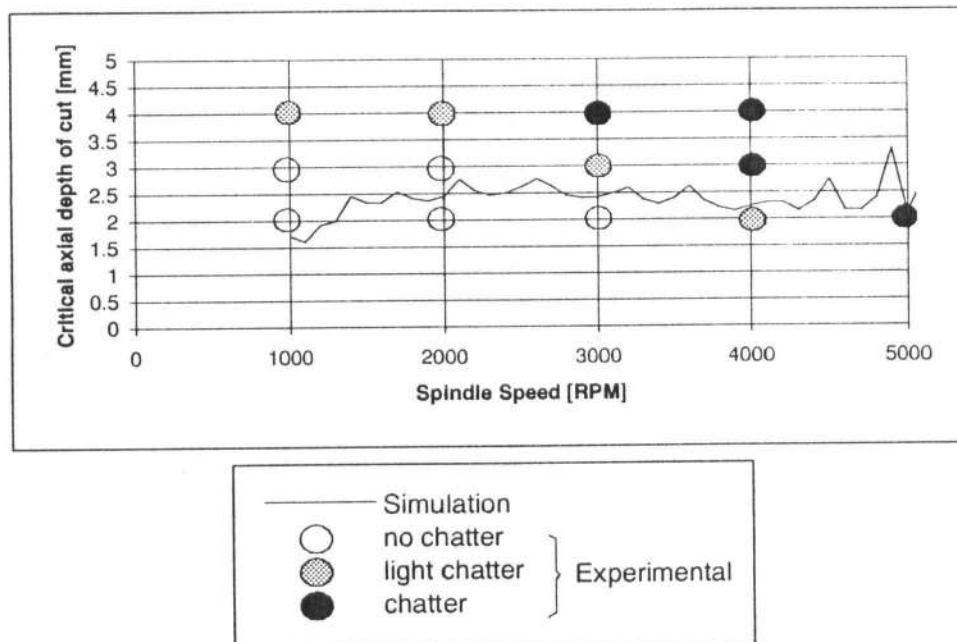


Figure 5.36: Simulated Stability Lobe Diagram for Ballend milling Test II

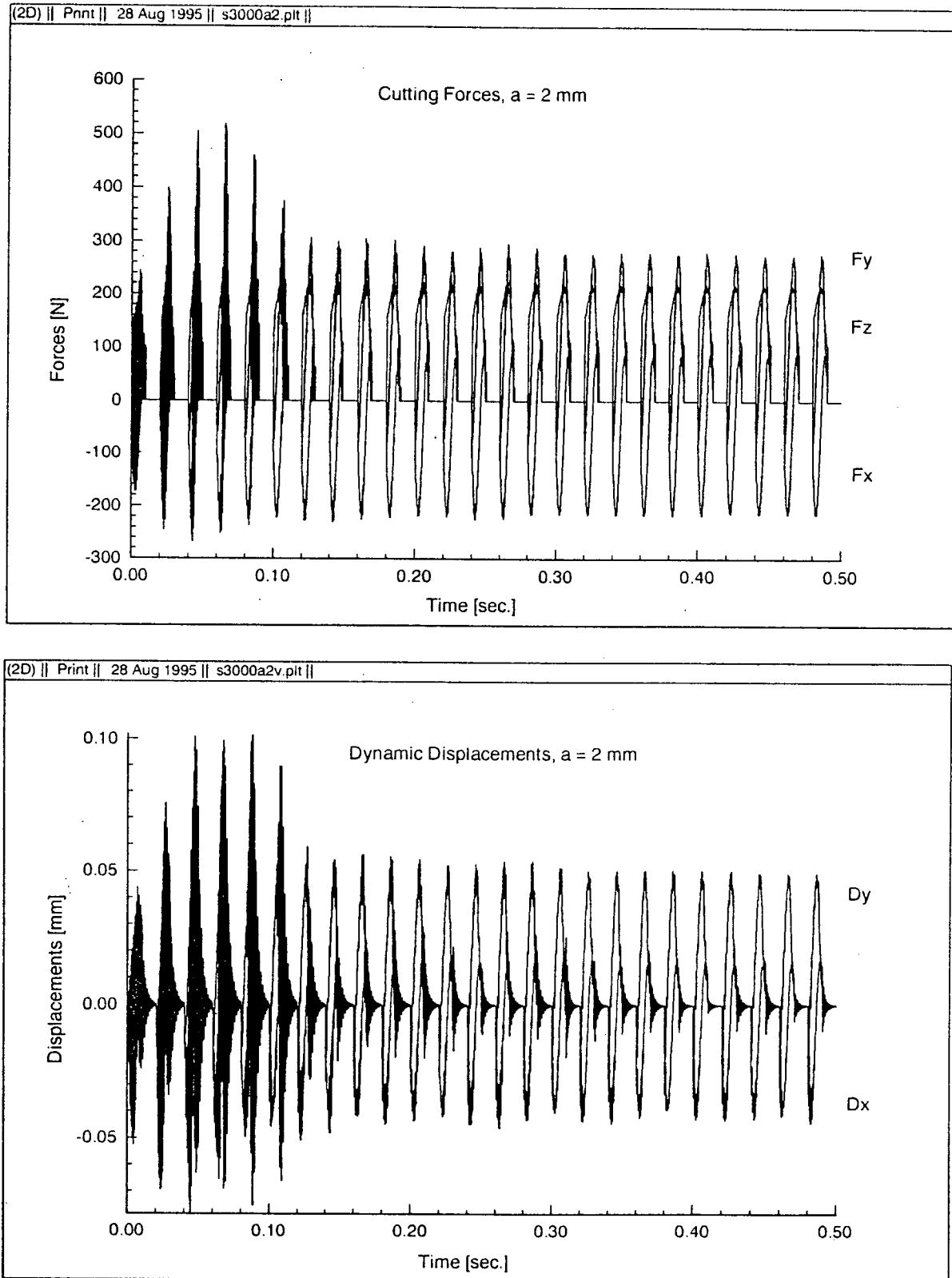


Figure 5.37: Simulated Cutting Forces and Vibrations. Ballend Milling Test II

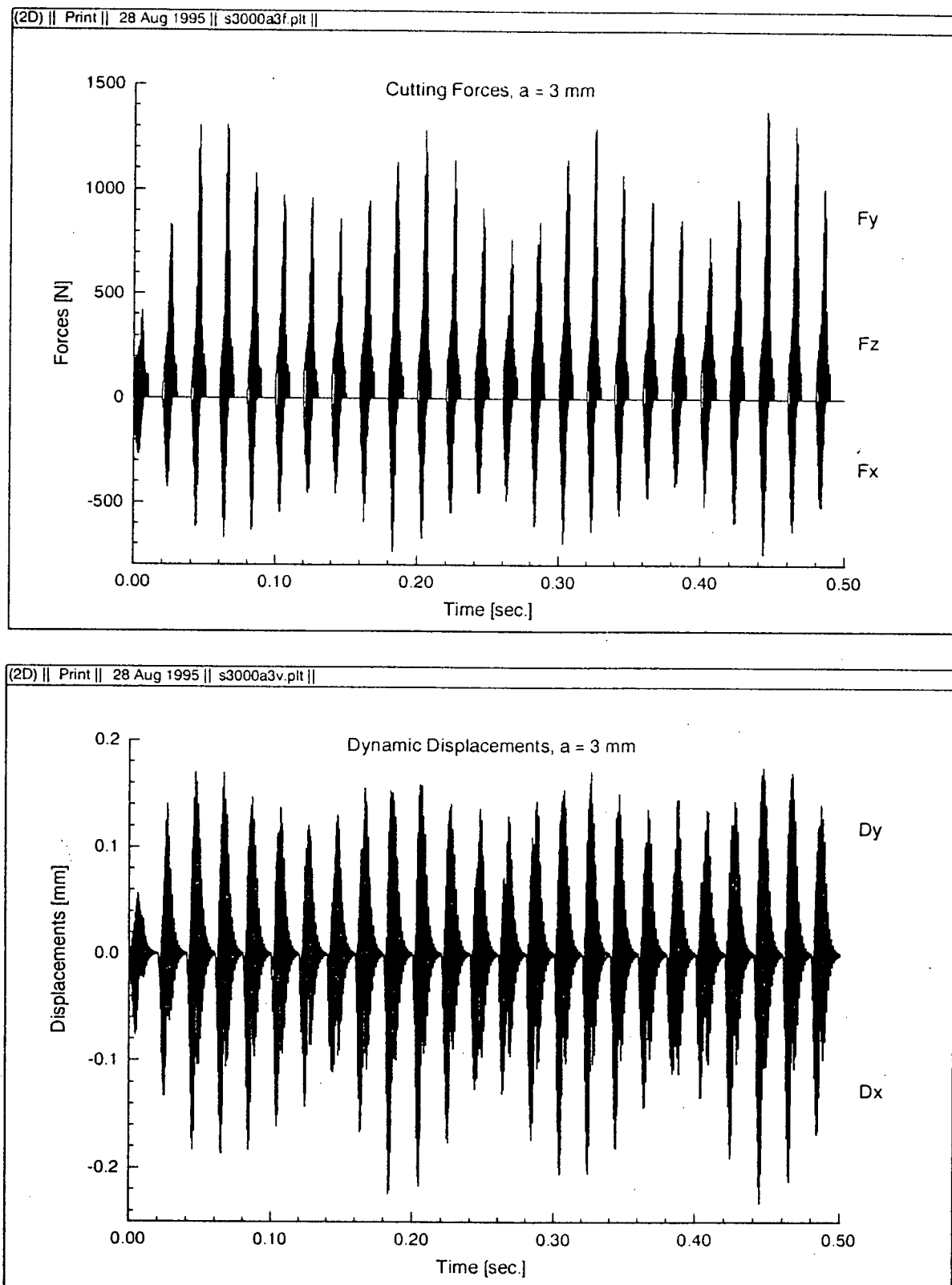


Figure 5.38: Simulated Cutting Forces and Vibrations. Ballend Milling Test II

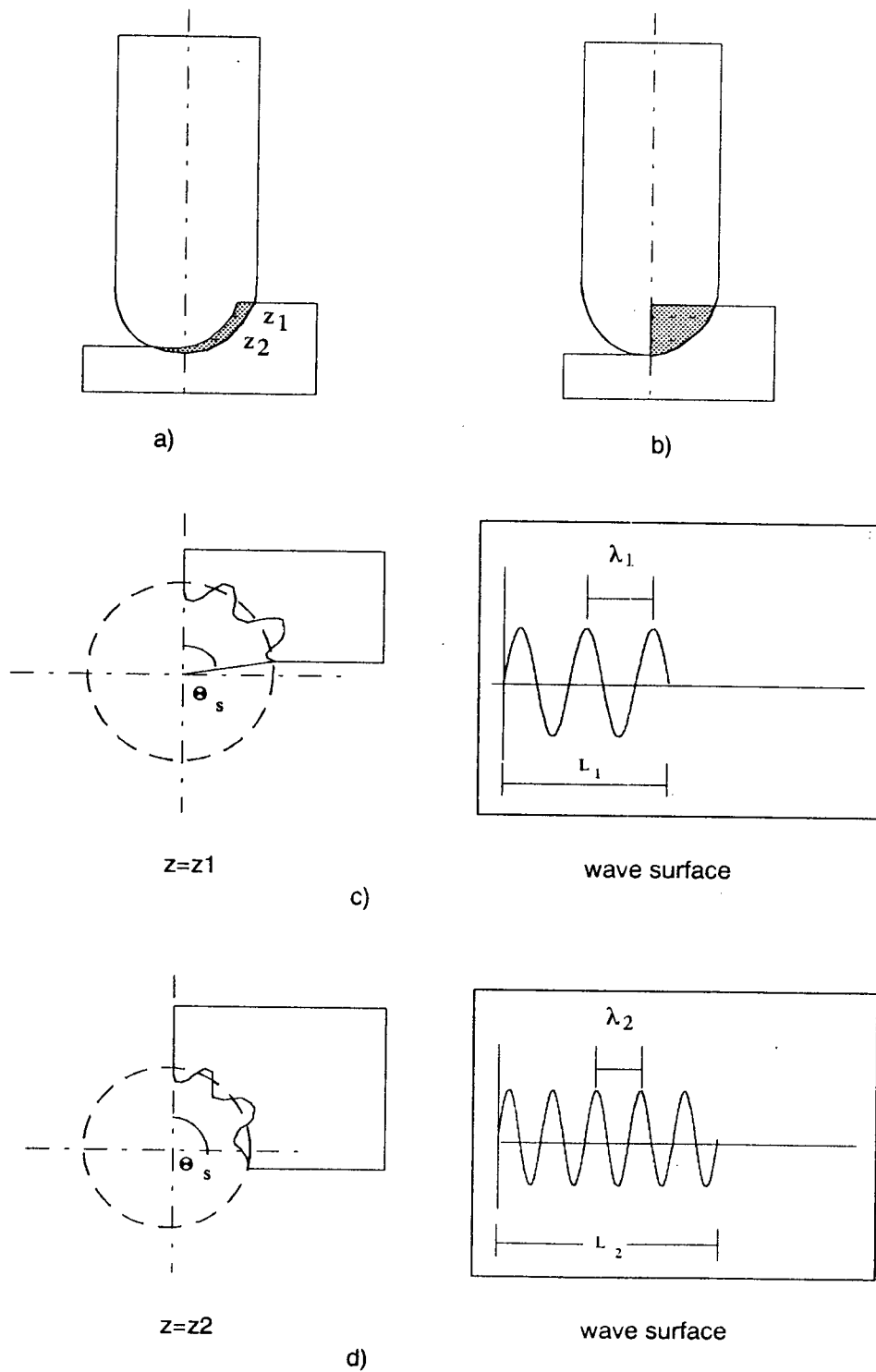


Figure 5.39: Wave generation on different cutting geometries. Ballend Milling

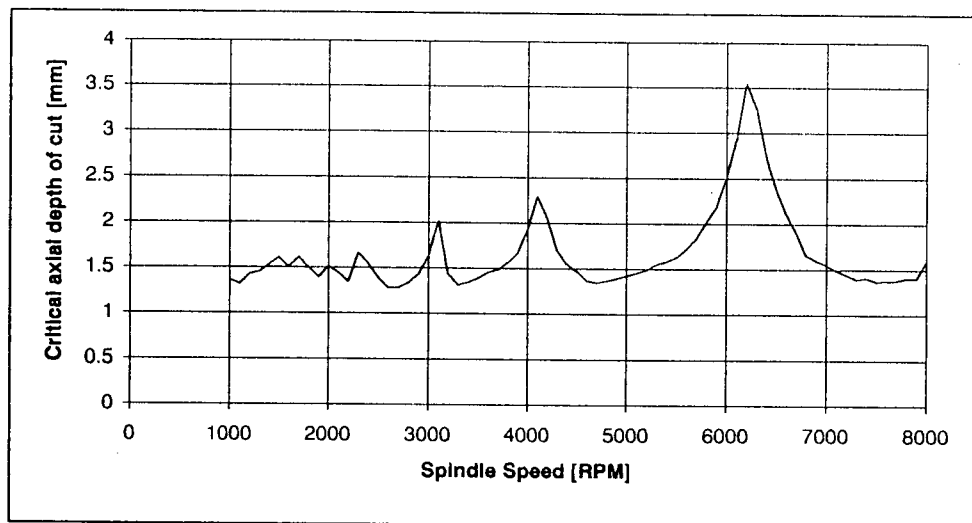


Figure 5.40: Simulated Stability Lobe Diagram for Ballend milling III

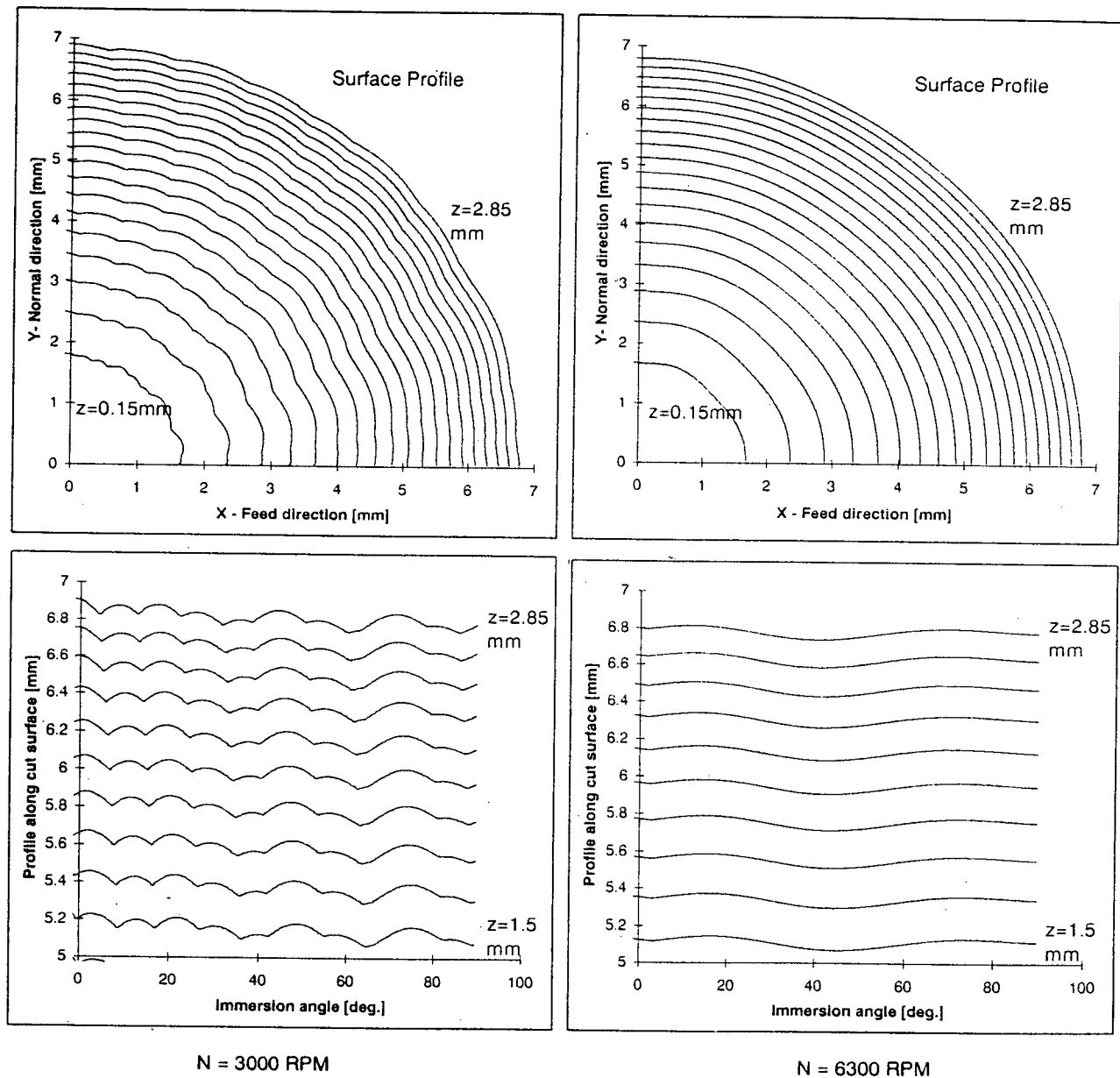


Figure 5.41: Simulations showing the waviness on cut surface at different cutting speeds

integral number of waves along the axial direction. Depending on the cutting conditions, the stability of the process may change substantially, especially at low speeds, when the process damping is high due to shorter wave length cycles.

On the other hand, if the radial immersion angle is constant (i.e. variable width of cut), as shown in Figure 5.39b, there is always an identical number of vibration waves left on the surface along the axial direction. This phenomena is tested in a half immersion ballend upmilling simulation, in which $R_0 = 9.525mm$, $k_x = 19300N/mm$, $k_y = 14200N/mm$. Other cutting conditions are the same as in the second simulation. Figure 5.40 shows the simulated stability lobes. The influence of spindle speed is demonstrated by examining the simulated results at $N = 3000RPM$ and $N = 6300RPM$. At $N = 3000RPM$, the integral number of waves imprinted on the surface per tooth spacing is, according to Eq. 5.18, $N_w = 4$. (see Figure 5.41a) The self excitation mechanism takes place and resulting in unstable process. While keeping other conditions constant except for a higher spindle speed ($N = 6300RPM$), as shown in diagram 5.41b, the number of waves between each teeth is lower, i.e., $N_w = 2$ and both the cutting forces and the tool vibrations reduce significantly. This change in spindle speeds has a significant impact on the stability of the process, which are reflected in Figures 5.42, 5.43, 5.44, and 5.45.² The resultant cutting forces, vibrations, and surface finish demonstrate clearly the advantages of regulating under a stable machining condition using the stability chart developed.

²The curvature of the surface is filtered out for better visualization

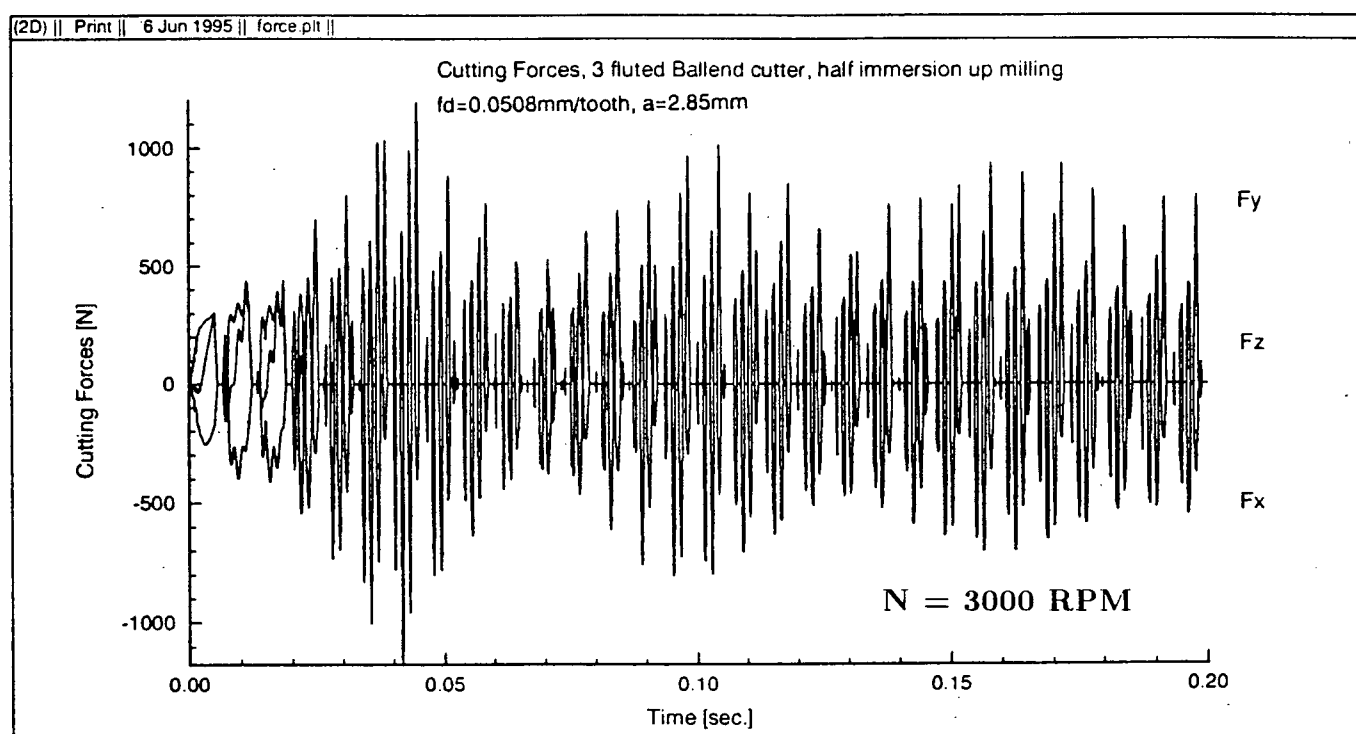
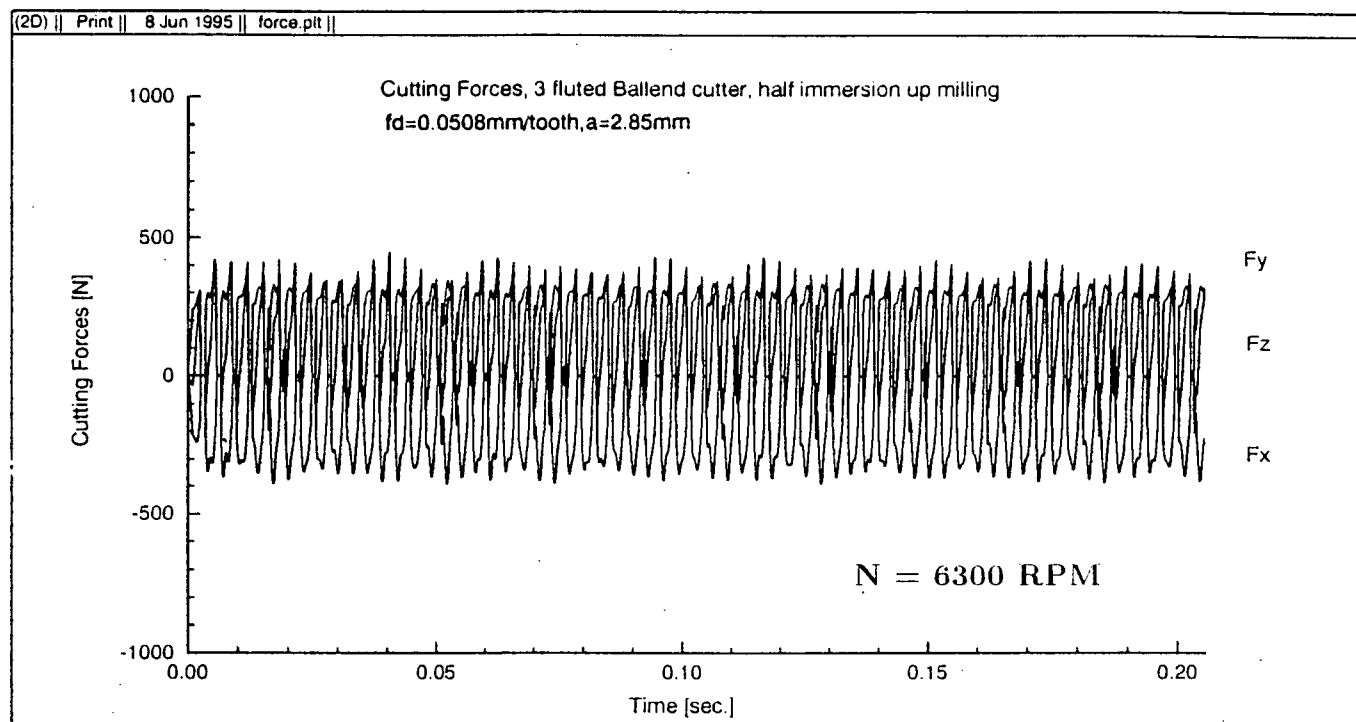


Figure 5.42: Simulations of cutting forces at 2 different speeds, Ballend milling

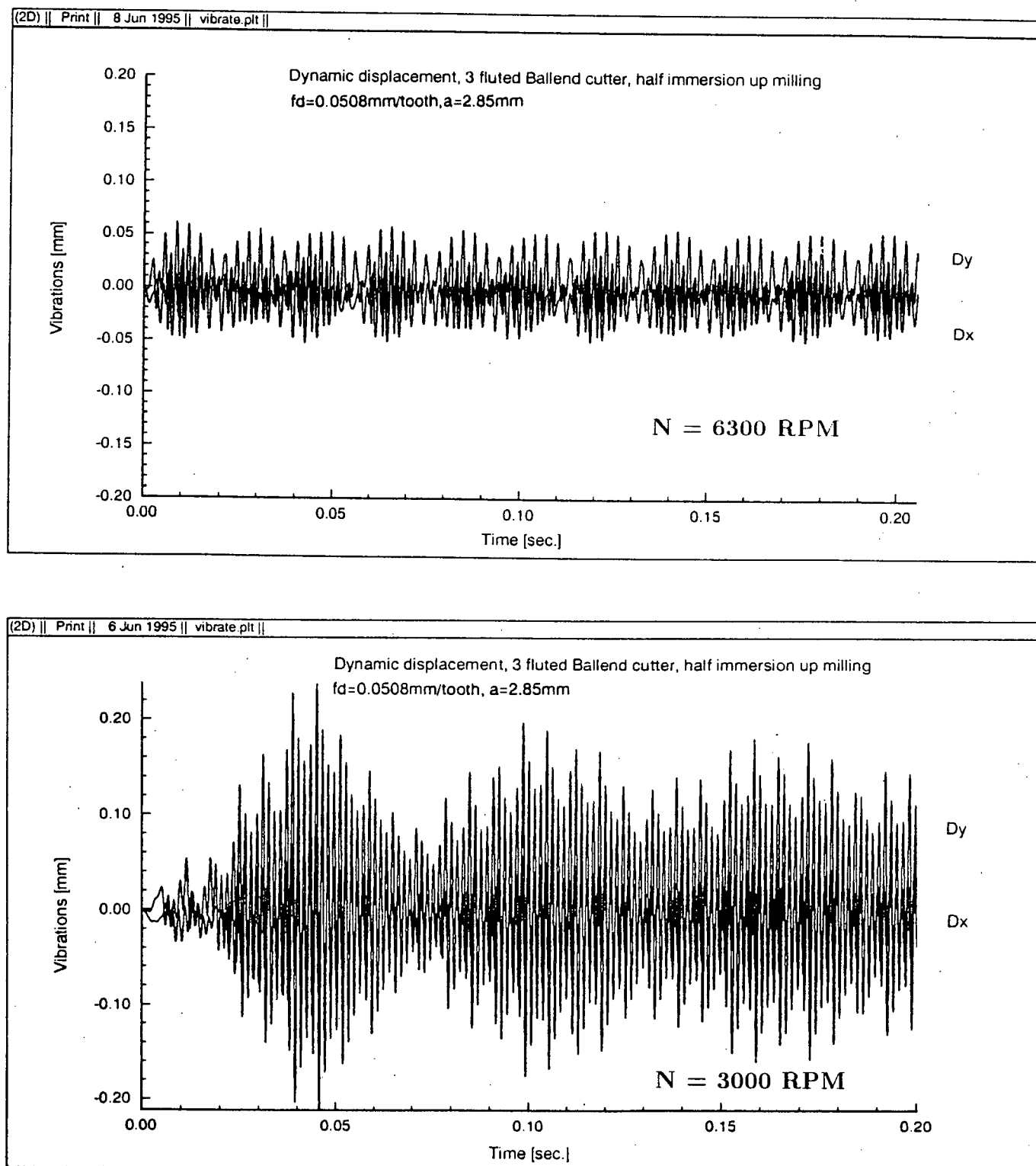


Figure 5.43: Simulations of vibrations at 2 different speeds, Ballend milling

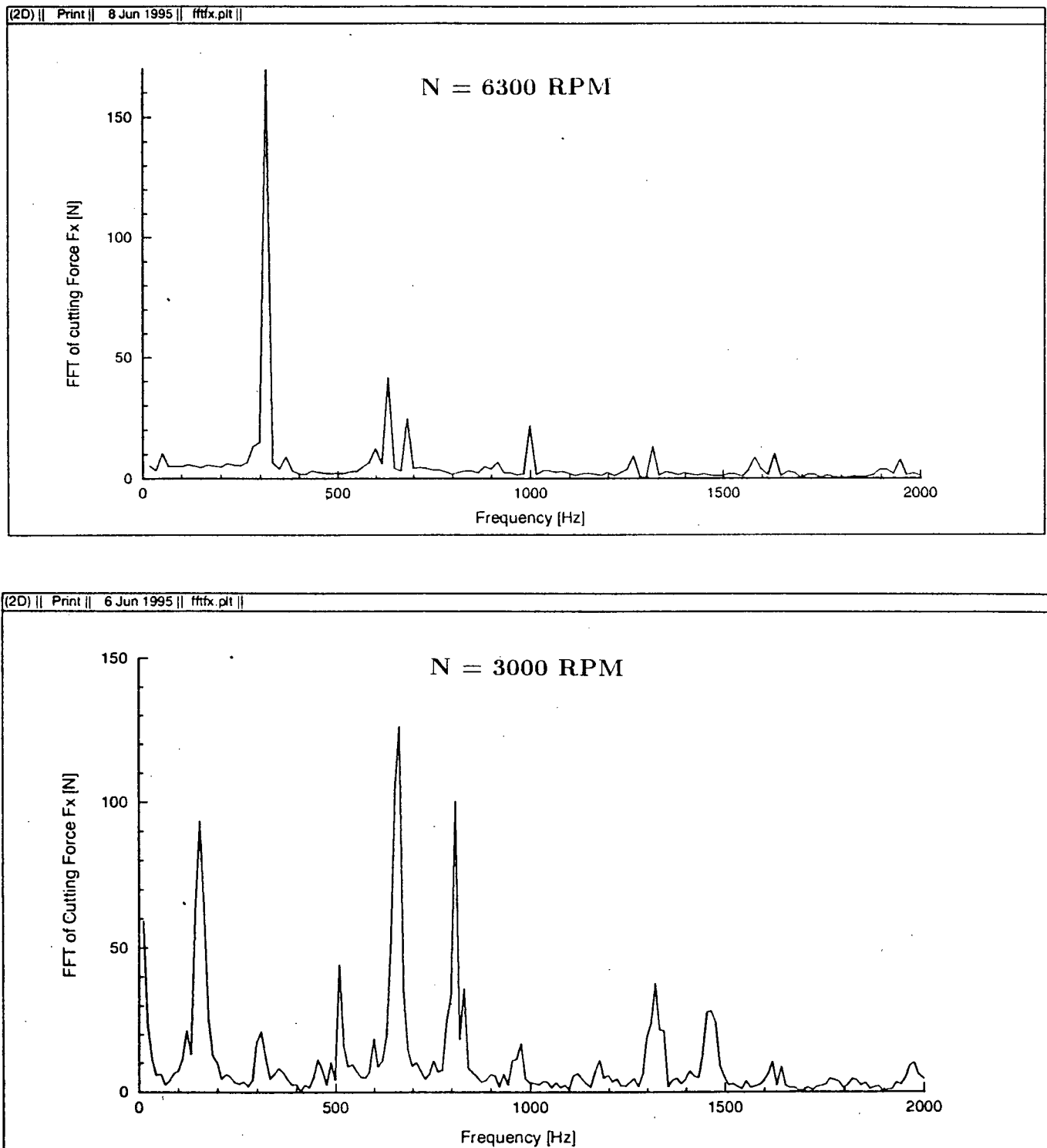


Figure 5.44: FFT of the simulated cutting forces at different speeds, Ballend milling

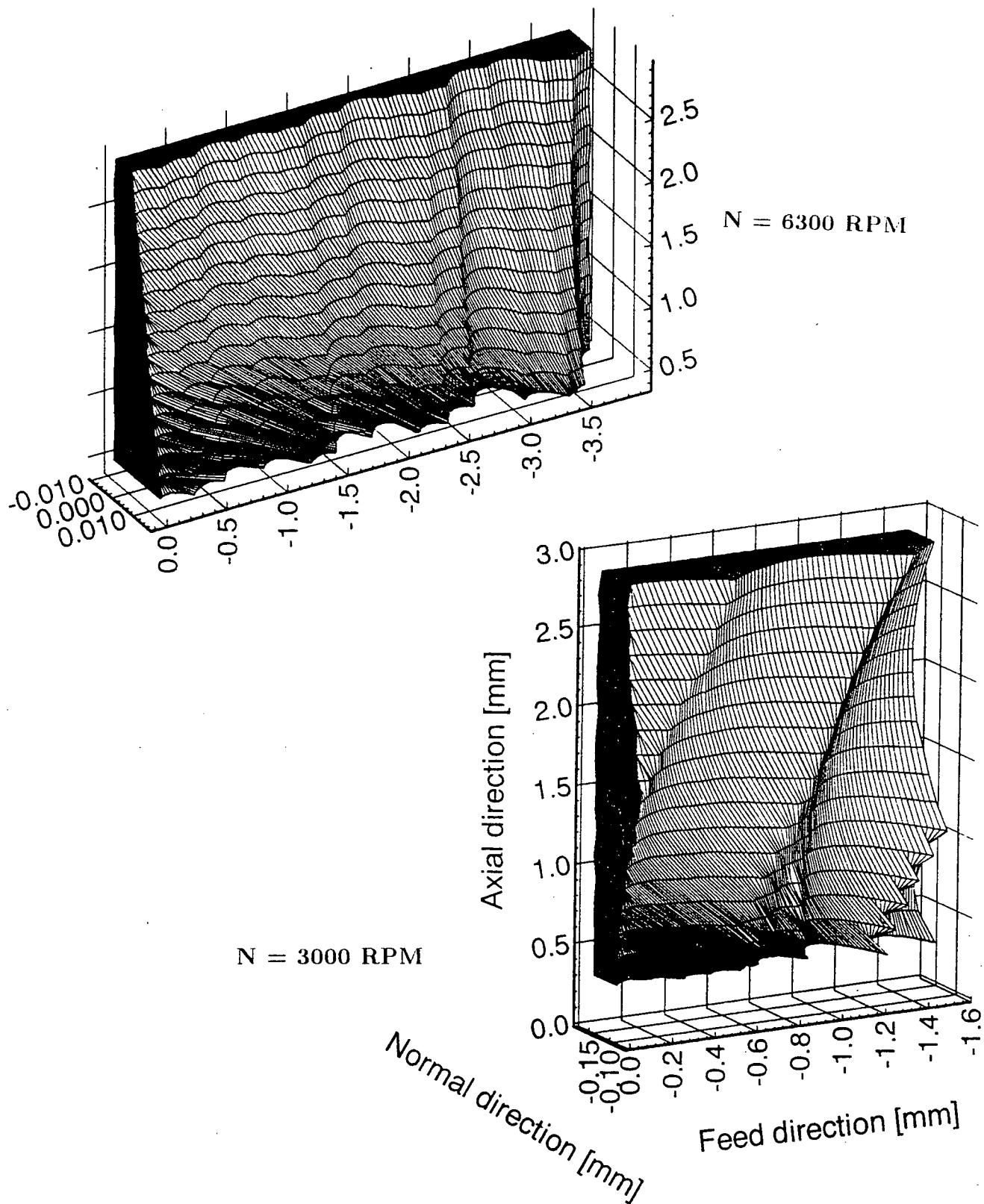


Figure 5.45: Simulations of finished surfaces at different speeds, Ballend milling

5.4.3 Summary

This chapter presented a general milling model in which both the cutter and the generation of cut surface by the true kinematics of milling system were accurately modelled. Simulations and experimental verifications showed that, the combined model is capable of predicting the cutting forces and generated surface finish with or without the presence of chatter vibrations during ball end milling operations.

The model has several advantages:

- When the vibrations are neglected, the static milling can be simulated.
- The finish surface is predicted by keeping the points which have zero immersion, $\Psi = 0$. The finish surface generated represents feed marks, static form errors or chatter vibration errors depending on whether rigid, statically or dynamically flexible milling system structure is assumed, respectively.
- In chatter analysis, the resulting chip thickness $h(t)$ represents the true regenerated value. There is no need for iterative evaluation of multiple tooth periods to find the true chip load [51].
- The nonlinearity in the chatter, i.e. the tool jumping out of cut, is accounted for by imposing the condition : *if $h(t) < 0$ then $h(t) = 0$.*
- Cutter runout and flank face/cut surface interference(i.e. process damping) can be included in the model easily.

5.5 Conclusions

Both static and dynamic milling with two different cutters have been examined in this chapter by simulation and experimental studies. Chatter stability was experimentally examined, though in a rather low speed range. However, the trends from simulations suggested that highly realistic results could be obtained if a more accurate experimental procedure is implemented, in which the predicted stability lobe diagram can be fully utilized.

Conclusions

The objective of the thesis has been to develop methods and algorithms to understand and predict the behavior of milling operations. Special emphasis has been placed on the ball end milling operations which are widely used in machining dies, molds, and hydrodynamic and aerospace parts with sculptured surfaces. The results of this study provide prediction of cutting power and torque required from the machine tool; the direction, amplitude and density of cutting forces applied on the cutter and workpiece structures; static and dynamic deformation errors left on the finish surface; chatter vibration free stable cutting conditions. The prediction of milling performance is used to plan ball end milling operations in industry.

First, geometric models of helical, bull nose and ball end cutters are developed in Cartesian coordinates. For a given cutter diameter, radial rake angle, helix angle, the number of flutes, bull nose radius and the ball end radius, a general geometric model of the cutter is defined. The milling operation consists of a rotating cutter and linearly feeding the workpiece. The rigid body motion of a cutting point on the tool edge is described by a trochoidal path. Previous researches assumed a linear shift of circular paths, which produce significant errors when the axial depth of cut and radial immersion are significantly small as in the case of ball end milling operations. In this thesis, the true kinematics of ball milling are modelled. The instantaneous positions of all points on the flutes are expressed as a function of time using the stationary spindle as a coordinate center. The intersection of rotating and linearly moving end mill with the workpiece surface is computed, and the finished surface is stored at time intervals. The chip thickness is calculated by finding the radial distance between the two subsequent surfaces digitized

in two successive tooth passages. The static and dynamic displacements of the cutter are integrated to the kinematic model, hence allowing the influences of vibrations and static deflections on the chip thickness and the finish surface.

The time varying cutting forces are proportional to the chip thickness predicted by the geometric and kinematic models of milling. The force amplitudes are dependent on the oblique geometry of the end mill and plastic deformation properties of the workpiece material during cutting. The machining properties of the material are identified from two dimensional orthogonal cutting tests, which resembles plain strain deformation. The average yield shear stress, shear angle and friction coefficient between the tool and workpiece material are measured at a range of rake angle, cutting speed and chip thickness. The pressure and friction load on the oblique cutting edge of helical end mill and ball end mill are predicted using orthogonal to oblique cutting transformation method. It has been experimentally verified that the ball end milling forces in three directions can be predicted with sufficient accuracy using the kinematic and cutting mechanics approach presented.

The dynamic interaction between the tool and workpiece, which involves tool vibrations due to excessive cutting forces and structural flexibility in the system, including the effects such as tool jumping in and out of cut due to excessive vibrations are implemented in a time domain simulation program. The structural properties of the end mill attached to the spindle is considered to predict the chatter vibrations. The simulation program has the capability and versatility to predict milling forces, both statically and dynamically, surface form errors and chatter marks, under different milling operations, with different cutter geometries. The model is able to predict chatter vibration free axial depth of cuts and spindle speeds, i.e. *stability lobes*, for a given workpiece material, tool geometry and the frequency response characteristics of the end milling system. The

stability lobe diagrams have been developed and experimentally verified for both cylindrical and ballend cutter geometries. Process damping has been found to be a dominant factor at low speeds, which introduces discrepancies into the model. Furthermore, the time domain simulation results have been compared with analytically predicted chatter stability lobes. It has been observed that while the analytical stability prediction method is sufficiently accurate at large width of cuts, the time domain simulation model gives more accurate predictions at low width of cuts due to its handling of nonlinearities in the dynamic cutting system.

The kinematic and geometric models developed in this thesis are general, and applicable to other workpiece materials rather than titanium alloy (*Ti6AlV4*) used here. However, the orthogonal to oblique cutting mechanics transformation model may not be applicable when the shearing is not continuous. Hence, further investigation is required to analyze the viability of the method in machining hardened die and mold steels, where the chip is segmented and fracture and shearing may be coupled in the primary deformation zone of cutting.

The integration of proposed algorithms to the NC tool path generation in die and mold machining is a natural extension of the work. Optimization of depth of cut, width of cut, cutting speed and feed during NC tool path planning may significantly improve the productivity and accuracy of milling dies and molds.

Bibliography

- [1] D. Montgomery and Altintas Y. Mechanism of Cutting Force and Surface Generation in Dynamic Milling. *Trans. ASME Journal of Engineering for Industry*, 113:160-168, 1991.
- [2] M.E. Martellotti. An Analysis of the Milling Process. *Transactions of the ASME*, 63:677-700, 1941.
- [3] M.E. Merchant. Basic Mechanics of the Metal Cutting Process. *Trans. ASME Journal of Applied Mechanics*, pages A-168-175, 1944.
- [4] F. Koenigsberger and A.J.P. Sabberwal. An Investigation into the Cutting Force Pulsations During Milling Operations. *International Journal of Machine Tool Design and Research*, 1:15-33, 1961.
- [5] F. Koenigsberger and J. Tlustý. *Machine Tool Structures*, volume 1. Pergamon Press, 1970.
- [6] F. Koenigsberger and J. Tlustý. *Machine Tool Structures-Vol.I : Stability Against Chatter*. Pergamon Press, 1967.
- [7] W.A. Kline, R.E. DeVor, and W.J. Zdeblick. A Mechanistic Model for the Force System in End Milling with Application to Machining Airframe Structures. In *North American Manufacturing Research Conference Proceedings*, page 297, Dearborn, MI, 1980. Society of Manufacturing Engineers. Vol. XVIII.
- [8] W.A. Kline, R.E. DeVor, and R. Lindberg. The Prediction of Cutting Forces in End Milling with Application to Cornering Cuts. *International Journal of Machine Tool Design and Research*, 22(1):7-22, 1982.
- [9] W.A. Kline, R.E. DeVor, and I.A. Shareef. The Prediction of Surface Accuracy in End Milling. *Trans. ASME Journal of Engineering for Industry*, 104:272-278, 1982.
- [10] W.A. Kline, R.E. DeVor, and I.A. Shareef. The Effect of Runout on Cutting Geometry and Forces in End Milling. *International Journal of Machine Tool Design and Research*, 23:123-140, 1983.
- [11] H.J. Fu. *A Dynamic Modelling Approach to the Optimal Design of Nonuniform Chip Loading in Face Milling*. PhD thesis, University of Illinois, 1985.

- [12] J. Thusty and P. MacNeil. Dynamics of Cutting Forces in End Milling. *Annals of the CIRP*, 24:21–25, 1975.
- [13] I. Yellowley. Observations of the Mean Values of Forces, Torque and Specific Power in the Peripheral Milling Process. *International Journal of Machine Tool Design and Research*, 25(4):337–346, 1985.
- [14] E.J.A. Armarego and N.P. Deshpande. Force Prediction Models and cad/cam Software for Helical Tooth Milling Processes. i. Basic Approach and Cutting Analyses. *International Journal of Production Research*, 31(8):1991–2009, 1993.
- [15] E.M. Lim, Feng, H.Y., and C.H. Menq. The Prediction of Dimensional Errors for Machining Sculptured Surfaces Using Ball-End Milling. In K.F. Ehmann, editor, *Manufacturing Science and Engineering*, pages 149–156. ASME 1993 Winter Annual Meeting, New Orleans, USA, 1993. PED-Vol.64.
- [16] G. Yucesan and Y. Altintas. Mechanics of Ball End Milling Process. In K.F. Ehmann, editor, *Manufacturing Science and Engineering*, pages 543–551. ASME 1993 Winter Annual Meeting, New Orleans, USA, 1993. PED-Vol.64.
- [17] E.J.A. Armarego and R.C. Whitfield. Computer Based Modelling of Popular Machining Operations for Force and Power Predictions. *Annals of the CIRP*, 34:65–69, 1985.
- [18] E.J.A. Armarego and N.P. Deshpande. Computerized End-Milling Force Predictions with Cutting Models Allowing Eccentricity and Cutter Deflections. *Annals of the CIRP*, 40(1):25–29, 1991.
- [19] E. Budak, Y. Altintas, and E.J.A. Armarego. Prediction of Milling Force Coefficients from Orthogonal Cutting Data.
- [20] M. Yang and H. Park. The Prediction of Cutting Force in Ball-End Milling. *International Journal of Machine Tool Design and Research*, 31(1):45–54, 1991.
- [21] K.H. Tai C.C., Fuh. A Predictive Force Model in Ball-End Milling including Eccentricity Effects. *International Journal of Machine Tool Design and Research*, 34(7):959–979, 1994.
- [22] T.C. Ramaraj. Analysis of the Mechanics of Machining with Tapered End Milling Cutters. *ASME, Journal of Engineering Industry*, 116:398–404, 1994.
- [23] S. Smith and J. Thusty. Update in High Speed Milling Dynamics. *ASME 1987 Winter Annual Meeting*, 25:153–165, 1987.

- [24] J. Slavicek. The Effect of Irregular Tooth Pitch on Stability in Milling. In *Proceeding of the 6th MTDR Conference*. Pergamon Press, London, 1965.
- [25] P. Vanherck. Increasing Milling Machine Productivity by Use of Cutter with Non-Constant Cutting-Edge Pitch. In *Proc. Adv. MTDR Conf.*, volume 8, pages 947–960, 1967.
- [26] S.A. Tobias and W. Fishwick. A Theory of Regenerative Chatter. *The Engineer - London*, 1958.
- [27] S.A. Tobias and W. Fishwick. The Chatter of Lathe Tools under Orthogonal Cutting Conditions. *Transactions of the ASME*, 80:1079–1088, 1958.
- [28] J. Tlustý and M. Poláček. The Stability of Machine Tools Against Self Excited Vibrations in Machining. *International Research in Production Engineering, ASME*, pages 465–474, 1963.
- [29] R. Sridhar, R.E. Hohn, and G.W. Long. General Formulation of the Milling Process Equation. *Trans. ASME Journal of Engineering for Industry*, pages 317–324, May 1968.
- [30] I. Minis and T. Yanushevsky. A New Theoretical Approach for the Prediction of Machine Tool Chatter in Milling. *Trans. ASME Journal of Engineering for Industry*, 115:1–8, 1993.
- [31] E. Budak. *Mechanics and Dynamics of Milling with Flexible Structures*. PhD thesis, University of British Columbia, October 1994.
- [32] S. Smith and J. Tlustý. An Overview of Modelling and Simulation of the Milling Process. *Trans. ASME Journal of Engineering for Industry*, 113(2):169–175, 1991.
- [33] S. Smith and J. Tlustý. Efficient Simulation Programs for Chatter in Milling. *Annals of the CIRP*, 42/1:463–466, 1993.
- [34] A.D. Spence and Y. Altintas. CAD Assisted Adaptive Control of the Milling Process. In *ASME 1989 Winter Annual Meeting—Control Issues in Manufacturing Processes*, pages 33–43, San Francisco, December 1989. ASME. DSC-Vol. 18.
- [35] A.J.P. Sabberwal. Chip Section and Cutting Force during the Milling Operation. *Annals of the CIRP*, 10:197–203, 1961.
- [36] E. Budak and Y. Altintas. Flexible Milling Force Model For Improved Surface Error Predictions. In *Proceedings of the 1992 Engineering System Design and Analysis, Istanbul, Turkey*, pages 89–94. ASME, 1992. PD-Vol. 47-1.

- [37] R.C. Whitfield. *A Mechanics of Cutting Approach for the Prediction of Forces and Power in Some Commercial Machining Operations*. PhD thesis, University of Melbourne, 1986.
- [38] E.J.A. Armarego and R.H. Brown. *The Machining of Metals*. Prentice-Hall, 1969.
- [39] G.V. Stabler. Fundamental Geometry of Cutting Tools. *Proceedings of the Institution of Mechanical Engineers*, pages 14–26, 1951.
- [40] Katsuhiko Ogata. *Discrete Time Control Systems*. Prentice-Hall Inc., 1987.
- [41] D.J. Ewins. *Modal Testing Theory and Practice*. Research Studies Press, England, 1984.
- [42] M.E. Martellotti. An Analysis of the Milling Process. Part II: Down Milling. *Transactions of the ASME*, 67:233–251, 1945.
- [43] J. Tlustý. Dynamics of High-Speed Milling. *Trans. ASME Journal of Engineering for Industry*, 108(2):59–67, May 1986.
- [44] S.A Tobias. *Machine Tool Vibration*. Blackie and Sons Ltd., 1965.
- [45] S.B. Rao. Analysis of the Dynamic Cutting Force Coefficient. Master's thesis, McMaster University, 1977.
- [46] J. Tlustý and S.B. Rao. Verification and Analysis of Some Dynamic Cutting Force Coefficients Data. *NAMRC, U. of Florida*, pages 420–426, 1978.
- [47] J. Tlustý. Analysis of the State of Research in Cutting Dynamics. *Annals of the CIRP*, 27/2:583–589, 1978.
- [48] E. Budak and Y. Altintas. Analytical Prediction of Stability Lobes in Milling. volume 44/1, 1994.
- [49] M. Weck, Y. Altintas, and C. Beer. Cad Assisted Chatter Free Nc Tool Path Generation in Milling. *International Journal of Machine Tool Design and Research*. (accepted for publication, 1993).
- [50] S. Smith and J. Tlustý. Update on High Speed Milling Dynamics. *Trans. ASME, Journal of Engineering Industry*, 112:142–149, 1990.
- [51] J. Tlustý and F. Ismail. Basic Nonlinearity in Machinig Chatter. *Annals of the CIRP*, 30:21–25, 1981.

Appendix A

Ballend Milling Force Coefficients

Table A.1: Edge Force Coefficients, Rake = 0 degree

$$\begin{aligned} K_{TE} &= 37.205 \text{ N/mm} \\ K_{RE} &= 21.04 \text{ N/mm} \\ K_{AE} &= 0.64 \text{ N/mm} \end{aligned}$$

Table A.2: Cutting Force Coefficients, Rake = 0 degree

Ra	fd	Krc	Ktc	Kac
1.27	0.0254	513.96747	1888.6835	-3.953168
1.27	0.0508	678	2344.5276	-70
1.27	0.0762	685.91083	2238.9265	0.706506
1.27	0.1016	535.4541	2111.4316	-91.45192
2.54	0.0254	244.91734	1988.1965	-242.039
2.54	0.0508	790.64752	2101.0342	-247.3838
2.54	0.0762	722.81268	2053.55	-200.5565
2.54	0.1016	669.86633	1992.5186	-259.0192
3.81	0.0254	291.18442	1800.4019	-435
3.81	0.0508	529.13086	1833.5325	-375.5063
3.81	0.0762	636.08765	1921.2904	-342.0091
3.81	0.1016	554.21527	1818.9087	-363.1614
6.35	0.0254	196.4164	1651.0255	-481.531
6.35	0.0508	630.36206	1820.4677	-335.1002
6.35	0.0762	647.32898	1534.0551	-337.677
6.35	0.1016	246.82477	1163.6793	-206.1739

Orthogonal Cutting data Edge force analysis

SPEED= 9 RPM 2.76 M/MIN	Edge forces: Fce ave= 98.3 N Ffe ave= 174.93 N	Shear stress: $r = r_0 \cdot \tan \alpha$ $r_0 = 1.577 - 0.038 \cdot \text{Rake}$ $\alpha = 0.282 - 0.0085 \cdot \text{Rake}$	Friction angle: $B = 18.71 + 0.239 \cdot \text{Rake}$
Cutting Ratio:	Rake in degrees		
SPEED= 15 RPM 4.61 M/MIN	Edge forces: Fce ave= 102.5 N Ffe ave= 179.08 N	Shear stress: $r = r_0 \cdot \tan \alpha$ $r_0 = 1.955 - 0.063 \cdot \text{Rake}$ $\alpha = 0.342 - 0.0097 \cdot \text{Rake}$	Friction angle: $B = 18.41 + 0.336 \cdot \text{Rake}$
Cutting Ratio:	Rake in degrees		
SPEED= 31 RPM 9.52 M/MIN	Edge forces: Fce ave= 99.93 N Ffe ave= 158.47 N	Shear stress: $r = r_0 \cdot \tan \alpha$ $r_0 = 1.019 + 0.044 \cdot \text{Rake}$ $\alpha = 0.23 + 0.0048 \cdot \text{Rake}$	Friction angle: $B = 20.21 + 0.259 \cdot \text{Rake}$
Cutting Ratio:	Rake in degrees		
SPEED= 92 RPM 26.3 M/MIN	Edge forces: Fce ave= 72.44 N Ffe ave= 141.66 N	Shear stress: $r = r_0 \cdot \tan \alpha$ $r_0 = 2.108 - 0.045 \cdot \text{Rake}$ $\alpha = 0.3624 - 0.0084 \cdot \text{Rake}$	Friction angle: $B = 26.85 + 0.107 \cdot \text{Rake}$
Cutting Ratio:	Rake in degrees		
SPEED= 154 RPM 47.3 M/MIN	Edge forces: Fce ave= 59.92 N Ffe ave= 148.55 N	Shear stress: $r = r_0 \cdot \tan \alpha$ $r_0 = 2.26 - 0.056 \cdot \text{Rake}$ $\alpha = 0.353 - 0.0083 \cdot \text{Rake}$	Friction angle: $B = 17.68 + 1.615 \cdot \text{Rake}$
Cutting Ratio:	Rake in degrees		
SPEED= 196 RPM 60 M/MIN	Edge forces: Fce ave= 59.92 N Ffe ave= 148.55 N	Shear stress: $r = r_0 \cdot \tan \alpha$ $r_0 = 2.214 - 0.0672 \cdot \text{Rake}$ $\alpha = 0.364 - 0.0209 \cdot \text{Rake}$	Friction angle: $B = 10.86 + 0.69 \cdot \text{Rake}$
Cutting Ratio:	Rake in degrees		

Table A.3: Results from Orthogonal Cutting Experiments